Karlsruhe Institute of Technology

Precise determination of the electron beam energy with Compton backscattered laser photons at ANKA

Zur Erlangung des akademischen Grades eines
DOKTORS DER NATURWISSENSCHAFTEN

von der Fakultät für Physik
des Karlsruher Institutes für Technologie (KIT)

genehmigte
DISSERTATION
von

Cheng Chang
aus China

Tag der mündlichen Prüfung: 22. January 2016
Referent: Prof. Dr. Anke-Susanne Müller
Korreferent: Prof. Dr. Marc Weber

Abstract

Synchrotron light sources have become indispensable facilities for numerous disciplines in modern science and technology. Using optics settings with ultra-low momentum compaction factors, short electron bunches and short pulses of synchrotron radiation can be achieved, which has increasingly demanded by users in various fields. As one of the fundamental machine parameters, energy is included in various aspects of the machine physics and related applications. Its accurate calibration is the corner stone to correctly model the machine, accurately control the optics and precisely determine other energy-related parameters, such as the momentum compaction factor.

ANKA (Angströmquelle Karlsruhe) is a third generation light source, providing users synchrotron radiation from the far-infrared to hard X-rays. Its operation energy is from 0.5 GeV to 2.5 GeV. Since 2004 short bunch operation using ultra-low momentum compaction factor at 1.3 GeV and 1.6 GeV has been provided for THz radiation research.

Previously, the method of resonant spin depolarization was used to accurately determine the energy and the momentum compaction factor at 2.5 GeV of the ANKA electron storage ring. However, this method becomes cumbersome or even unrealistic for lower energies, especially for the short bunch operation, since the build-up time of the polarized electron beam becomes extremely long. Therefore an innovative method based on Compton backscattering has been developed to accurately calibrate the entire energy range of ANKA storage ring with typical relative uncertainties of a few 10^{-4}. Especially the nonlinear momentum compaction factors at short bunch operation have also been determined precisely.

Compared to the conventional method based on Compton backscattering using head-on collision, the new approach at ANKA adopts transverse configuration. As an improvement of the method, the measurement above 2 GeV based on Compton backscattering has been demonstrated successfully. The setup can be used at storage rings with restricted space as it does not require any reflective component that possibly interfere the existing beamline structure and the optical setup can also be made very compact. The setup at ANKA does not require any modification of the beam pipe as an existing ion pump port has been used to couple in the laser through its housing onto the electron beam.

The theoretical model, numerical studies, design and implementation of the respective sub-system and component, the measurement procedure as well as the measurement results are presented in this thesis. The possibilities of the setup adaption to other facilities have also been explored and included.

Keywords: synchrotrons, Compton backscattering, energy measurement, momentum compaction factor, CO_2 laser, high purity germanium spectrometer

Contents

1. Introduction

This chapter will first introduce the significance of precise and accurate determination of electron beam energies at the synchrotron light sources, i.e. the motivations of the thesis. Then the basic characteristics of Thomson scattering, Compton scattering and Compton Back-Scattering (CBS) are presented. The excellent properties of CBS scattered photons can also be used for high energy photon production as Compton light sources.

1.1 Motivation

Light is such a crucial means for human beings to perceive the nature. For modern science and technology, photons with wavelength beyond visible range become increasingly important. Since the wavelength of the X-rays ranges between 0.01 nm - 10 nm, which is the atomic to molecular scale of most substances, the tremendous value of X-ray for microscopic research has been drawing great attention ever since it was discovered by W.C. Röntgen in 1895. By taking advantages of X-rays, the double helix structure of DNA was revealed in 1953, heralding a new era of the life science.

Although for numerous fields such as the molecular biology, material/nano science, medical studies, etc. the demand for high flux/brightness X-ray sources are ever increasing, the traditional X-ray source like X-ray tubes has limited capacity due to their broad energy spectrum, low spectral flux and all-direction emission.

Synchrotron light sources, on the other hand, can provide advantageous radiation with very high brightness, good collimation and polarization, excellent pulsed time structure, also covering the entire electromagnetic spectrum from THz to hard X-ray frequencies. At synchrotrons, relativistic electrons are accelerated by the electromagnetic field in the accelerating cavities. When their propagation direction is guided by the magnetic field in a curved manner, the synchrotron radiation is generated and concentrates in the forward direction.

After the first synchrotron radiation was observed in 1947 at a General Electric synchrotron in the United States and its exceptional properties were recognized in the 1960s, three generations of synchrotrons have been developed and utilized. The first generation of synchrotron light sources was the parasitic use of the accelerators specifically designed for high energy physics research. Their great success led to the second generation, which took advantages of many bending magnets at the storage ring to produce the dedicated synchrotron radiation. The ever increasing demand for higher brightness and higher photon energy drove the synchrotron light sources to the third generation, characterized by multiple long straight sections for the insertion devices, such as undulators and wigglers (devices consisted of a series of dipole magnets introducing the periodic dipole field with alternating directions), to produce high brightness radiation or take advantage of the higher harmonics. Most of the third generation synchrotron light sources are selected in the medium energy region (2.4 - 3.5 GeV), while high energy synchrotron facilities have also been developed with higher cost such as 6 GeV ESRF (European Synchrotron Radiation Facility in France), 7GeV APS (Advanced Photon Source in the United States) and 8 GeV SPring-8 (Super Photon ring in Japan). The photon energy of hard X-ray synchrotron radiation can usually go up to tens of or even 100 keV [1]. Due to the outstanding properties, large scale synchrotrons have been widely developed and extensively used, now there are around 50 synchrotron facilities all over the world [2].

Free Electron Laser (FEL), driven by linear accelerators or Energy Recovery Linac (ERL), has shown outstanding properties and the potential of full coherence, tunable wavelength, ultrashort pulse structure and much higher spectral brightness than the current third generation synchrotron radiation, therefore is regarded as fourth generation of accelerator based light sources.

Besides the high spectral brightness and short wavelength, the short time structure of the electron beam and resultant radiation enable users to study the dynamic process on a short time scale, e.g. via pump-probe experiments. In contrast to the single usage by passing though the electron beam only once at FELs and ERLs, the storage ring just accumulates and circulates the electron beam for a very long time, therefore the equilibrium state generated by stochastic quantum emission dominates the beam emittance and the bunch length. However, some synchrotron facilities use special methods to provide shorter bunch lengths, one of them is to use low momentum compaction factor (α_c) to reduce the electron bunch length to picosecond scale [3-5]. Furthermore, when the electron bunch length is shorter than the radiation wavelength, the emission from every electron in the bunch (10^8 - 10^{11}) can add together constructively as Coherent Synchrotron Radiation (CSR). The radiation power of CSR is proportional to the square of the electron number instead of the linear dependence as for the incoherent radiation. Therefore besides the benefit of time resolved studies, the picosecond bunch length also leads to CSR in the Far-Infrared (FIR) to Terahertz (THz) regime with tremendous flux and brightness.

Located at the Karlsruhe Institute of Technology in Germany, ANKA (Angströmquelle Karlsruhe) is a third generation light source. From 2003 the facility began to provide users synchrotron radiation from the far-infrared to hard X-rays. So far there are 16 operational beamlines with one under construction. The operation energy of ANKA storage ring is from 0.5 GeV at injection to 2.5 GeV for normal user operation. Since 2004 short bunch operation using optics with ultra-low momentum compaction factor (so called low-α_c mode) at 1.3 GeV and 1.6 GeV has been provided for THz radiation research at the IR1 and IR2 beamline [6].

One of the most fundamental parameters of accelerators is their beam energy, as it is included in various aspects of the machine physics and related applications. For the colliders, the accurate knowledge of the beam energy is normally required for the high energy experiments and determination of the new particle characteristics. For the light sources, it is also crucial to accurately calibrate the electron beam energy to correctly control the optics (the magnet current), produce photons (energy deviation of the insertion devices) and understand the machine (e.g. the values of α_c). For example, the bursting threshold current of the CSR has a strong dependence on the bunch length, which is, on the other hand, proportional to $\sqrt{\alpha_c}$. Therefore the uncertainty level of α_c has a great influence on the bunch length and determines how good the threshold current can be calculated. As shown in Fig. 1.1, if the values of α_c can only be determined at the relative uncertainty level of ±10%, the bursting threshold can hardly be predicted precisely, especially for the slightly larger bunch lengths. But if the uncertainty level reaches only ±1%, the values will be nearly the same as the theoretical curve. Often to precisely measure α_c the beam energies need to be accurately determined, especially for the low-α_c modes, where α_c can become highly nonlinear, see section 6.3. Usually, if the relative uncertainty of the electron beam energy can achieve around 10^{-4}, the linear term of α_c can be determined with the relative uncertainty on the order of 10^{-2} [7]. Therefore an energy measurement with relative uncertainty of 10^{-4} is intrinsically valuable at ANKA.

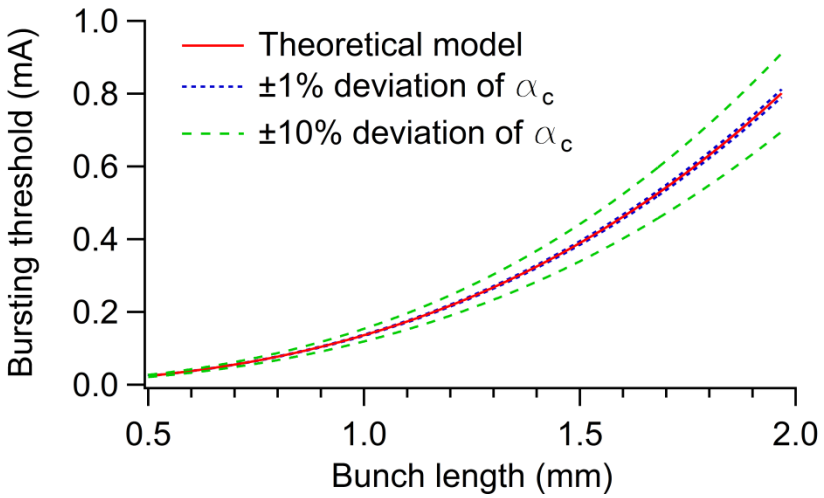

Figure 1.1: Calculation on the bursting threshold current at 1.3 GeV at ANKA. The red solid curve is the theoretical model of threshold current [8]. The green dashed lines form the boundary of ±10% relative uncertainties of α_c, while the blue dotted lines present ±1% deviation, which are nearly the same as the precise value.

For the circular storage rings, besides the direct measurement of the magnetic field strength with the typical relative uncertainty around the order of 0.5% [9], the most commonly used methods for precise determination of the beam energy are the Resonant Spin Depolarization (RSD) with the typical relative uncertainty of 10^{-5} [10-12][13][14] and the detection of the CBS photons, generated by monochromatic laser light scattered off the relativistic electron beam, with the typical relative uncertainty of 10^{-4} - 10^{-5} [9, 15-22].

Previously, the method of resonant spin depolarization was used to accurately determine the energy at 2.5 GeV of the ANKA electron storage ring [23][24]. The momentum compaction factor at 2.5 GeV was also precisely measured accordingly [25]. While this method works well at higher energies, it becomes cumbersome for lower energies as the build-up time of the spin polarization is inversely proportional to the beam energy to the power of five. The measurement time would become extremely long, e.g. several hours at 1.3 GeV. However the low-α_c modes normally adopt the electron beam energies such as 1.3 GeV, because the natural bunch length increases with the beam energy according to $\sigma_s \propto (E_0)^{3/2}$, whereas the bunch length at beam energies lower than 1 GeV is dominated by longitudinal instabilities [26]. Therefore the RSD method cannot be used for the determination of α_c for the low-α_c modes typically with short life time of the beam, see chapter 6. Since CBS method does not require a polarized electron beam, it becomes a good alternative here.

Compared to the traditional CBS method, we have innovatively developed and realized a transverse configuration ($\varphi \approx \pi/2$). As a method improvement, this setup has several advantages: It is very compact (also cost-effective) and can therefore also be used at rings with restricted space. For example, our setup did not require any modification of the beam pipe as we have used an existing pump port to shoot the laser beam through the housing of an operational ion getter pump onto the electron beam. Furthermore, the transverse setup reduces the Compton edge energy by a factor of two, which makes the measurement and especially detector calibration considerably easier because available calibration sources have limited upper energies. The transverse configuration can in principle also be converted easily into a versatile diagnostics tool, for example a laser wire. The setup

has been proved to cover the entire energy range of ANKA and accurately determine α_c values at the low-α_c modes. Adaption with capability to measure even higher energies has also been designed and discussed, see section 3.1.2.

1.2 Thomson scattering and Compton scattering

Named after J. J. Thomson, Thomson scattering is the elastic scattering process of the incident electromagnetic wave by the free charged particle. The photon energy of the incident wave should be much smaller than the stationary particle energy, thus after the scattering the recoil of the particle can be neglected. Scatterings of visible light or even soft X-ray on the free electron satisfy such condition. If the electromagnetic field of the incident wave is relatively small, the particle motion is non-relativistic and the magnetic field of the incident wave is negligible. The electrical field of the incident wave drives the particle to do dipole oscillations, thus the emitted photons have the same frequency as the incident electromagnetic wave. As electromagnetic dipole radiation, it distributes symmetrically with respect to the forward and backward directions, but most strongly in the perpendicular direction to the particle oscillation plane. The total cross section of Thomson scattering is

$$\sigma_T = \frac{8\pi}{3} r_e^2 \approx 6.65 \times 10^{-29}\, m^2 . \tag{1.1}$$

where $r_e = 2.82 \times 10^{-15}$ m is the classical electron radius and σ_T is the total Thomson cross section.

But in the electron rest frame, if the energy of the incident photons is comparable to the rest energy of the electron, quantum effects have to be taken into consideration and the recoil of the electron cannot be neglected, classical Thomson scattering no longer applies. After the scattering the electrons obtain a part of the incident photon energy, so the wavelength of the scattered photons increases compared to that of the incident light. This inelastic scattering process is called Compton scattering [27]. Compton scattering provides clear evidence for the wave-particle duality of photons, thus its discoverer A.H. Compton won the Nobel Prize in physics in 1927.

1.3 Compton backscattering and Compton light source

Both the Thomson scattering and Compton scattering describe the process of incident photons scattered by the nonrelativistic electrons. For the relativistic electrons, however, due to Lorentz transformation, even the symmetrical distribution of the Thomson scattered photons in the electron rest frame will concentrate within a very small angle in the forward direction in the laboratory frame, and the scattered photon energy is also greatly increased (under linear scattering condition, the maximum energy is proportional to γ^2, γ is the Lorenz factor) compared to the incident photons. For example, generation of 0.1 nm hard X-ray only needs photons of around 1 μm wavelength scattered by around 26 MeV electron beam. Since the energy transfers from the relativistic electrons to the incident photons, just opposite to the Compton scattering at non-relativistic situation, the scattering process is usually called Inverse Compton Scattering (ICS), Compton Back-Scattering (CBS) or Laser Compton Scattering (LCS).

The parameters of the high energy CBS photons are entirely determined by the parameters of the electron beam and the laser beam at the Collision Point (CP). By adjusting the collision angle between the electron beam and the laser beam, the scattered photon energy can be easily adjusted.

The energy spectrum of the scattered photons has a sharp cutoff at the highest energy called Compton edge. The scattered photons with the maximum energy corresponds to the maximum yield and zero scattering angle, therefore quasi monochromatic scattered photons can be easily obtained with a selective collimator of a small aperture size. Also the polarization state of the CBS photons can be determined by the incident photons.

It is a good illustration to compare CBS photon sources to the undulator. The electromagnetic wave of the linear polarized laser can be regarded as a magnetic structure of the undulator/wiggler. The energy of the output photons is proportional to the square of the electron beam energy but inversely proportional to the undulator period length. Since the laser wavelength (~1 μm) is much smaller than the undulator (~1 cm), the electron beam energy required by CBS photon source is normally around two orders of magnitude lower compared to the undulator/wiggler at synchrotrons for the same energy level of the scattered photons. Therefore the size and cost of the CBS photon sources can be reduced significantly, which is promising for the development of compact light sources.

After the laser was invented, CBS was first proposed for high energy photon production in 1963 [28, 29], and experimentally demonstrated in 1964 [30]. However, due to the very small cross section, the yield of the scattered photons was too low for proper research applications. Nonetheless with the rapid development of the picosecond terawatt lasers with the Chirped-Pulse Amplification technique (CPA) and the high current, high-brightness electron accelerator, the small cross section was compensated with the demonstration and success in the field [31-33]. To increase the average spectral flux, Z. Huang and R.D. Ruth of SLAC (Stanford Linear Accelerator Center) proposed the use of the storage ring and the storage cavity (e.g. Fabry-Perot cavity) to accumulate and circulate high current electron beam and high power laser separately, and through high interaction rate, the average output photon flux can be increased by several orders of magnitude [34]. Recently, numerous Compton light sources based on the storage ring have been built or are under construction [35][36][37][38]. To further take advantage of the excellent electron beam qualities provided by the linear accelerator, e.g. the short bunch length and the low emittance, but still reserve the merits of high repetition rate and high average spectral flux, Compton light sources based on superconducting linear accelerators, ideally in combination with ERL technique and high brightness photo injector, were proposed and are still under rapid development [39-42][43][44]. The ERL technique is also environment-friendly with high energy efficiency by recycling the electron beam energy.

Compact Compton light sources can be a good supplement to the advanced but gigantic synchrotrons or FELs with very limited nationwide access and typically valuable beam time. The Compton light sources can provide quasi monochromatic (photons generated with Compton edge energy have zero scattering angle and highest spectral cross section, thus can be selected with a small aperture along the propagation axis, see section 1.4, 2.1 and Chapter 4), polarized and collimated X-ray pulses with much higher spectral flux and ultrashort time structure in contrast to the traditional X-ray tubes, and yet can be maintained and hosted by a university, a hospital or a research institute [37].

1.4 Compton backscattering between an electron and a laser photon

If a laser photon (energy E_l) scatters off of a relativistic electron (energy E_e) at an arbitrary collision angle φ, the energy E_s of the scattered photon follows the relativistic kinematics and is illustrated in Eq. 1.2 and Fig. 1.2, where α is the angle between the incoming laser and the scattered photon and θ is the scattering angle between the scattered photons and the electrons. The electron velocity divided by the speed of light is denoted by β:

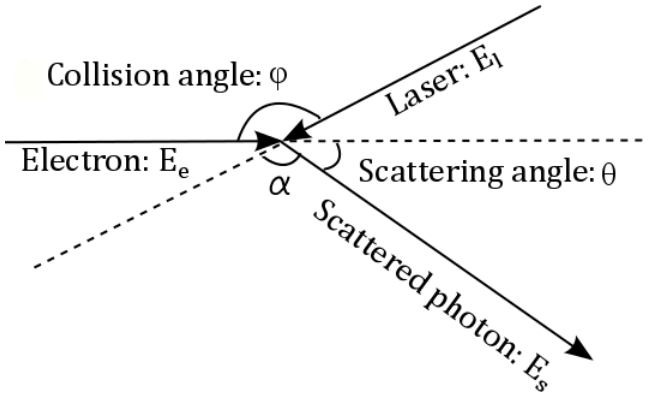

Figure 1.2: Scheme of CBS.

$$E_s = \frac{E_l(1-\beta cos\varphi)}{1-\ \beta cos\theta + E_l/E_e(1-\cos\alpha)}\ . \tag{1.2}$$

When θ is 0, α equals to φ, the energy of the scattered photons reaches its maximum,

$$E_{max} = \frac{E_l(1-\beta cos\varphi)}{1-\ \beta + E_l/E_e(1-cos\varphi)}\ . \tag{1.3}$$

The total CBS cross section on unpolarized electron is given by [35] [45]

$$\sigma_C = \frac{\pi {r_e}^2}{\rho}\left[2\left(1-\frac{4}{\rho}-\frac{8}{\rho^2}\right)ln(1+\rho)+1+\frac{16}{\rho}-\frac{1}{(1+\rho)^2}\right], \tag{1.4}$$

where

$$\rho = \frac{4E_eE_l}{m^2c^4}sin^2\left(\frac{\varphi}{2}\right) = \frac{4\gamma E_l}{mc^2}sin^2\left(\frac{\varphi}{2}\right),$$

mc^2 is the rest energy of the electron (0.511 MeV/c^2)and γ is the Lorenz factor.

When ρ << 1, i.e. the incident photon energy in the electron rest frame is much less than the rest energy of the electron, the Compton backscattering can be reduced to the relativistic Thomson scattering, and σ_C in Eq. 1.4 will equal to the total cross section of Thomson scattering σ_T in Eq. 1.1 approximately. Fig. 1.3 shows the total cross section of CO_2 laser (photon energy 0.117 eV at the wavelength of 10.6 μm) scattered by 1.3 GeV unpolarized electrons at an collision angle larger than 30 degree, which is very closed to σ_T (6.65×10^{-29} m^2).

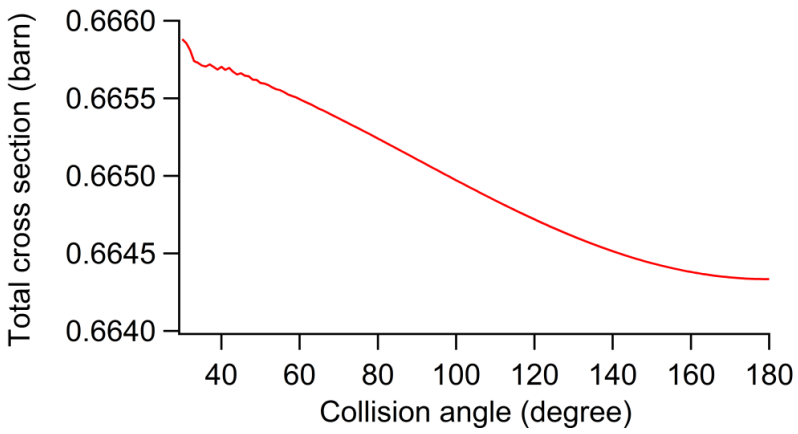

Figure 1.3: Total CBS cross section of CO_2 laser (photon energy 0.117 eV) scattered by 1.3 GeV unpolarized electrons at collision angle largers than 30 degree (1 barn = 10^{-28} m^2).

The energy spectrum of the scattered photons, i.e. the CBS differential cross section on E_s is

$$\frac{d\sigma_C}{d\varepsilon} = \frac{2\pi {r_e}^2}{\rho}\left[\frac{1}{1-\varepsilon} + 1 - \varepsilon - \frac{4\varepsilon}{\rho(1-\varepsilon)} + \frac{4\varepsilon^2}{\rho^2(1-\varepsilon)^2}\right], \tag{1.5}$$

where $\varepsilon = E_s/E_e$.

The energy spectra of the scattered photons with CO_2 laser scattered by 1.3 GeV electrons at different collision angles are shown in Fig. 1.4. The sharp Compton edges at the maximum energies indicate the great characteristics of high energy photon sources or the excellent diagnostics to determine the initial electron beam energy. Since the CBS total cross section remains relatively the same as the Thomson total cross section, and the maximum energy at 90° collision angle is around half of that at head-on collision (180° collision angle), the differential cross section at the Compton edge energy at 90° collision angle is nearly twice as large as that at 180° collision angle. In fact, according to Eq. 1.5, for $E_{max} << E_e$, the differential cross section at the Compton edge energy can be further reduced to

$$\frac{d\sigma_C}{dE_s}(E_{max}) \approx \frac{4\pi {r_e}^2}{E_{max}}, \tag{1.6}$$

Where $E_{max} \approx 4\gamma^2 E_l sin^2\left(\frac{\varphi}{2}\right)$. See section 2.1.

Thus, factors that reduce the Compton edge energy E_{max}, such as low γ, E_l or φ, can lead to a higher differential cross section at E_{max}.

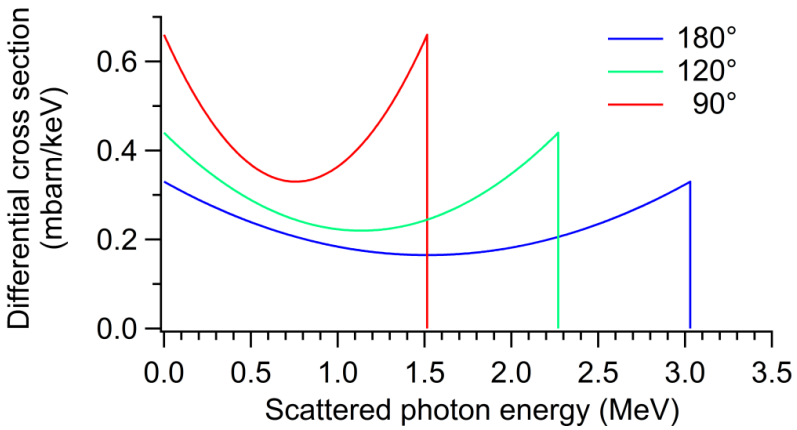

Figure 1.4: Energy spectra of the scattered photons with CO_2 laser scattered by 1.3 GeV electrons at different collision angles: φ = 180° (blue), 120° (green) and 90° (red).

1.5 Compton backscattering between an electron beam and a laser beam

In reality, both of the electron beam and laser beam have the finite energy and spatial distribution, thus the characteristics of the scattered photons are actually determined by the superposition of numerous single particle scattering events described in the last section.

For scattering of the electron bunches and laser pulses, the flux of the scattered photons can be expressed by

$$\frac{dN_s}{dt} = N_e N_p L_{sc} \overline{\sigma_C} f = L_{e\gamma} \overline{\sigma_C}, \tag{1.7}$$

where N_s is the total number of the scattered photons produced, N_e is the number of the electrons in an electron bunch, N_p is the number of photons in a laser pulse, f is the repetition rate of the collision. $\overline{\sigma_C}$ is the average CBS cross section for beam-beam interaction, which can be approximated by the Thomson total cross section σ_T when the scattering is closed to the relativistic Thomson scattering. $L_{e\gamma}$ is the interaction luminosity of the CBS process, expressed as $L_{e\gamma} = N_e N_p L_{sc} f$.

L_{sc} is the single collision luminosity, which describes the number of scattering events per unit CBS cross section. It depends on the collision angle, the density profile of the electrons and the photons at the collision point. For 3-D Gaussian distribution for both of the relativistic electron bunch (β≈1) and laser pulses, assuming the collision is in the horizontal plane, L_{sc} can be expressed by [46][47]

$$L_{sc} = \frac{1}{2\pi\sqrt{\sigma_{eV}^2+\sigma_{pV}^2}\sqrt{\sigma_{eH}^2 + \sigma_{pH}^2 + \left(\sigma_{eL}^2+\sigma_{pL}^2\right)cot^2\frac{\varphi}{2}}}, \tag{1.8}$$

where σ is the RMS size, the subscribes of “e” and “p” stands for electron bunches and laser photon pulses, the subscribes of “H”, “V” and “L” depicts the horizontal, vertical and longitudinal dimensions, respectively.

Specifically, for scattering around the collision angle of π/2, Eq. 1.8 becomes

$$L_{sc} = \frac{1}{2\pi\sqrt{\sigma_{eV}^2+\sigma_{pV}^2}\sqrt{\sigma_{eH}^2+\sigma_{pH}^2+\sigma_{eL}^2+\sigma_{pL}^2}}. \tag{1.9}$$

And for head-on scattering, L_{sc} can be further simplified as

$$L_{sc} = \frac{1}{2\pi\sqrt{\sigma_{eV}^2+\sigma_{pV}^2}\sqrt{\sigma_{eH}^2+\sigma_{pH}^2}}. \tag{1.10}$$

Further studies on characteristics of beam-beam scattering, such as spatial and energy distribution at a head-on collision, can be found in [48]. However, for the analytical model, assumptions under certain conditions have to be adopted. Also some integrals have to be numerically calculated. As to detailed studies of the scattering process at an arbitrary collision angle, CAIN series as stand-alone FORTRAN Monte-Carlo simulation codes [49] have been well developed by KEK (the high energy accelerator research organization in Japan). Investigation on CBS with Continuous Wave (CW) lasers on the booster ring and the storage ring at ANKA using CAIN2.42 are described on in Chapter 2 and 4.

1.6 Overview of the thesis

Chapter 2 will further establish the detailed analytical model of the diagnostic method based on CBS to determine the electron beam energy. As we have innovatively adopted a transverse setup with collision angle around π/2 to measure the electron beam energy, the difference between our innovative approach and the conventional method via head-on collision will be elaborated. As an illustration, the simulation and setup scenario on the booster ring will be explored.

Chapter 3 will focus on the setup on the storage ring, including the coupling ports, the detection system, the optical design and implementation. The detailed simulation studies on the characteristics of the scattered photons based on the parameters of the electron beam and the laser beam at the collision point will follow as in Chapter 4.

Chapter 5 will give the optimization studies of the measurement system, in particular for the influence of the intensity absorber misalignment on the measurement results. With the optimized setup, Chapter 6 will present all the systematic energy measurements at the ANKA storage ring, together with the determination of the momentum compaction factors of different optics at 1.3 GeV.

2. Compton backscattering based electron beam energy measurement at synchrotrons

In order to accurately and precisely determine the electron beam energy with CBS, we have to take advantage of some abrupt transitions, like the very narrow Compton edge in an energy spectrum. For determination of such edge energy, we have to select a detector with the highest available energy resolution. A High Purity Germanium (HPGe) spectrometer combines very high energy resolution with broad and suitable energy range for detection of Compton backscattered gamma rays generated at synchrotrons with GeV beam energies. The spectrometer has to be placed just downstream of the propagation direction of electron beams to intercept all the gamma rays with energy around the Compton edge.

2.1 Introduction of the method

In Chapter 1 we have obtained the maximum energy of the scattered photons as in Eq. 1.3, which forms a sharp cut-off edge in the energy spectrum called Compton edge,

$$E_{max} = \frac{E_l(1-\beta cos\varphi)}{1-\beta + E_l/E_e(1-cos\varphi)} . \tag{1.3}$$

For a typical GeV storage rings we have $E_e >> mc^2$ (mc^2 is the electron rest energy), the approximate value of β can be expressed as

$$\beta = \sqrt{1-1/\gamma^2} = \sqrt{1-\frac{m^2c^4}{{E_e}^2}} \approx 1-\frac{m^2c^4}{2{E_e}^2} ,$$

where

$$\frac{m^2c^4}{{E_e}^2} \ll 1 .$$

Thus we can substitute the approximate value of β into Eq. 1.3, which leads to

$$E_{max} \approx \frac{{E_e}^2 sin^2\left(\frac{\varphi}{2}\right) + \frac{m^2c^4}{4}cos\,\varphi}{E_e sin^2\left(\frac{\varphi}{2}\right) + \frac{m^2c^4}{4E_l}} . \tag{2.1}$$

For a typical collision angle (not very close to 0), it leads to an approximation for the cut-off energy E_{max} :

$$E_{max} \approx \frac{E_e}{1+\frac{m^2c^4}{4E_eE_l sin^2\left(\frac{\varphi}{2}\right)}} , \tag{2.2}$$

For typical laser photon energy less than 10 eV,

$$\frac{m^2c^4}{4E_eE_lsin^2\left(\frac{\varphi}{2}\right)} \gg 1\,.$$

Eq. 2.2 further reduces to

$$E_{max} \approx \frac{4{E_e}^2E_lsin^2\left(\frac{\varphi}{2}\right)}{m^2c^4} = 4\gamma^2E_lsin^2\left(\frac{\varphi}{2}\right). \tag{2.3}$$

The electron beam energy E_e can then be determined from the well-known values of mc^2, E_l, φ, and the measured E_{max} using

$$E_e \approx \frac{mc^2}{2sin\left(\frac{\varphi}{2}\right)}\sqrt{\frac{E_{max}}{E_l}}\,. \tag{2.4}$$

2.2 The relative uncertainties

From Eq. 2.4, we can easily get the relative uncertainty of the electron beam energy as

$$\frac{\sigma_{E_e}}{E_e} = \sqrt{\left(\frac{\sigma_{E_l}}{2E_l}\right)^2 + \left(\frac{\sigma_{E_{max}}}{2E_{max}}\right)^2 + \left[\frac{\sigma_\varphi}{2\tan(\varphi/2)}\right]^2}\,. \tag{2.5}$$

Here

σ_{E_l}/E_l is the relative uncertainty of the average laser photon energy. It is very important for the CBS method to have a very stable light source with photons of well-known energy as they act as a "ruler" or a "scale" for the precise determination of the electron beam energy. The required energy stability can normally be achieved by using specially designed gas laser oscillators, which aim at single line lasing, or by using an external Fabry-Perot Interferometer (FPI). The relative uncertainty is well below 10^{-5} for the CO_2 laser we have adopted for the storage ring, see section 3.2.1.1.

The uncertainty of the collision angle σ_φ comes from

(1) Obit drifts of the electron beam during measurement (< 0.01 mrad, monitored by BPM system);

(2) Measurement error of the electron orbit due to the limited accuracy of the beam position monitors from the calibration based on the beam-based-alignment method (< 0.1 mrad, estimated from BPM system and their beam based alignment at ANKA [50]);

(3) Mismatch between the magnetic and mechanical centers of the quadrupoles (< 0.05 mrad, estimated based on the characteristics of the quadrupole magnet [51]. The magnetic centers are the reference for the beam-based-alignment, while the determination of the laser direction is based on the mechanical centers.);

(4) Angular deviation of the laser (< 0.2 mrad, details of the measurement can be found in section 5.1.1).

Since $\tan(\varphi/2) \approx 1$ for $\varphi \approx \pi/2$ and approaches infinity for $\varphi \approx \pi$, for traditional head-on collision this term can be neglected (second order dependence of σ_{E_e}/E_e on the angular deviation is ${\sigma_\varphi}^2/4$). For the transverse setup used in this work, however, this term needs to be considered as it has an impact on and potentially limits energy measurement accuracy.

$\sigma_{E_{max}}/E_{max}$ is the relative uncertainty in determining the average energy of the Compton edge, and comprises two factors: the systematic and the statistic uncertainties.

The systematic uncertainty of determining E_{max} is limited by the accuracy of the energy calibration of the detector, which can reach a few 10^{-5} for commonly used HPGe detectors, see section 5.1.2. This is usually the limit of the traditional head-on collision setup.

The statistic uncertainty comes from the determination of E_{max} based on the spectral curve fitting. Since several factors like the energy spread of the electron beam and the finite energy resolution of the detector inevitably degrade the abrupt Compton edge and lead to a finite width, E_{max} now should refer to the average spectral position of the Compton edge. The specific process of curve fitting can be found in section 5.1.3.

The model to estimate the statistical uncertainty determined by edge fitting can be estimated as [45]

$$\frac{\sigma_{E_{max}}}{E_{max}}_{stat} \approx \sqrt{\frac{2\Delta E_{max}/E_{max}}{E_{max}\dfrac{dN_\gamma}{dE_s}(E_{max})}}, \tag{2.6}$$

where $dN_\gamma/dE_s(E_{max})$ is the Compton edge height. E_{max} is the average energy of the Compton edge photons which would be 0.2 MeV, 1.5 MeV, 2.3 MeV and 5.6 MeV for 0.5 GeV, 1.3 GeV, 1.6 GeV and 2.5 GeV electron beam energy, respectively. $\Delta E_{max}/E_{max}$ is the relative width of the Compton edge.

Using Eq. 1.6 and Eq. 1.7, Eq. 2.6 can be further expressed as

$$\frac{\sigma_{E_{max}}}{E_{max}}_{stat} \approx \sqrt{\frac{2\,\Delta E_{max}/E_{max}}{E_{max}\varepsilon_{int}L_{e\gamma}t\dfrac{d\sigma_c}{dE_s}(E_{max})}} \approx \sqrt{\frac{\Delta E_{max}/E_{max}}{2\pi {r_e}^2\varepsilon_{int}L_{e\gamma}t}}, \tag{2.7}$$

where r_e is the classical electron radius, ε_{int} is the intrinsic peak detection efficiency of the detector (see section 3.2.2), $L_{e\gamma}$ is the interaction luminosity of the CBS process, *t* is detector acquisition time.

For HPGe detectors, empirically, the intrinsic peak efficiency can be approximated as $\varepsilon_{int} \propto a{E_\gamma}^{-b}$ [52] [53], E_γ is the gamma photon energy. According to [53], when the incident gamma ray energy is more than 130 keV, the value b of the HPGe detector is slightly more than 1 (E_γ in keV). This value remains relatively the same until around3 MeV, and then tends to further increase with more polynomial terms included [54-56]. Therefore for a certain HPGe detector, if the Compton edge energy rises up from 130 keV until around3 MeV, to reach the same statistic uncertainty level for determination of the Compton edge energy based on curve fitting, the acquisition time needed is inversely proportional to the Compton edge energy, given that $L_{e\gamma}$ and $\Delta E_{max}/E_{max}$ in Eq. 2.7 remain the same. Above around 3 MeV, the acquisition time needs to be even longer to compensate

the further decreasing detection efficiency, see section 6.1. Therefore smaller Compton edge energy is highly preferable for the measurement method based on the CBS.

Including the consideration of the energy resolution of the detectors, the relative width of the Compton edge can be further expressed as [45]

$$\frac{\Delta E_{max}}{E_{max}} \approx \sqrt{\left(2\frac{\Delta E_e}{E_e}\right)^2 + \left(\frac{\Delta E_l}{E_l}\right)^2 + \left(\frac{\Delta\varphi}{tan\frac{\varphi}{2}}\right)^2 + \left[\frac{\Delta R(E_{max})}{R(E_{max})}\right]^2}. \quad (2.8)$$

$\Delta E_e/E_e$ is the energy spread of the electron beam (~10^{-4} - 10^{-3} for ANKA, see Chapter 4);

$\Delta E_l/E_l$ is the relative stability of the central laser photon energy plus relative line width (< 10^{-5} for the CO_2 laser we used, see section 3.2.1.1);

$\Delta R(E_{max})/R(E_{max})$ is the energy resolution of the detector at E_{max} (for normally used HPGe detector ~10^{-3}, see section 3.2.2).

There are several sources for deviations of the collision angle $\Delta\varphi$: (1) orbit drift during measurement (< 10^{-5} rad, see above at Eq. 2.5); (2) horizontal divergence angle of the electron beam (< a few 10^{-5} rad, estimated from parameters in Chapter 4); (3) angular drift of the laser (~10^{-4} rad, see section 5.1.1); (4) horizontal divergence angle of laser (< 10^{-5} rad for an elliptical focus spot used in this work, see section 3.1.1).

The numbers in the parentheses are again the estimations for the setup at the ANKA storage ring. $\Delta E_e/E_e$ and $\Delta R(E_{max})/R(E_{max})$ are the dominant contributions that widen the relative cut-off edge $\Delta E_{max}/E_{max}$ to ~10^{-3} on the recorded energy spectra.

To reduce statistic uncertainty to below 10^{-4}, for example for an 1.3 GeV electron beam, the Compton edge height must be higher than 100 counts/keV according to Eq. 2.6. If it reaches ~1000 counts/keV, the statistic uncertainty can be further reduced to a few 10^{-5}. It is comparable or even smaller than the systematic uncertainty due to the detector calibration stated above. For such edge photon count rates it is possible to bring $\sigma_{E_{max}}/E_{max}$ down to a few 10^{-5} at 1.3 GeV even for relatively short measurement times (see section 4.1.1).

Once we get the value of E_{max} and $\sigma_{E_{max}}$ from spectral edge fitting, we can calculate the electron beam energy using Eq. 2.4, and its relative uncertainty by Eq. 2.5. From the estimations given above, we can see the uncertainty of the collision angle σ_φ dominates the final uncertainty σ_{E_e}.

So far, several facilities have reported their beam energy measurements based on CBS using the traditional head-on geometry. For example, BESSY I and II, MLS in Germany, Duke university in USA, VEPP-4M at NINP in Russia and BEPC-II in China all successfully measured the beam energy with the uncertainty level of 10^{-4} to a few 10^{-5} [16-22].

At ANKA, energy measurements by detection of CBS photons are especially useful for energies lower than 2.5 GeV, for example at the low-α_c mode. Compared to conventional head-on collision methods previously used at several facilities, an innovative transverse scheme is adopted at ANKA for its high usability. For head-on collision schemes the absolute energy calibration of the HPGe detector is the

most challenging factor, whereas for transverse geometries, the collision angle accuracy is most likely the limiting parameter. The relative uncertainties achieved in our proof of principle experiment based on the transverse CBS method of energy measurement can be expected as a few 10^{-4}, see Chapter 5.

2.3 Studies of the measurement feasibility in the ANKA booster ring

Several locations for the installation of the CBS setup were considered, including the booster ring of the ANKA storage ring. The booster ring increases the beam energy of the electrons coming from the microtron from 53 MeV to 500 MeV, and injects them into the main storage ring with a 1 Hz repetition rate. The process mainly includes an energy ramp, a flattop of maximum energy and beam extraction as shown in Fig. 2.1. The advantage of the booster ring with respect to the installation of the CBS setup is that the ring provides ample space to introduce new hardware without interfering with beamlines. The feasibility of such a setup was studied and is briefly presented in the following. Finally it was decided to install the setup directly in the main storage ring.

2.3.1 Setup with CO_2 laser

The current of the booster ring is very low (~2 – 3 mA) and the time window of the maximum energy around 500 MeV (the flattop of the ramping curve in Fig. 2.1) is only around 40 ms per second, because the booster ring working at injection mode is not a typical storage ring. Therefore, it is necessary and critical to have a high intensity laser to scatter with the electron beam and high detection efficiency of the detector.

Since the low photon energy of the CO_2 laser leads to a high photon density at the same laser power, and the resulting low energy Compton edge photons also have better detection efficiency, we decided to use this as a model to study in the beginning. As adopted at BESSY II and MLS, the CO_2 laser from Edingburgh Instruments and Ortec 100% High Purity Germanium (HPGe) detector can provide high CW laser power (around 50 W) and enough detection capability and delivered very good measurement results [19, 20]. Thus we can estimate the performance of the CBS setup at the booster ring based on the same instruments.

To keep the measurement duration practical and to increase the signal to noise ratio without resorting to very high laser power, we furthermore assumed the integration of a Fabry-Perot cavity for a passive amplification of the laser power [57][58]. As we can see in Fig. 2.2, the electron beam circulates inside the beam pipe while laser photons are stored in the optical cavity. After they interact at the collision point, CBS gamma rays are generated and propagate towards the detector located at the corner of the hall, while electrons are deflected by the bending magnet. The collimator acts like an aperture placed just before the detector to select the useful photons at the Compton edge as much as possible while keeping the unnecessary background radiation low.

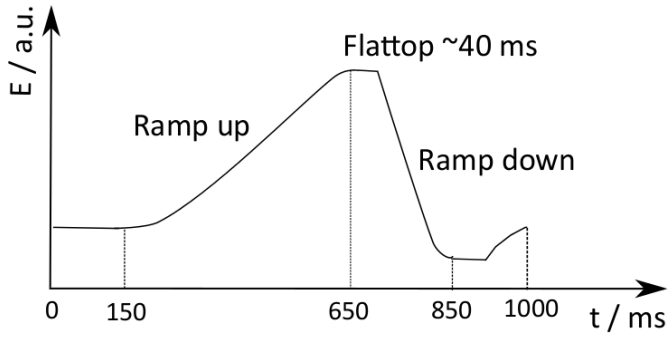

Figure 2.1: Sketch of the energy ramping curve of the bending magnet of the booster ring. The t values are not exact numbers.

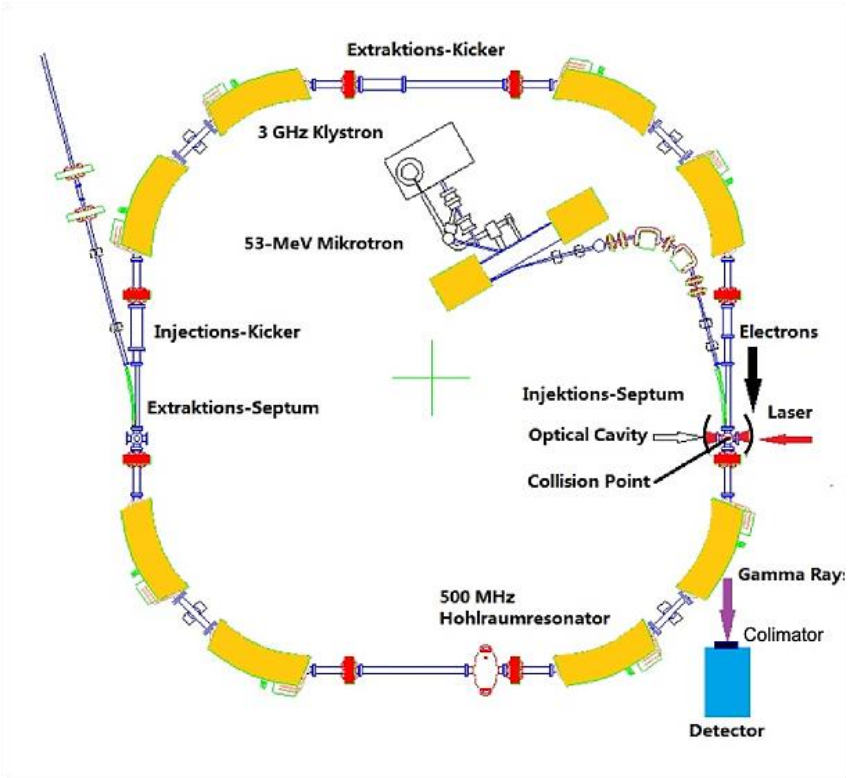

Figure 2.2: Setup with optical cavity at the booster ring.

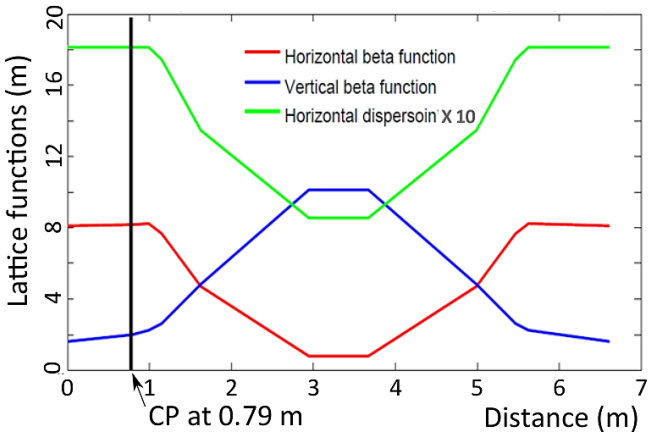

Figure 2.3: Beta and dispersion functions of ANKA booster ring (one quarter).

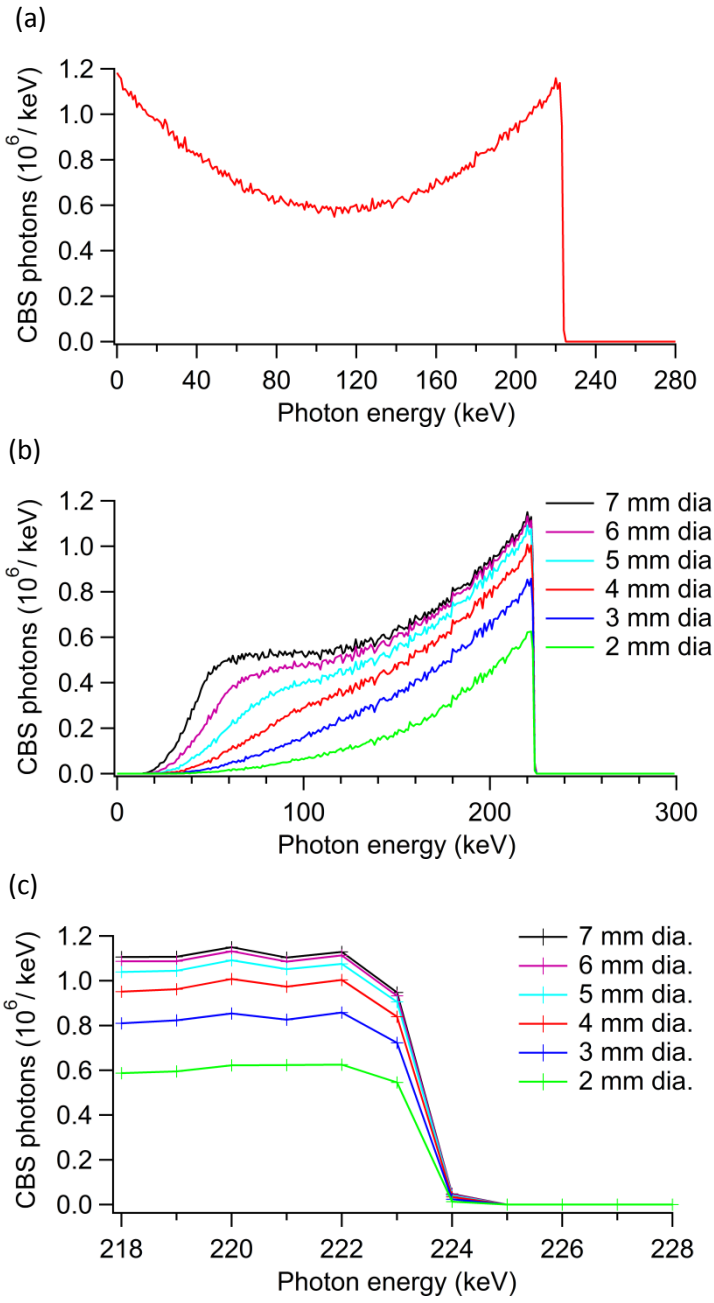

Figure 2.4: Simulation results for the transverse CBS setup with amplified CO_2 laser at around 500 MeV electron beam energy for 10 minutes acquisition time. (a) Entire energy spectrum, (b) Energy spectra of scattered photons received by different collimator apertures, (c) Compton edge received by different collimator apertures.

Based on the model in Accelerator Toolbox (AT) of Matlab [59], we can obtain the beta and dispersion functions of one quarter of the booster ring as shown in Fig. 2.3. The parameters of the electron beam at the Collision Point (CP) are summarized in Table 2.1, together with the information of the laser and the detector.

The calculation by AT shows that it only takes around 20 ms for the electron beam circulating in the booster ring to reach the equilibrium state, thus the values in Table 2.1 are for the 500 MeV flattop when the energy ramp up finishes. The dispersion function has been taken into consideration for the

horizontal beam size calculation, and the vertical emittance is taken from the measurement value in [60]. We can assume the measurement time is 10 minutes, which can be comparable to the duration of a good injection process. The vertical size of the laser is set to be around 100 µm to match the vertical size of the electron beam. This is not difficult to achieve since the input coupling ZnSe window can be close to the CP for a dedicated interaction cavity, see section 3.1.3.

Table 2.1: Parameters of the transverse setup for the booster ring at 500 MeV used for the feasibility studies.

Electron beam		Laser and Detector	
Beam current / mA	~3	Wavelength / µm	10.6
Energy / GeV	0.5	CW CO_2 laser power / W	50
Vertical size (RMS) / µm	~68	Vertical size (RMS) / µm	100
Horizontal size (RMS) / µm	1265	Horizontal size (RMS) /µm	100
Bunch length(RMS) / ps	106	Polarization	Vertical
Energy spread (RMS)	3.35×10^{-4}	Collision angle	90°
Horizontal dispersion / m	1.813	Enhancement factor of laser optical cavity	200
Emittance / nm × rad	H: 150.9	Collimator position after the CP / m	2.3
	V: ~2.3	Accumulation time / min	10

Using the parameters in Table 2.1 we can simulate the CBS photons and the Compton edge spectrum with CAIN2.42 as shown in Fig. 2.4. Panel (a) depicts the entire CBS spectrum at the CP, the Compton edge is at around 220 keV. From panel (b) we can see that a 5mm wide collimator already covers most of the edge photons, but cuts off most of the CBS photons with low energy, which also act as the background. Considering the high detection efficiency of the 100% HPGe and the low energy of the edge photons (around 220 keV), nearly every edge photon can be recorded in the spectrum with their full energy. Therefore we expect that 10 minutes accumulation at the injection mode of the booster ring results in an edge height around 1.0×10^6 / keV with the 5 mm diameter aperture. According to Eq. 2.6, this number of edge photons is high enough to bring the statistic uncertainty of edge energy determination below 10^{-5}, which is even smaller than the calibration uncertainty of the HPGe detector. Even without the optical cavity, the edge height would be around 5000-6000 / keV, which is still enough to bring the statistic uncertainty below 10^{-4}.

For the uncertainty of the electron beam energy, the dominant factor in this model is the accuracy and stability of the collision angle, determined by the drift and deviation of the laser and the electron beam orbit.

2.3.2 CBS photons transmitted through the bending magnet

Unfortunately, unlike bending magnets of a normal storage ring, the bending magnets of the booster ring are covered without a port for synchrotron radiation. Thus the scattered CBS photons have to pass through thick layers of iron as shown in Fig. 2.5. Their path length would be around 165 mm.

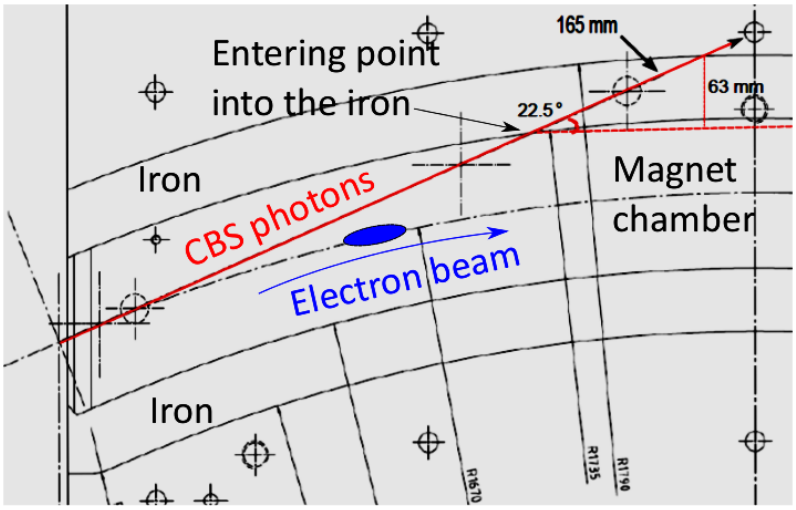

Figure 2.5: The path of the CBS edge photons though the bending magnet of the ANKA booster ring.

We can use a simple exponential decay to estimate the amount of CBS photons able to transverse such a bending magnet. When a beam of gamma ray with intensity I_0 is incident on a piece of material with thickness of x, the intensity of the radiation which passes through without any interactions is I_x, and the relationship between them is simply exponential $I_x = I_0 exp(-\mu\rho x)$, μ is called mass attenuation coefficient (in the unit of cm^2g^{-1}).

Since the stopping power of iron for gamma rays is quite large due to its high atomic number, for 16.5 cm thick iron nearly nothing is left of gamma rays with energy below 0.5 MeV. For 3 MeV only 1% is left, and even for 10 MeV only 2% can be expected to pass through the magnet without any interaction as summarized in Table 2.2. Therefore the setup with CO_2 laser discussed here is not feasible due to the special design of the booster ring.

Table 2.2: Transmitted gamma rays after passing through 16.5 cm iron.

Energy of gamma ray / MeV	Percentage passing through [61]
0.2	5.78×10^{-9}
0.5	1.82×10^{-5}
1	0.041%
2	0.392%
3	0.905%
4	1.353%
5	1.678%
10	2.029%

2.3.3 Setup with visible and UV laser

From Table 2.2, we can see that for high energy gamma photons, there is still a small proportion of the edge photons left after passing through the iron. We therefore considered using a visible or even UV laser as an alternative solution since this leads to higher energy photons according to Eq. 2.4. However, high energy edge photons is more difficult to be recorded by the HPGe detector, and the

differential cross section at the high energy Compton edge is much smaller than at the low energy edge. Furthermore, at the same power level, the visible laser has much lower photon density than the mid-infrared laser due to its much higher photon energy. Therefore the laser power, together with amplification factor of the optical cavity for the visible laser, need to be even higher than in the previous CO_2 laser scenario.

We can use a 514 nm CW Argon laser (Innova-Sabre DBW 25 from Coherent [62]) as a typical estimation and illustration. The available power and wavelength is summarized in Table 2.3. We can use the same parameters as for the CO_2 case in Table 2.1 to simulate the Compton edge spectrum, except now the laser has 514 nm wavelength, 10 W input power and 1000 enhancement factor from the optical cavity [63]. The laser power at the CP is the same as that in the CO_2 case.

Table 2.3: Considered power and wavelength options of an Argon laser.

Wavelength / nm	Output power / W
514.5	10.0
488.0	8.0
351.1	1.8

Fig. 2.6 shows that the Compton edge energy is around 4.57 MeV, which confirms the analytical result from Eq. 2.3. Only 3000/keV edge photons are produced in 10 minutes with a 40 ms energy flat-top. For 4.55 MeV edge photons, only around 1.5% of them can pass through the bending magnet. If we assume that around 8% can be recorded by the detector due to this relatively large energy, then there are only a few counts per keV at the Compton edge recorded on the spectrum every 10 minutes. Although based on the estimation using Eq. 2.6, only around 100 counts/keV are needed at the edge to reduce the statistic uncertainty of edge energy determination to 10^{-4}. Unfortunately, around 200-300 minutes are required to accumulate such amount of data, which certainly exceeds a practical measurement time.

To reduce this accumulation time, higher laser power or larger enhancement factor of the optical cavity would be required. This, however, would be quite demanding and difficult to handle. Another possible solution is to extend the measurable flat-top of the maximum energy to longer times. However, the capacity of the power supply to ramp the bending magnets of the booster ring is very limited. According to Danfysik, the power supply vendor, a good experimental target is 100 ms[64]. Therefore if the extension of the flat-top time to 100 ms would be possible, the accumulation time could be further reduced to around 80-120 minutes, which might be possible for the measurement.

For the 488 nm laser option, the edge photons are at around 4.8 MeV according to Eq. 2.3. The percentage left after passing though the bending magnet would be 1.6%, only slightly higher than that at 514 nm wavelength. The laser power, however, is only 80% compared to that of the 514 nm case, the photon number is even lower considering its higher photon energy. A lower signal is expected to be recorded at the Compton edge. For a wavelength of 351 nm, the signal is even worse.

If a pulsed laser can be used, the situation would be much improved since the pulse length of the electron bunch of ~105 ps (RMS) is relatively small compared to the revolution period of 88 ns. More than 100 times more edge photons can be expected. Therefore it would be good enough for the measurement with the 514 nm laser in 10 minutes of a 40 ms flat-top. However, investigation on

whether the relative stability of the central/average wavelength can be kept below 10^{-5} should be carried out, since a short laser pulse is actually composed of numerous line modes and the central/average wavelength does not necessarily stay the same, if e.g. the pulse length or the chromatic dispersion varies. In this case there might be serious deviation of the reference of the accurate laser photon energy needed to calculate the electron beam energy using Eq. 2.4. Also amplifying and keeping laser pulses stable inside the optical cavity as well as synchronizing them with electron bunches would be difficult.

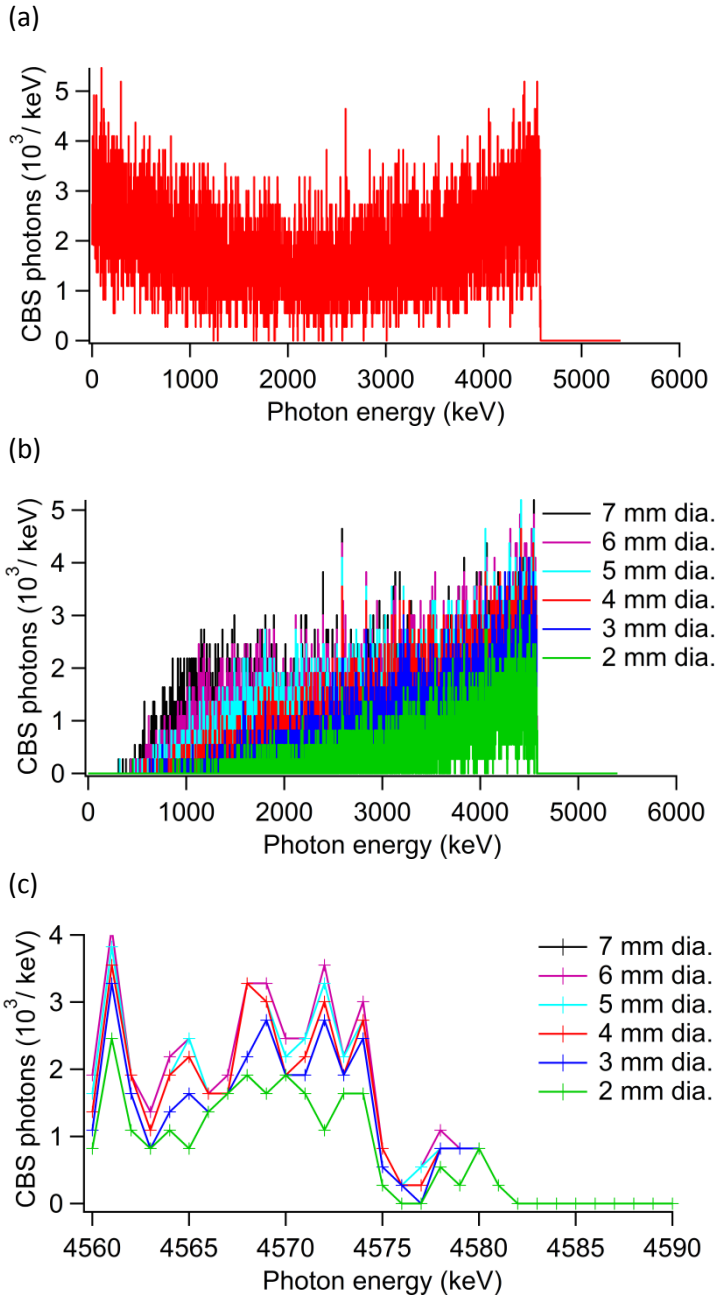

Figure 2.6: Simulation results for the transverse CBS setup with amplified argon laser at 500 MeV electron beam energy for 10 minutes acquisition time. (a) Entire energy spectrum, (b) Energy spectra of scattered photons received by different collimator apertures, (c) Compton edge spectra received by different collimator apertures.

2.3.4 Altered operation modes of the booster

The booster ring in storage mode cannot be operated continuously at 500 MeV due to power supply limitations. At 250 MeV, however, this should be possible. We can also operate it at around 300 MeV with injection of the electron beam every 2 seconds (0.3 s ramp up, 1.5 s flat top, 0.2 s ramp down). Continuous storage of 300 MeV beam needs further investigation.

Table 2.4 summarizes a preliminary estimation with different combination of laser and electron beam conditions. The assumption is that for ~200 nm or ~300 nm UV laser either the laser power or the enhancement of the optical cavity is much lower than that for ~400- 500 nm, therefore the laser intensity at the CP should be at least 10 times lower. As we can see that the best combination is to have a 300 MeV electron beam scattered on a 514 nm laser beam.

Table 2.4: Compton edge energies and accumulation time at different operation and laser modes.

Electron energy / MeV	Wavelength of the laser / nm	Energy of Compton edge / MeV	Time needed for data accumulation
300	257	3.3	~200 min (CW) / ~300 min (0.5 Hz)
250	257	2.3	~500 min (CW)
300	514	1.6	~30 min (CW) / ~40 min (0.5 Hz)
250	514	1.1	~70 min (CW)

2.3.5 Further investigation

There seem to be several possibilities to measure at the ANKA booster ring, depending on the following conditions.

Firstly, due to the low signal rate, the radiation background level received by the HPGe should be measured and the signal to noise rate should be studied. Since the vacuum condition in the beam pipe of the booster is worse than in the main storage ring, the intensity of the gas bremsstrahlung would be much higher. The gas bremsstrahlung is also concentrated in a narrow cone along the electron beam propagation direction, and its energy can go up to the electron beam energy. Therefore most of the bremsstrahlung photons can easily pass through the bending magnet and even more secondary scattered radiation and particles can be generated.

Secondly, the enhancement factor of the optical cavity proposed for the booster is quite challenging. We therefore must be able to achieve effective coupling and amplification inside the optical cavity.

Thirdly, detailed studies need to be performed on the interaction between the signal edge photons and the iron of the bending magnet. The edge photons probably would get an additional energy spread towards lower energy, therefore undermining the precision of the energy determination. Similar effects can be found in Chapter 5 for the interaction between Compton edge photons and the misaligned intensity absorber in the main ANKA storage ring.

We finally decided to proceed with the measurement at the ANKA storage ring, since the location at the ANKA storage ring has the advantage that the electron energy can be measured not only at 500 MeV (the injection energy), but also at 1.3GeV and 1.6 GeV (the energies of the frequently used low α_c modes), as well as 2.5 GeV (the energy of the user operation). Measurement at 2.5 GeV allows the cross-check with resonant spin depolarization method previously established at ANKA. The principle of the setup at the storage ring is nearly the same as that at the booster ring, and will be described in the following chapters.

3. Setup design at the storage ring

Considering both energy resolution and detectable energy range with reasonable efficiency, an HPGe spectrometer is the best option for our measurement. To ensure that the Compton edge energy for such GeV scale electron beams is still within the detectable range of commercially available HPGe spectrometers (up to 10 MeV), we chose a CO_2 laser emitting in the mid-infrared range as the scattering photon source. Also the frequency (the photon energy) of CO_2 lasers can be stabilized to achieve relative uncertainties of 10^{-5} or even better. This is crucial for energy measurements based on Compton backscattering. The gamma photons generated by CBS propagate in a narrow cone along the direction of the electron beam. The photons with the Compton edge energy are concentrated on the propagation axis. We use a tungsten collimator in front of the detector to collect these photons and reduce the background level. The crystal section of the HPGe is shielded by lead blocks in the experimental environment to further decrease the background signal.

3.1 Comparison between different scenarios at ANKA storage ring

With appropriate laser and detection system, a comparison between different scenarios at ANKA storage ring can be made. At ANKA, there are feasible positions for laser-electron interaction at the long straight section in section 4 with space for the HPGe detector at the front end area of the X-SPEC beamline. As we can see in Fig. 3.1, there are mainly two scenarios to perform the experiment, one allows installation of a dedicated interaction cavity, and the other is to couple in the laser directly through an existing ion pump. Both of them couple in the laser horizontally. Another possible transverse configuration would be to shoot the laser from the bottom to the top of the beam pipe, e.g. through a scraper port. However, in this case, the focusing spot size has to match the horizontal electron beam size, which is nearly 10 times larger than the vertical beam size in the horizontal coupling scenario. So the laser density would be 10 times smaller, which would cause roughly 10 times less gamma rays, deteriorating the signal to noise ratio.

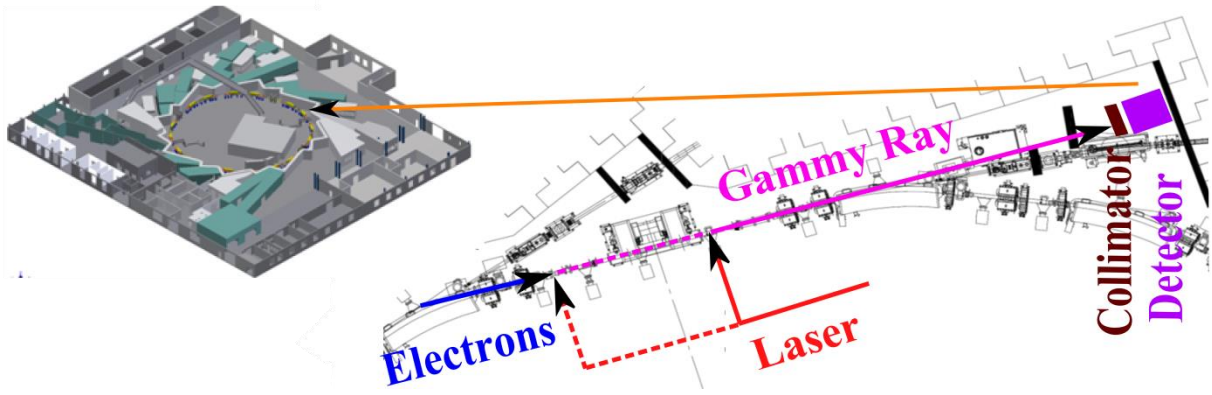

Fig 3.1: Layout scenarios of Compton scattering setup at ANKA. The solid line of laser stands for the ion pump coupling, while the dashed line represents the position for a dedicated chamber.

3.1.1 Direct laser coupling through an ion pump port

This design is to take advantage of an existing ion pump, coupling the laser through its housing, as shown in Fig. 3.2. The section after the ion pump consists mainly of a safety valve, a connecting cross shaped section (a standard piece with two 126 mm long tubes as we use, a special version with

horizontal tube of 86 mm length is possible from manufacture) and an anti-reflection coated ZnSe window to couple in the CO_2 laser. The broad band coated ZnSe window had ~98% transmittance around 10.2 μm, and was manufactured with special care for ultrahigh vacuum application (pressure range: 3 bar to 1×10^{-11} mbar). The cross shaped section connects the ZnSe window and the valve, also provides access to pump the section down to the ultrahigh vacuum condition as shown in Fig. 3.2.

In this configuration, the laser hits directly the back side of the beam pipe after the interaction with the electron beam. The cross section and dimension of the beam pipe are shown in Fig.3.4. There is a channel for cooling water, but unfortunately there is no copper plate on the inner side of the running water at our setup position to facilitate heat dissipation as in Fig. 3.4. Thus to minimize heat load effects on the ultrahigh vacuum with the laser beam hitting the back wall of the beam pipe, we used a cylindrical lens as the final focusing lens to tightly focus the laser beam vertically while maintaining a large horizontal beam size. This keeps large laser-electron interaction luminosity but increases the laser spot area, thus decreasing the laser power density on the beam pipe as much as possible. Details of the optical design are described in section 3.3.1.

The laser beam size of a Gaussian profile along the optical path can be calculated as

$$w^2(z) = w_0^2\left[1+\left(\frac{\lambda z}{n\pi w_0^2}\right)^2\right], \tag{3.1}$$

where w_0 is the beam waist at the focal plane at zero position, w(z) is the beam radius where the beam intensity drops to $1/e^2$ and equals 2σ (σ is the standard deviation of Gaussian distribution, z is the position along the optical path and n is the refraction index of the medium along the optical path.

In the field far from the beam waist, Eq. 3.1 further reduces to

$$\theta \approx \frac{w(z)}{z} \approx \frac{\lambda}{n\pi w_0}, \tag{3.2}$$

where θ is the divergence of the laser beam in the far field. Thus for a specific laser, to achieve a small beam waist at the focal plane, the divergence angle of the input beam must be large. In reality the divergence angle depends on the clear aperture of the entrance window. For example, our ZnSe entrance window with a CF40 flange has 35 mm diameter clear aperture.

We want to achieve a relatively small beam waist of w_0 = ~300 μm (around the middle of the beam pipe) to match the vertical size of the electron beams at low α_c mode at 1.3 GeV (σ ~100 μm) as well as possible. This size still allows the compensation of possible position fluctuation of the laser beam due to vibrations of optical components. Since the window aperture limits the laser input beam size, it requires special effort to shorten the distance between the window and the middle of the beam pipe to achieve a larger divergence angle in Eq. 3.2.

From Fig. 3.2 we can see that, for the setup using the ion pump port, the distance between the window and the center of the beam pipe is 880 mm. From Eq. 3.1 we can calculate that we need around 11 mm vertical beam radius at the entrance window position to achieve a 300 μm vertical waist radius w_0 (all the calculations in this section are based on an M^2 value of ~1.1 for the CO_2 laser), although around 22 mm diameter laser beam on the window with around 35 mm clear aperture

inevitably causes clipping effect and diffraction patterns, see section 3.2.1.4. The laser spot has to be located at the center of the window to guarantee a relatively good and symmetrical focusing.

Also, we have to carefully choose the propagation direction/angle of the laser because, as we can see in Fig. 3.3, several possible obstacles are in its way: there are three supporting struts in the connecting piece between the ion pump and the beam pipe, one of them is located at the center. This makes it necessary to deviate from exactly 90 degrees relative to the beam pipe, so that the maximum intensity in the beam center is not obstructed. The limiting apertures along the coupling path together with the struts are marked by black circles in Fig. 3.2. The vertical laser beam size shrinks along the optical path while the horizontal size remains at around 12 mm due to the cylindrical lens, only three path restrictions (shown as red circles in Fig. 3.2) are actually limiting in this case. To minimize the clipping effect of the restrictions, the laser is calculated to be best steered around ±19 mrad off the exact perpendicular path relative to the beam pipe. However, this leads to a maximum of 28.8 mm equivalent horizontal aperture and therefore to a bigger clipping at the fringes of the horizontal focal spot. In the vertical direction, on the other hand, the clipping is only caused by the ZnSe window and very small.

Although there are a lot of details to be considered and optimized carefully in the design, the advantage of the setup without a dedicated interaction cavity is clear: it does not require any specific space, not only in the front-end area as in the conventional head-on method, but also at the storage ring. Given the common situation of very limited or restricted space at modern synchrotrons, it can be critical to be able to combine the function of an existing side port in order to implement such a compact CBS setup. From a design standpoint it is important to minimize the distance from the vacuum window to the scattering region. Also, a smaller collision angle would facilitate measurements of higher energies.

(a)

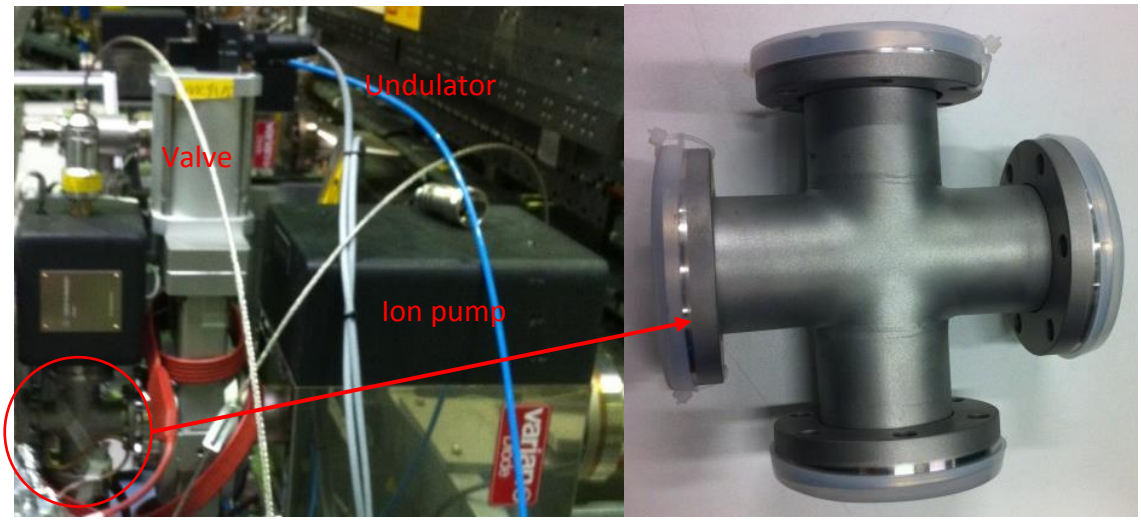

(b)

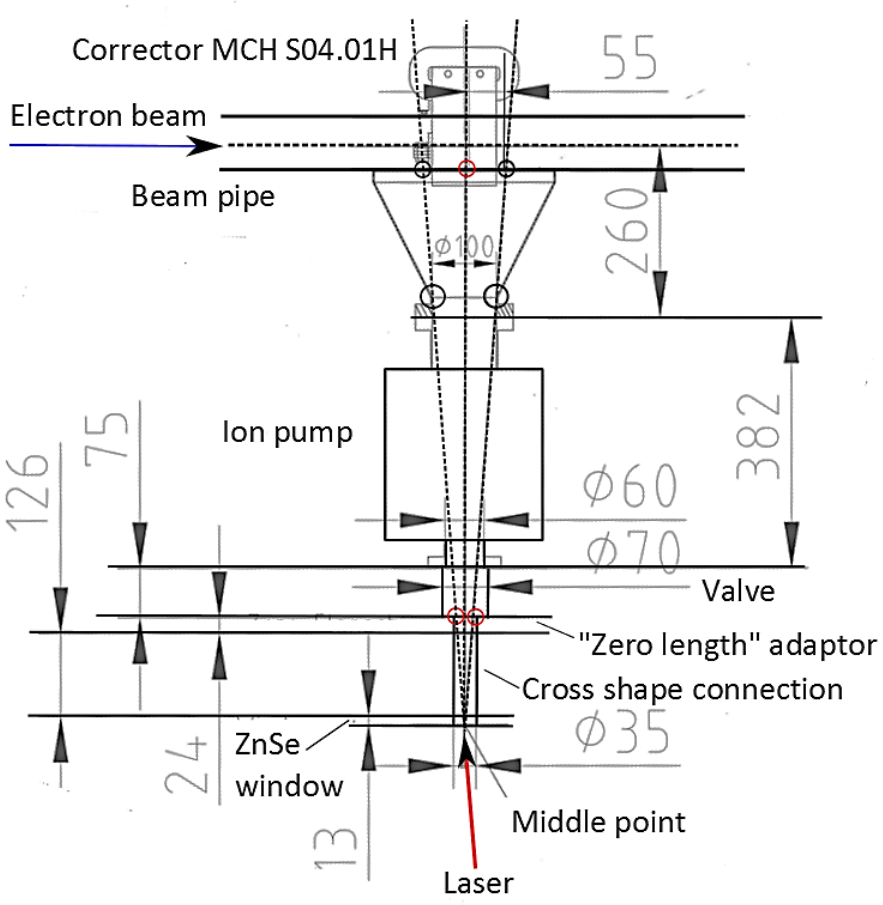

Fig 3.2: Laser coupling path through an ion pump: (a) side view photograph of the laser coupling setup; (b) top view sketch of the coupling tunnel with dimensions. The black circles are the possible restrictions where the laser beam is limited depending on the laser beam size. The red circles depict the points limiting the laser beam based on our actual beam size.

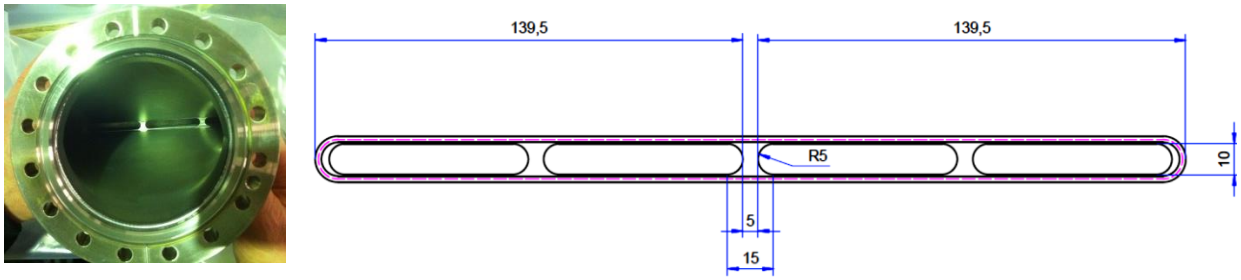

Fig 3.3: The struts in the adapter piece between the ion pump and the beam pipe.

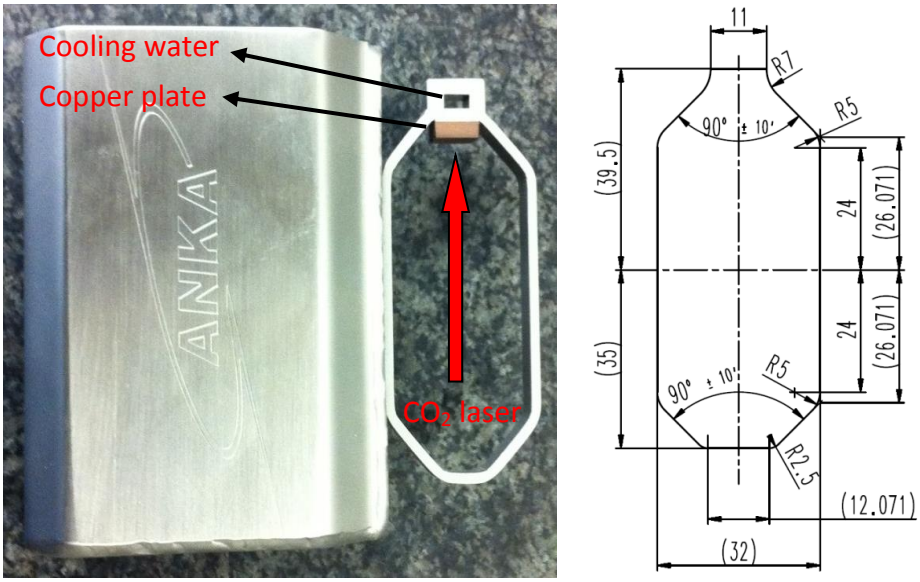

Fig 3.4: The ANKA beam pipe and its cross section.

3.1.2 Design with dedicated interaction cavity

As we can see Fig. 3.5, another possibility is to replace the vacuum valve in front of the WERA wiggler with a dedicated interaction chamber, which has two windows on each side of the beam pipe. This would allow a coupling of the laser beam through one window and absorb it through the other one. In this design, there are also two valves at both sides of the beam pipe for vacuum safety. A focusing lens or a parabolic mirror could focus the laser spot as small as needed at the collision point. With motorized stages we could scan laser beam vertically to achieve good overlap between the electron and the laser beam. The ion pump based design in section 3.1.1 could be a good starting point for the development of a dedicated chamber as in Fig. 3.5. From the dimension in Fig. 3.2, we can estimate for a compact interaction chamber, the distance from the window to the center of the beam pipe is around 250 mm to 300 mm. In this case a small input beam size of around 3-4 mm (2σ) on the window is sufficient to tightly focus the laser beam to around 300 µm at the focal plane.

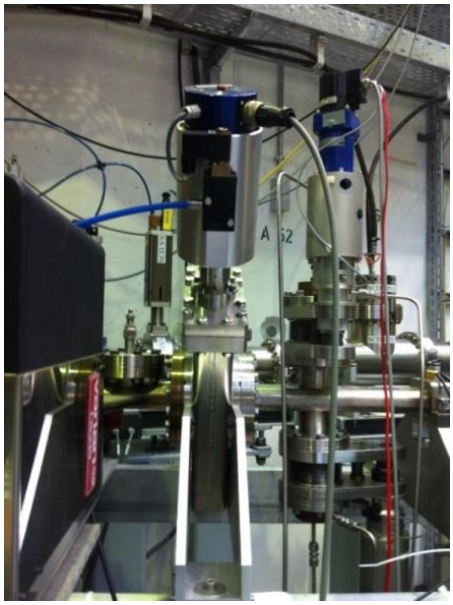

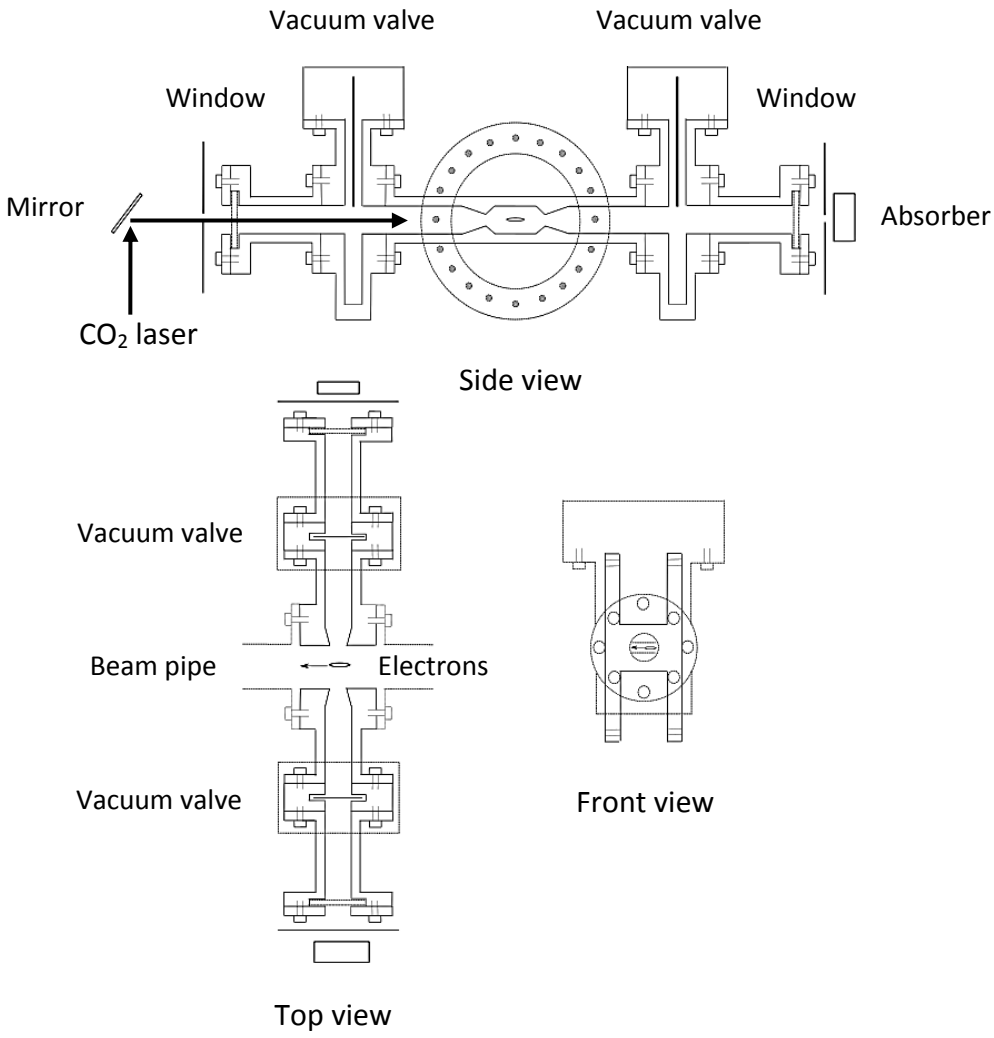

Figure 3.5: Sketch of the interaction cavity to replace a safety vacuum valve on the storage ring.

Though an interaction chamber requires a dedicated section of the storage ring and additional cost, the interaction cavity has several advantages:

First, the chamber should have an out-coupling port next to the input port. The laser power can then be directed through this second window at the back side, and absorbed by a beam dump. This would allow an increase of the laser power to improve the amount of Compton backscattered gamma rays, therefore leading to a better signal to noise ratio and a shorter measurement time. Several factors can make this necessary: increased background radiation level of gas bremsstrahlung due to higher energy, higher current or higher residual gas levels, or conditions with a lower electron-laser interaction rate, such as a larger vertical electron beam size. Also, we can monitor the laser power, beam position or angular drifts during measurements by detecting the out-coupled beam. If the laser power is not enough, a Fabry-Perot (FP) cavity for power amplification can be adopted [57,58,63].

Second, the transverse configuration offers more flexibility than the head-on collision. It provides the possibility to combine the energy measurement setup with a laser wire function, making it very attractive and versatile as an integrated instrument. For example, in order to achieve the laser wire function, the beam radius needs only to be enlarged to around 11-12 mm on the window to provide beam waist of around 80-90 μm (2σ) to scan through the vertical electron beam size (σ around 50-100 μm depending on energies and operation modes, see Chapter 4).

Third, since the electron beam sizes at different operation modes and energies can vary considerably, and the input beam size on the window is only around 3-4 mm with the dedicated cavity, we have the flexibility to adjust the laser waist size. For example, this can be achieved by using a laser beam expander, to match the electron beam parameters and thus maximize the interaction rate.

Last, a dedicated chamber can permit usage of smaller scattering angles. According to Eq. 2.3, smaller scattering angles lead to lower Compton edge energies. This has two advantages: the detection efficiency becomes higher at lower energies, and its calibration is more accurate since commercial high energy radiation sources are rarely available and may require higher radiation protection measures. On the other hand, smaller scattering angles allow the measurement of energies higher than 2.5 GeV. For example, with an HPGe of modest relative efficiency (around 40%) and using a $^{244}Cm/^{13}C$ calibration source (6.13 MeV), energies up to around 7 MeV can be measured reliably. According to Eq. 2.4, we need a collision angle around 80° to measure 3 GeV electron beams (as used at the Australian Synchrotron, NSLS-II, SOLEIL, ALBA, Diamond Light Source, MAX IV, Taiwan Photon Source, etc.); for 6 GeV electron beams (European Synchrotron Radiation Facility) we need around 40°; for 8 GeV electron beams (Spring-8) an angle around 30° is required.

Of course, the interaction angle depends on the HPGe crystal volume and to which energy we can calibrate it (e.g. $^{14}N(n,\gamma)^{15}N$ and $^{35}Cl(n,\gamma)^{36}Cl$ can reach above 10 MeV [56]. Larger HPGe crystal volumes and higher detection efficiencies can compensate the requirement to use smaller angles. Then electron energies up to 3.4 GeV can be measured with a strict perpendicular geometry, and 8 GeV electron beams can then be measured with a collision angle of 35°. However, such small angles most probably require a larger space in the storage ring.

In summary, the requirement of a dedicated chamber depends on the specific facilities. In general, the angular acceptance of the in-coupling port plays an important role in the design of such a system

as it limits the achievable focus size at the interaction zone. Furthermore, we can measure higher energies by using smaller the interaction angles.

3.2 Design and development of the CBS setup

For the measurements at ANKA, we chose a near-perpendicular geometry and decided to couple the laser into the vacuum through the ion pump port. This layout allowed keeping the space requirements minimal and covers the entire energy range at ANKA.

The setup mainly consists of a CO_2 laser and optical subsystem, HPGe detector and detection subsystem, and a vacuum coupling subsystem. The coupling port for the laser is already discussed in the last section, the coupling port for the CBS photons will be introduced in this part.

3.2.1 The CO_2 laser and the optical system

As discussed before, the most important reason to choose a long wavelength laser and small collision angle is to bring the Compton edge energy within the detectable range of the HPGe detector and to increase the detection efficiency. Besides, long wavelength lasers and low collision angles can increase the CBS edge photon intensity, since the long wavelength laser has higher photon density at the same laser power and the lower Compton edge energy makes the spectral differential cross section at the edge energy higher, see Eq. 1.6 and Fig. 1.3.

CO_2 lasers are among the most efficient lasers and are readily available at the required power levels. Besides, from section 3.1, we can see the CO_2 laser with wavelength of 10.6 μm is already hard to be focused tightly to scatter with the electron beam, given the practical size of the coupling window to the ultrahigh vacuum beam pipe. Thus, we chose CO_2 laser as our primary photon source to realize Compton edge energy around MeV scales.

3.2.1.1 Introduction to the CO_2 laser system

The CO_2 laser system was developed by the Deutsches Zentrum für Luft- und Raumfahrt (DLR)[65]. The system was installed near the storage ring at ANKA as shown in Fig. 3.6. It mainly consists of a laser head cavity, two electronic control units, a chiller and an oscilloscope. The laser head was designed originally to emit in the THz range with a THz resonator pumped by a commercial CO_2 laser. The components for the THz emission, not related to the CO_2 laser, were removed before the system was transported to ANKA. The components left now comprise a commercial laser from DeMaria Inc. (RF excited, model LC-40 from DeMaria purchased by Newport Corp.), and a beam splitter to pick up a small amount of laser power coupling into a Fabry-Perot interferometer (FPI). The FPI serves as an external reference, and a dedicated proportional–integral–derivative (PID) feedback loop stabilizes the frequency to about 10^{-6} by controlling the laser cavity length. This is important to obtain a high degree of accuracy for the CBS-based electron energy measurements. The relative stablity of the laser photon energy satisifies our measurement based on section 2.2. The CW laser is lasing at line 10R22 (λ=10.2332 μm) with linear polarization, and emits a maximum power of around 20 W. The beam waist is at the out-put coupler of the DeMaria laser, which is 1.54 mm (diameter, intensity drops to $1/e^2$) for a wavelength of 10.6 μm. The beam divergence (full angle) is 9.7 mrad. Thus the M^2 of the laser [66] is about 1.1.

There are other options of commercial products for such initial photon sources with extremely stable photon energy, such as PL series from Edinburgh Instrument as adopted in BESSY I/II and MLS, which has a relative stability of the laser frequency better than 10^{-7}. There is another much cheaper option as L-20S or AL-30S models from Access Laser (including the option of a line tracker), they also provide enough laser power and aim at at single line lasing, then the relative stability of frequency should be better than 10^{-5}, which still satisfies our theoretical requirement of the laser.

Figure 3.6: CO_2 laser and optical system.

3.2.1.2 Design and implementation of the optical system

The main purpose of the optical subsystem is: to focus the laser vertically to match the vertical size of the electron beam. Furthermore, we need to measure the laser propagation direction accurately. This allows the precise determination of the collision angle needed for the calculation of the electron beam energy (see Eq. 2.4 section 5.1.1).

To help with the alignment of the invisible CO_2 laser beam we used a visible alignment or pilot laser, coupled into the beam path via a beam combiner positioned at a 45° angle (see Fig. 3.8). To make sure both lasers co-propagated on axis throughout the optical path, an exact overlap had to be established. The overlap had to be achieved at two positions, best far away from each other. In our case, we made sure both beams overlapped on the optical table and a point 10 m away. We used temperature sensitive liquid crystal sheets to observe the position and beam profile of the CO_2 laser. There was one mirror in front of the pilot laser. Both of the mirror holder and the pilot laser mount had freedom of horizontal and vertical angular adjustment. We could adjust one holder to overlap the visible laser to the spot of the CO_2 laser on the crystal sheet at the near field, and use the other for the far field.

A remote controlled pneumatically driven laser beam block was installed after the beam combiner. This is important as there is no access to the experiment inside the ANKA storage ring during electron beam operation.

To guarantee that the beam expanded enough for the cylindrical lens to focus the beam down to around 300 μm diameter at the middle of the beam pipe, we designed the optical path such that we could use the large beam divergence of the laser (full angle is 9.7 mrad). A beam expander could be used to adjust the size of the beam waist according to the different electron beam size at various operation modes and energies to optimize the setup performance, or possibly integrated a laser wire function. Of course the ZnSe window needed a larger clear aperture than the one we used, or a dedicated interaction chamber was adopted as discussed in section 3.1.2.

The focusing lens needed to be located as near to the window as possible, so there would be a larger distance between camera position 1 and 2 in Fig. 3.8 for the laser tracker to determine the propagation direction of the CO_2 laser (details can be found in section 5.1). Furthermore, the further away from the window, the input beam size on the focusing lens needed to be bigger to achieve the same focal spot size. The focal length of the focusing lens was designed to be 1 meter.

The focusing lens was around 12 cm away from the window, making it possible to put another mirror in between to reflect the CO_2 laser beam through a second identically constructed vacuum window onto the Pyrocam camera with the same distance to the camera as the beam path to the electron interaction zone inside the electron beam pipe. Thus, the in-vacuum optical path is simulated as well as possible, so that the camera (at camera pos. 3 in Fig. 3.8) shows the laser beam profile expected at the laser-electron interaction region (“virtual focal plane”). This way we could also check if the working distance was correct to locate the focal plane at the middle of the beam pipe. This, however, should not be very sensitive since the Rayleigh range of the beam was quite large according to the Gaussian beam calculation (around 28 mm).

The camera was a Pyrocam IV from Ophir Photonics with a 1 inch × 1 inch active detecting area, protected by a broad-band (8 – 12 μm) antireflection coated window. When running in a chopped CW mode, it could monitor the CO_2 laser beam profile instantaneously based on the thermal effect of the laser beam. But the peak power density had to be less than the damage threshold.

An attenuator was used to reduce the laser power for the camera detection and aligning all the optical components safely. We used a LASNIX step attenuator (model 102) as its attenuation is based on diffraction from free-standing/substrate-less metal grids that preserve all the beam properties such as beam direction and offset. This is especially important for our measurement, since we have to precisely determine the laser beam propagation direction with the laser tracker and the camera, which requires an attenuated beam, while actual CBS measurements need full laser power. Thus, negligible angle offset by the attenuator was crucial for interpretation of our measurement results. The metal grids had 5 steps, which have 3 dB, 5 dB, 8 dB, 9 dB and 10 dB power attenuation respectively. We could choose any combination of them, with the maximum reduction of 35 db (3.2×10^{-4}, only 6 mW left for our 20 W laser). The diffracted laser power was absorbed in the housing walls, and air cooling was enough for 20 W. The tube of model 102 was 200 mm long with 19 mm diameter clear aperture. The attenuator was placed about 10 cm to the laser out coupling hole of the laser head cavity, and the distance from the DeMaria CO_2 laser to the center of the out coupling

hole was 24.7cm, thus the beam diameter at the end of the attenuator was only around 7 mm and could pass through the attenuator freely.

We used 75 mm (dia.) × 15 mm (thickness), gold plated mirrors (reflection > 99% at 10.6 µm wavelength) held by stainless steel mirror mounts together with solid, fixed length posts, making them very sturdy and insensitive to the possible vibrations. The 3 inch diameter spherical collimation lens was mounted on a manual XYZ translation stages (STANDA 7T67-25-XYZ). When it was adjusted to the right position, the beam became parallel after passing through it and we could monitor it by locating the camera at positions 1 and 2. The 3 inch × 3 inch square cylindrical lens was mounted on a motorized XYZ translation stages (STANDA 8MT167-25LS-XYZ). The motorization permits the remote adjustment of the laser focal position by adjusting Y and Z position of the lens during CBS measurements and the optimization of the scattering efficiency with the electron beam (see section 5.2.1).

The metal surface on the back side of the beam pipe can possibly reflect a large portion of laser power back. Thus, to protect the laser cavity, we chose a small angular offset from the exact perpendicular direction relative to the beam pipe. Given our long optical path, the offset angle only needs to be ±5 mrad, which is much less than the requirement of ±19 mrad as calculated in section 3.1.3. Another possibility would be a standard isolation components normally used in industry of high power CO_2 laser cutting, e.g. the combination of an absorbing thin-film reflector and a reflective phase retarders e.g. from II-VI Infrared Inc. But their cost and complexity was not necessary for our setup.

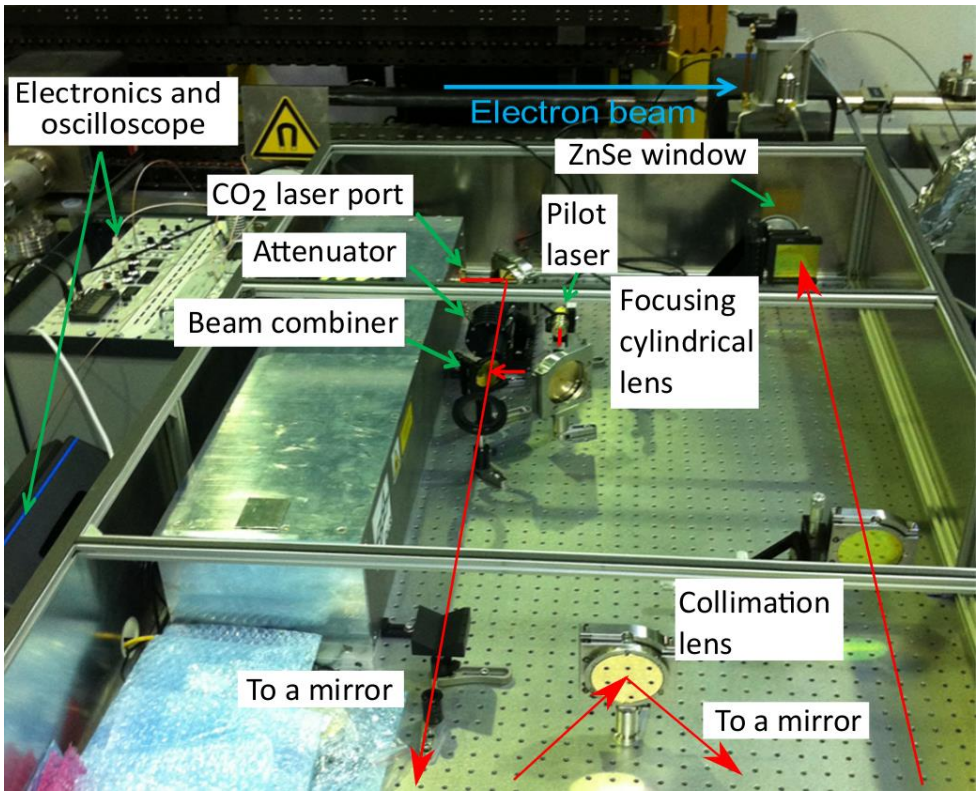

Figure 3.7: Main components of laser and optical system for CBS installed at ANKA.

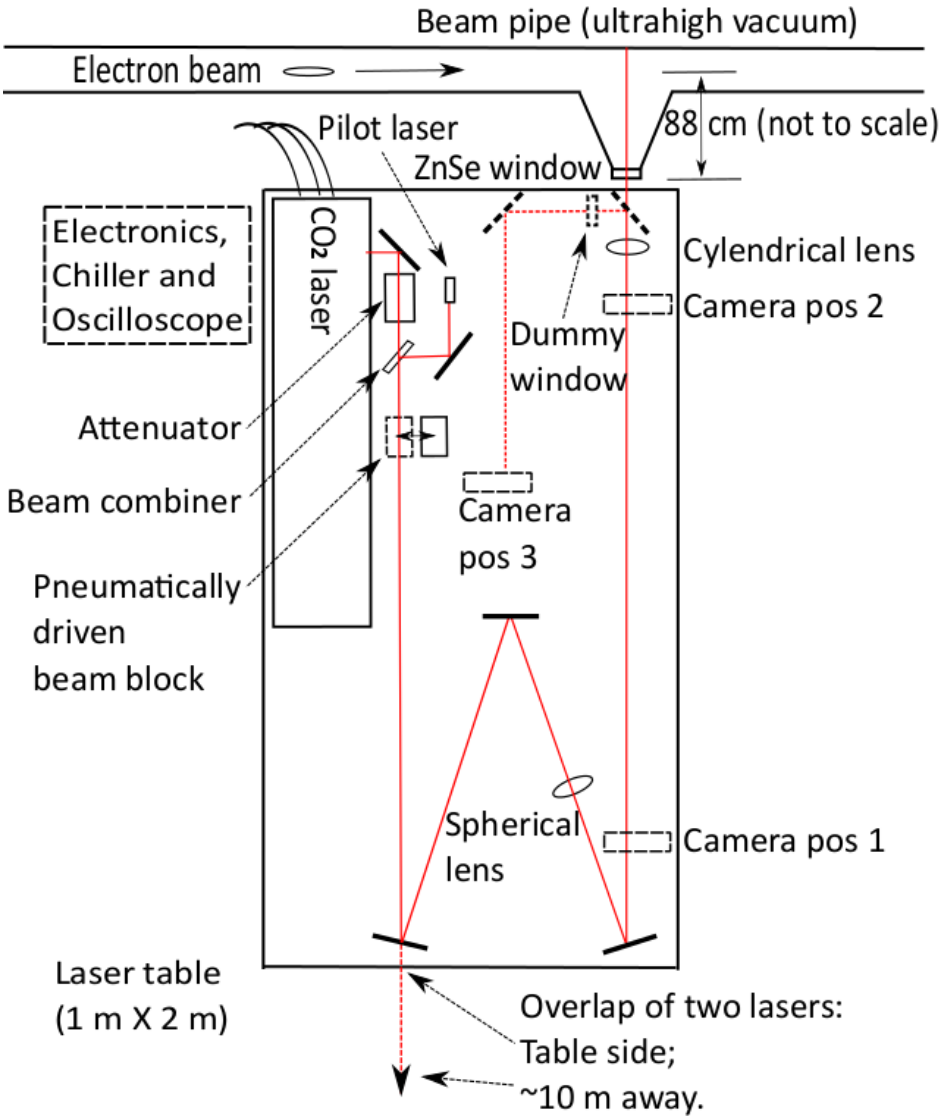

Figure 3.8: Design and layout of CO_2 laser and optical system.

3.2.1.3 Beam size simulations for different collimation lenses

A numerical calculation was performed using a commercial program, Optics Software for Layout and Optimization (OSLO 6.6.2, EDU edition [67]), based on the parameters given in section 3.2.1.1 to optimize the position and focal length of the collimation lens. The focal lengths of the collimation lenses are considered to be 2 m, 2.5 m, 2.7 m, 3 m and 4 m. According to the numerical results shown in Fig. 3.9, the Gaussian beam radius achieved at the focal plane agrees well with the theoretical calculation based on Eq. 3.1. The optical elements along the simulated optical path are the spherical collimation lens, the cylindrical focusing lens and the ultrahigh vacuum ZnSe window. Since the cylindrical lens only focuses in the vertical direction, we can clearly see the horizontal beam size remains the same in the left column of Fig. 3.9. For the 4 m collimation lens, the horizontal beam radius is even bigger than the radius of the window clear aperture. The comparison and selection among these scenarios including clipping effect will be presented next section.

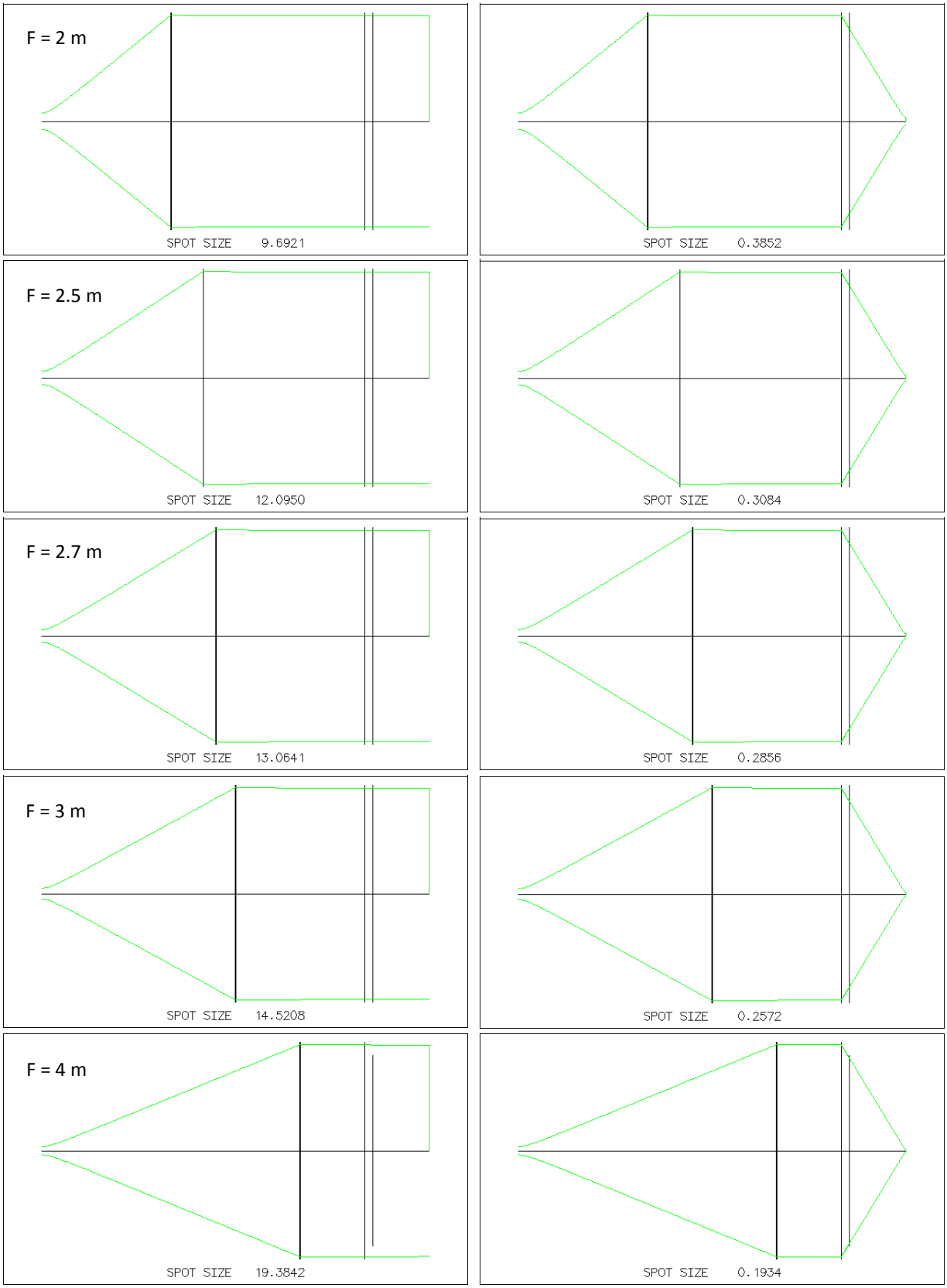

Figure 3.9: Simulation of beam sizes along the optical path. The simulated optical elements (from left to right) are the collimation lens, the cylindrical focusing lens and the ZnSe window. The focal lengths of the collimation lenses are 2 m, 2.5 m, 2.7 m, 3 m and 4 m (top to bottom). The left column shows horizontal plane and the right column is vertical plane. The final spot sizes are in mm.

3.2.1.4 Influence of clipping apertures

The main reason we chose these different focal lengths for the collimation lens is the limitation of the clear aperture size of the ZnSe vacuum window. It is well known that even relatively large hard edge apertures that transmit high percentages of power can lead to considerable diffraction effects blurring the focal spot [68].

Specifically, as calculated in [69], if the clipping ratio *a/w* (*a* is aperture radius, *w* is the beam radius defined as intensity drops to $1/e^2$) equals to 2, the focal spot radius only enlarges by 2%, the peak intensity is largely preserved. If a/w is 1.5, around 99% power can still be transmitted, but the focal spot radius enlarges already by 12%, making the peak intensity drop to around 80% of the one achieved by an unperturbed laser beam. For the situation with *a/w* = ~1, not only the focal beam radius increases by 46%, but also only 86% beam power can pass through the aperture, leading to peak intensity of only ~40%. Additionally, this shifts the position of the focal plane towards the focusing lens.

In our setup, as summarized in Table 3.1, the larger focal length of the collimation lens leads to bigger laser beam size on the focusing lens. However, for the vertical plane, our window has a 35 mm diameter clear aperture, while for horizontal plane, apertures in the ion pump housing has only 28.8 mm opening (see section 3.1.1). With a 2 m focal length collimation lens we can achieve a clipping ratio of around 2 at the window, and finally focus the beam to around 390 μm focal spot radius. For a focal length of 4 m, the theoretical focal spot radius would be around 200 μm, but since the clipping ratio would be around 1, the real value would be around 280 μm including the enlargement of 1.46 from the clipping. It is still much smaller than 390 μm achieved by the collimation lens with 2 m focal length. However, only 76% beam power gets transmitted, and with such severe diffraction it is hard to control the focusing beam quality and the focal plane position.

Table 3.1: Estimation on the influence of aperture clipping (aperture sizes: 35 mm for the vertical plane, 28.8 mm for the horizontal plane).

Focal length of the collimation lenses (m)	4	3	2.7	2.5	2
Vertical laser beam radius at the window (mm)	17.0	12.8	11.5	10.6	8.50
Collimated horizontal laser beam radius (mm)	19.4	14.5	13.1	12.1	9.68
Vertical clipping ratio	1.03	1.37	1.52	1.65	2.06
Horizontal clipping ratio	0.742	0.993	1.10	1.19	1.49
Theoretical vertical focal radius (μm)	193	257	286	308	385
Vertical enlargement factor [69]	~1.46	~1.20	~1.12	~1.08	~1.02
Expected actual vertical focal radius (μm)	~282	~308	~320	~333	~393
Estimation of total transmitted power	~76%	~92%	~95%	~97%	~99%

As the envelop to cover all the electron vertical beam sizes at different energies and operation modes should be around 300 μm, and also the transmitted power should be above 90%, thus the 3 m collimation lens is the optimum with the expected vertical focal radius of around 308 μm. In order to guarantee that the clipping/diffraction effect does not influence too much, the collimation lenses with 2.7 m and 2.5 m focal lengths are also chosen as backups.

3.2.1.5 Profile of the focal spot and vibration measurement

As we can see from Fig. 3.10, the measurement at the virtual focal plane (see Fig. 3.7) yields a ~320 μm vertical beam radius (2σ, $1/e^2$ radius), which agrees well with the design value in Table 3.1. Since the horizontal beam size is already larger than the camera aperture, it cannot be determined properly by the camera.

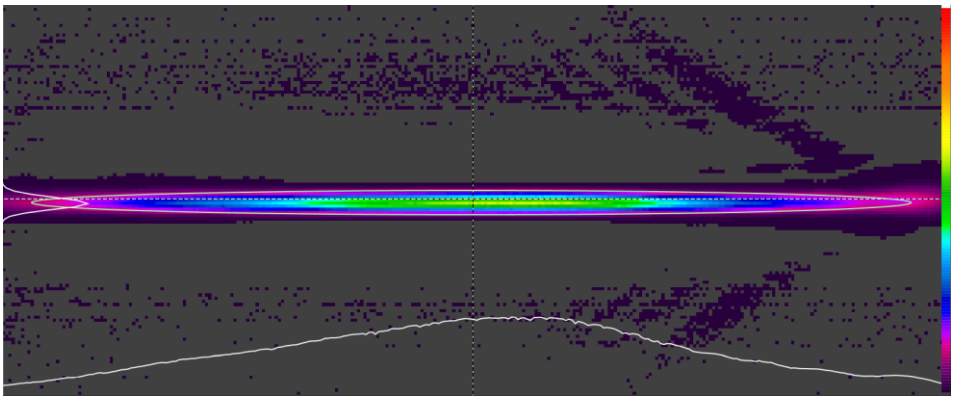

Figure 3.10: Profile of the laser focal spot with horizontal size much larger than the vertical size.

We can also monitor the long term drift of the beam centroid using the camera. The camera can register light intensity at every pixel, and calculate the centroid position of the beam profile instantly. Fig. 3.11 shows the probability density distribution of laser vertical centroid positions recorded in 30 minutes and the data-taking frequency is 1 Hz. One sigma of the vertical centroid position by Gaussian fit is 15.9 ± 0.3 μm. It is only 1/10 of the vertical beam size, therefore the laser focal spot is relatively stable in the vertical plane.

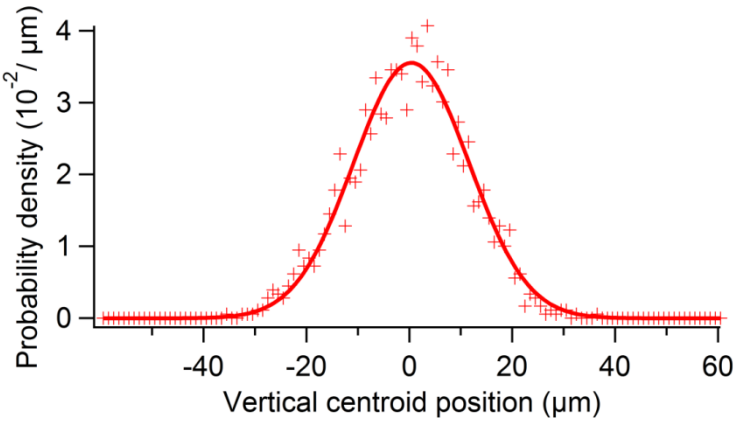

Figure 3.11: Long term (one hour) measurement of the beam centroid position.

3.2.2 High Purity Germanium detector and the detection system

In this section, the basic working principles, especially the detection efficiencies of the gamma ray detectors will be introduced. The HPGe spectrometer is selected based on comparison among different types of detectors. The characteristics of such HPGe detector will be depicted in details. Its shielding and supporting system will be presented as well.

3.2.2.1 Basic principles of gamma ray detectors/spectrometers

In order to measure the energy of an incident gamma ray, the gamma ray has to interact with certain kinds of materials in the detector head, and transfer part or all of its initial energy to this material to generate an electron cloud/cluster along the propagation path, which is then collected by the detector as an electrical pulse. The amount of electrons or the amplitude of the pulse is proportional to the energy transferred from the initial gamma ray and can therefore be used to measure the gamma ray energy recorded by the detector. The distribution of the photon intensities sorted by their recorded energy is called energy spectrum.

Because of the electromagnetic nature, gamma rays mainly interact with the detector material in three ways: the photoelectric absorption, the Compton scattering and the pair production. With increasing gamma ray energy, the dominant mechanism changes from the first to the last one. Since all three effects involve interactions with material atoms and their electrons, high atomic number, large active volume and high material density material would be in favor of high interaction probabilities and therefore lead to good detection efficiencies.

There are mainly two ways to define the detection efficiency, one is based on absolute efficiency / intrinsic efficiency, the other is defined as total efficiency or full energy peak (peak) efficiency.

The absolute efficiency describes the percentage of the pulses recorded by the detector relative to the amount of all the gamma rays emitted by the radiation source. If the efficiency only describes the proportion of the pulses recorded relative to the gamma rays actually impinging on the detector, without including the geometry factor describing the solid angle of the detector facing the source, then it is called intrinsic efficiency.

The total efficiency counts every pulse recorded by the detector, no matter how small the amplitude is, while the peak efficiency just counts those pulses that are generated by the gamma rays that deposit all their initial energy in the detector. These peak pulses normally form a narrow full energy peak on the spectrum, while the other pulses with only a fraction of the initial gamma ray energy appear as the continuum to the left of the full energy peak on the energy spectrum, as shown in Fig. 3.12. More details of spectral features can be found in [52].

The total efficiency and the intrinsic efficiency can be calculated easily from each other, as long as the geometrical relationship between the detector and the radiation source is known. In order to relate the total efficiency and the peak efficiency, we have to include a parameter known as the “peak to total ratio”, which is, however, not always available in the detector specification.

Thus, there are four definitions: the absolute total efficiency, the absolute peak efficiency, the intrinsic total efficiency and the intrinsic peak efficiency. As for our measurement, the intrinsic peak efficiency is the most useful value since our signal photons (CBS gamma rays at the Compton edge) are very collimated along the propagation axis and nearly all of them can hit onto the detector surface. The peak efficiency contains the information about the proportion of the edge photons produced at the CBS process with their entire energy recorded by the detector.

The full energy peak normally has a finite spectral width, and its Full Width Half Maximum (FWHM) is called energy resolution when detecting a monochromatic radiation source. Conventionally, often the percentage of FWHM divided by the central peak energy E_0 is used as the detector resolution. In this thesis, we will call the percentage expression the relative energy resolution.

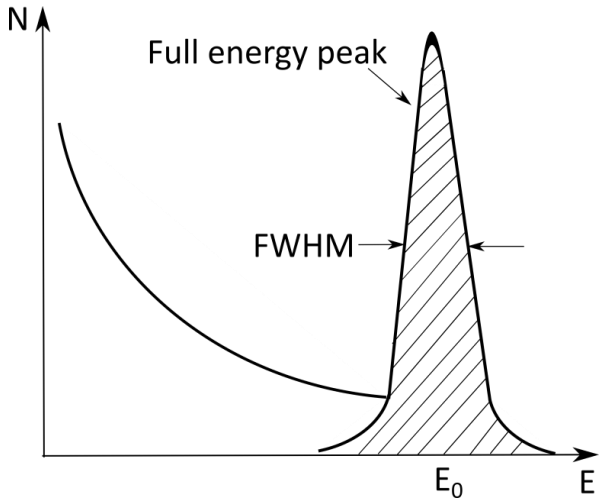

Figure 3.12: A typical energy spectrum of monochromatic gamma rays recorded by a gamma ray detector.

3.2.2.2 Selection of the gamma ray detectors

There are typically two fields involving detection of gamma rays, one is normally dealing with extremely high energy gamma rays such as high energy physics, the other is detection with medium to high energy gamma rays for nuclear radiation analysis.

Typically, the relative spread of the Compton edge (the width of the Compton edge divided by its average energy) from the CBS collision between the frequency-stabilized CW laser and the electron bunch in the storage ring is around 0.1%. But on the spectrum, every count given by the detector includes a convolution with the detector energy resolution. In order to detect such narrow edge on the spectrum, a spectrometer with good energy resolution and comparably high detection efficiency is required.

For the detection of extremely high energy gamma rays, e.g. the lead glass Cerenkov counter, such as the ones in the OPAL detector at LEP [70], can be used. Its intrinsic energy resolution is $\sigma_E/E \cong 5\%/\sqrt{E}$, where E is the photon energy in GeV. So the electron beam energy needs to be as high as possible to reach a relatively good energy resolution, as the Compton edge energy is proportional to γ^2 and the laser photon energy (γ is the Lorenz factor, see Eq. 2.3). From the discussion in the section of booster, it is probably practical to use 400 - 500 nm visible lasers as for

our setup. If we shoot such laser to scatter with the 2.5 GeV electron beam at ANKA, the Compton edge energy of the scattered photons would be around 120 - 150 MeV (perpendicular scattering) or 240 - 300 MeV (head-on collision). As a result, the relative energy resolution σ_E/E of the lead glass counter is still larger than 10%. If we adopt it as our detector, the relative Compton edge width in Eq. 2.8 would be ~100 times larger than that by an HPGe detector. Moreover, the photon energy of the visible laser is more than 20 times higher than that of CO_2 laser, thus the visible laser power needs to be ~20 times higher to achieve the same amount of photons to scatter with electron beams. To realize such scenario, the required laser power is already too large, not to mention such wide Compton edge (or "slope") would interfere with single and double escape peak on the spectrum, making it hardly feasible to determine its average energy precisely.

For the recent proposed FCC-ee project with up to ~400 GeV electron beam or FCC-hh with up to ~100 TeV proton beam, γ is ~10^5. If we shoot ~500 nm laser antiparallel onto the particle beam, the resulting Compton edge would achieve ~100 GeV, then the relative energy resolution of such lead glass counter can achieve 0.5%. The required laser power and detection efficiency as well as the signal to noise ratio have to be further carried out to realize such precise energy monitor.

Besides the extremely high energy detectors normally used for high energy physics, there are many other detectors for nuclear radiation analysis, mainly in three categories: gas filled detectors, scintillation detectors and semiconductor detectors (or solid state detectors). Details about their properties, structures and working principles, etc., can be found in [71][72][52]. As for the energy resolution, since on average it only needs several eV to create a charge carrier in the semiconductor detectors, a gamma photon with its energy fully deposited, can typically generate about one or two orders of magnitude more charges in semiconductor detectors than in gas detectors or scintillation detectors respectively. The more charge carriers means less relative statistical fluctuation on the electrical pulse amplitude. Therefore the semiconductor detectors have much better energy resolution compared to the other two types of detectors intrinsically.

Although the gas detectors, such as HPXe, have better energy resolution than the scintillation detectors, they are still inefficient for detection at ~several MeV. In consideration of both the typical energy resolution and the detection efficiency including available detector size, among all the commonly commercial detectors listed in the comprehensive comparison in [73], NaI:Tl on behalf of the scintillation detectors and HPGe on behalf of semiconductor detectors are preferable to our measurement setup. The commonly used scintillator detector (e.g. NaI:Tl) has high intrinsic efficiency and also can be made with very big size, but the energy resolution is inferior compared to the HPGe. However, according to Eq. 2.6, a detector with large energy resolution would give wider Compton edge, but if it has higher detection efficiency, it can achieve the same statistical uncertainty at determination of the Compton edge energy. For example, HPGe has ~30 times better resolution than NaI:Tl for MeV scale gamma detection, in order to adopt NaI:Tl to achieve the same statistic uncertainty for determination of the Compton edge energy, either ~30 times higher scattered photon intensity, or NaI:Tl with a ~30 times higher detection efficiency is required. Since our HPGe is ~40% relative efficiency compared to 3 in dia. × 3 in long NaI:Tl, it means we need a NaI:Tl with ~4000 cm^3 volume, which is still much smaller than the manufacture capacity (crystals with volume up to 75 cm dia. × 25 cm length has been produced [72]. Our measurement is somehow feasible with a big NaI:Tl detector, but special care should be taken for the curve shape of the Compton edge since now the edge should be more than 100 keV wide, which might interfere with

some other radiation patterns on the spectrum, therefore lead to the difficulties in determining the Compton edge energy by curve fitting.

Among semiconductor detectors, there are several other types like CdTe detectors, which can compete with HPGe regarding energy resolution. But these types are typically made for X-ray or gamma ray detection below several hundreds of keV due to its small volume normally available. The HPGe gives the best energy resolution, and can be made very large commercially (~200% relative efficiency [72]). The typical detectable energy range is 40 keV - 10 MeV, and can be much extended to 3 keV or even below 1 keV at the low energy region. Although HPGe must be cooled in the liquid nitrogen or electronically during measurement and hardly suitable as portable devices, it still serves well under our detection conditions.

In summary, regarding energy resolution and detectable energy range, the best detector for our measurement would be HPGe spectrometer.

3.2.2.3 Configuration of the HPGe spectrometer

Our detector is from ORTEC (GEM-M5970, relative efficiency: 38%, crystal profile: 58.2 mm dia. × 74.2 mm length contour with a 10.5 mm dia. × 61 mm length hollow core, energy resolution FWHM @1.33 MeV: 1.9 keV), together with a 7 liter dewar, making it a very compact configuration. The dimension of the whole profile can be seen in Fig. 3.13. The detector crystal has a bigger length to radius ratio compared to other models, making it especially suitable for detection of our highly collimated CBS gamma beam at ANKA.

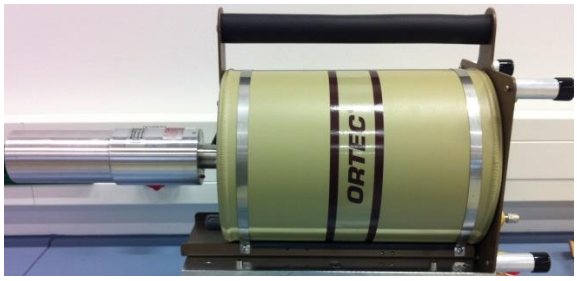

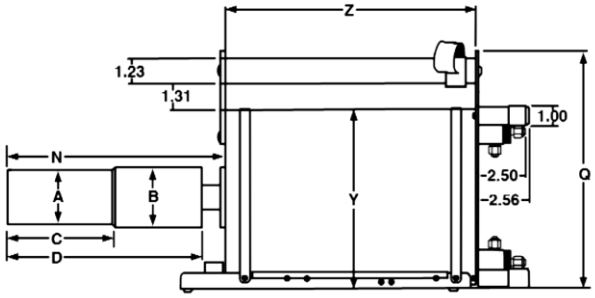

	A	B	C	D	N	Q	Y	Z
Dimension / mm	70	75	134	246	278	302	229	320
Tolerance / mm	0.3	0.3	5	8	10	13	5	5

Figure 3.13: HPGe detector with dimensions. [74]

The relative efficiency is very common expression of HPGe detection efficiency. Its definition is the absolute full energy peak efficiency at the detection of 1.33 MeV gamma radiation line emitted by a point source ^{60}Co located 25 cm away from the detector front surface, over the absolute peak efficiency of a 3 in dia. x 3 inch length NaI:Tl detector under the same geometrical conditions (the value is 0.0012). The relative efficiency serves as a good indicator of the detection efficiency of the HPGe at 1.3 MeV, also can be used to estimate the detector's crystal volume. But the diameter tends to have a bigger influence on the relative efficiency over the length, since the result is from measurement of a point like source.

As we can calculate geometrical factor based on the crystal profile and ^{60}Co point source, we can get the nominal intrinsic peak efficiency of our HPGe as ~13% at 1.33 MeV when detecting the point source 25 cm away, which may be still smaller than the actual performance since our detector may have better detection for our highly collimated radiation.

3.2.2.4 Basic working principles

HPGe is a semiconductor detector. It converts photon energy to generate electrons and holes as charge carriers which are eventually collected by the electrodes. The basic properties and physical process in the detector crystal is similar to that of semiconductor solar cell. The crystal profile can be seen in Fig. 3.14. It is a commonly used coaxial configuration (with one end closed) to achieve a big active volume for ~MeV gamma ray detection. The germanium is P-type material, together with a ~700 μm lithium diffused layer at the outer surface, which serves as electrode (the N+ contact), to form a p-n junction. The other electrode is a 0.3 μm boron ion-implanted contact layer (the P+ contact) located at the inner surface. A very high reverse voltage (2600 V) is applied onto the p-n junction, completely expanding the depleted region to the whole crystal. The depleted region acts as the active volume. If the incident photons interact and produce electron-hole pairs in the depleted region, the strong electrical field would sweep them to the collection electrodes (the N+ and P+ contact layers). Due to the very small band gap of Ge, it needs to be cooled in the liquid nitrogen to reduce the leakage current of thermally generated charges to an acceptable level. Since the outer surface of the crystal has a relative thick dead layer together with another ~1 mm aluminum shell covering the crystal, the gamma rays with energy less than 40 keV can hardly be detected.

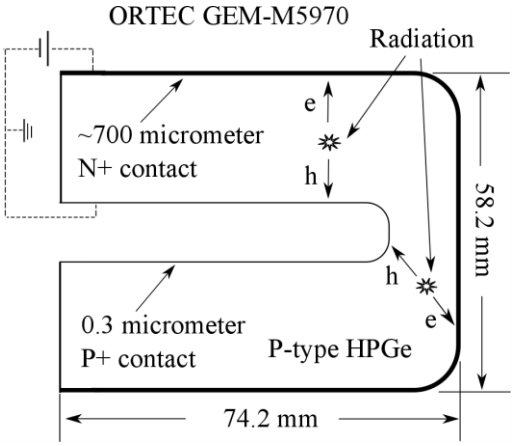

Figure 3.14: Crystal profile of ORTEC GEM-M5970 HPGe detector.

When the external electrical field is high enough, the drift velocity of the electron reaches the maximum of 10^7 cm/s, which makes the typical collection time for the coaxial type crystal 10^{-7} - 10^{-6} s [75] (depending on the specific profile of the crystal and the locations where the charge carriers are produced). It is still much less than the average life time of the charge carriers in HPGe (~10^{-5} s). After all the charges generated by the incident gamma ray are collected, the electrical pulse will first be amplified by the preamplifier closely followed afterwards, then further analyzed by a Multi-Channel Analyzer (MCA). The preamplifier inside the detector head amplifies the pulse to several millivolts of amplitude but with a very long pulse tail (~50 μs), reduces the noise and optimizes the coupling between the detector and the MCA. The MCA (DSPEC 50) is connected to the detector head through cables, and mainly consists of an amplifier, an Analog-to-Digital Converter (ADC) and its memory.

The amplifier will further amplify the pulse to 0-10 V positive amplitude and also optimizes the pulse shape via proper shaping circuits to achieve short duration (~several μs) and better signal to noise ratio. Then the ADC digitizes the pulse amplitude with its height value further sorted to a corresponding channel number. The pulse counts in every channel are stored in the memory, shown or analyzed as the energy spectrum collectively or as in a list mode separately.

The shaping circuit shapes the pulses to a quasi-trapezoid, which consists of a rise time side (0.8 - 23 μs), a top base (0.3 – 2.4 μs, normally with a tilt), a fall time side (same as the rise time) as we can see Fig. 3.15. The optimum shaping rise time should be longer than the pulse rise time from the preamplifier, which normally stands for the charge collection time in the detector crystal. Ideally if shaping time constants are towards infinite, the amplitude of all the preamplifier pulses can reach their maximum. But when the rise time is reduced and comparable to the rise time of the long preamplifier pulses from very slow charge collection, a small part of the full amplitude cannot be preserved and therefore the energy resolution deteriorates. The effect is called the ballistic deficit [71]. The situation is especially serious for a large volume detector, since the large variation of charge collection time can be caused by different locations of the radiation interaction. So the optimum shaping times need to be many times greater than the average collection time in the crystal [71], but too long shaping times would also include too much noise, thus worsen energy resolution as well. Also for high count rate measurement often short rise time is chosen to reduce the dead time and the pile up effect.

After the shaped pulse reaching its maximum, ADC starts to digitalize and convert its amplitude to a channel number and put it to the memory. The whole process from the beginning of the rise time to the completion of memory registration is called detector dead time. During this period the detector refuses any other pulse coming upon. The real time is the total measurement duration. The live time is the real time minus the dead time, which stands for the duration the detector is waiting to process next pulse. Often the dead time is expressed in the percentage way of the absolute value of dead time divided by the real measurement time. Furthermore, through the enhanced throughput mode we can minimize the dead time to be 2 × rise time + 2 × flattop (shown in Fig. 3.14).

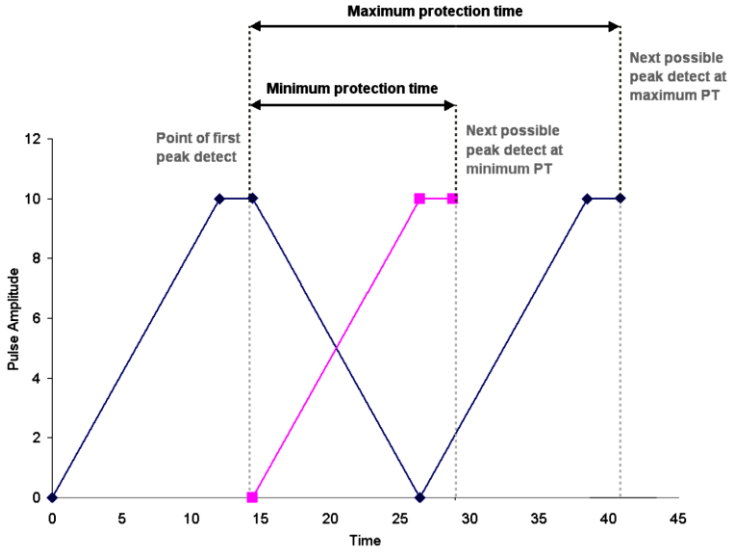

Figure 3.15: Illustration of pulse shaping times. [75]

3.2.2.5 High count rate performance

As we have a standard resistor preamplifiers from ORTEC with an energy rate limit of 1.45×10^5 MeV/s, if on average every gamma photon that enters the preamplifier has 1 MeV energy, then beyond the maximum incident rate of 1.45×10^5 /s, the preamplifier will be saturated. But normally the electron beam current at ANKA can be well adjusted to suit our measurement.

If we need to measure the full current at ANKA, the Transistor Reset Preamplifier (TRP) has to be adopted in the HPGe. Although the TRP works without saturation, it increases dead time therefore registers fewer counts compared to the resistor preamplifier below its saturation point.

For high count rate measurement, actually even before the saturation, the signals begin to be too closed together for the detector to distinguish their pulses, which is called pileup effect. These bad signals are rejected and not useful. When the incoming signal rate increases, the throughput (i.e. number of useful events stored in the memory per second) goes up but the increasing rate decreases, and it will reach the maximum level at certain point, further increase of incident signals will even reduce the amount of the useful signals that could have been stored in the spectrum due to the pile up effect. Thus for high count rate measurement, the detection efficiency can be even much worse than that of low count rate measurement.

There is a tradeoff between the high throughput and the good energy resolution that can be achieved. We can get higher throughput by choosing shorter pulse processing time (shorter dead time), but it might worsen energy resolution for ballistic deficit. To find optimum shaping times for a specific measurement condition, a series of tests for comparison need to be carried out, but when the measurement condition changes (e.g. the various electron beam current, energies, operation modes and collimator positions, etc. at ANKA), the optimum shaping time probably changes accordingly. Fortunately, the influence of the optimum shaping times is not very critical for our measurement, since the low throughput or the degraded energy resolution can be compensated by longer accumulation time.

As we can see [76], for the dead time round 2.2 μs, when the incoming signal rate is around 10^5/s, it reaches the optimum throughput above 4×10^4/s. As we can see in section 4.1, the count rate of detected gamma rays given by 10 mA electron beam at 1.3 GeV and 20 W laser is estimated to be ~10^4 /s, which is much below the optimum throughput point, thus the pile up effect can be neglected if we choose such short dead time. However, for such short dead time, the rise shaping time can only be ~1 μs, probably leading to a certain degree of the ballistic effect.

3.2.2.6 Design of the supporting and shielding system

As we can see in Fig. 3.16 and Fig. 3.17, the size of the detector table is optimized to fit in the narrow space at the front-end area of the XSPEC beamline. In order to minimize radiation background during measurement, the detector head is covered with lead shielding blocks of 5 cm on the sides and 10 cm in the front. The 2 blocks in the front have a hole of 10 mm on axis. The 5 blocks at the back have central holes of 100 mm diameter to accommodate the detector head. The whole setup is located on a thick Al plate, which can be translated and rotated with small amplitude by the screws at the

sides and the bottom. The screws are connected to the table below. The Al plate has several 12 mm (dia.) holes for pre-alignment with the laser tracker regarding the reference line set by the quadrupoles.

The collimator is a 130 mm × 100 mm × 30 mm tungsten block with 4 mm, 5 mm, 6 mm and 7 mm diameter tunnels for our signal beam going through while absorb other background radiation in different directions, see Fig. 3.18. There is an intensity absorber 4 meters away in front of the collimator. Since the horizontal opening of the intensity absorber is only 6 mm, 7 mm dia. tunnel is already large enough to cover the entire signal beam coming through the absorber (see section 3.2.3). The collimator is installed onto a sturdy motorized translation stages from ISEL Germany AG with the two moving range of 490 mm in both horizontal and vertical direction. The ISEL stages enable us to scan one collimator tunnel during measurement to maximize the incident signal rate or change the collimator tunnel to further increase or decrease radiation count rate. Also we can block the incoming radiation completely with the collimator block to protect the detector. The collimator can be further aligned to the incoming radiation with the laser tracker.

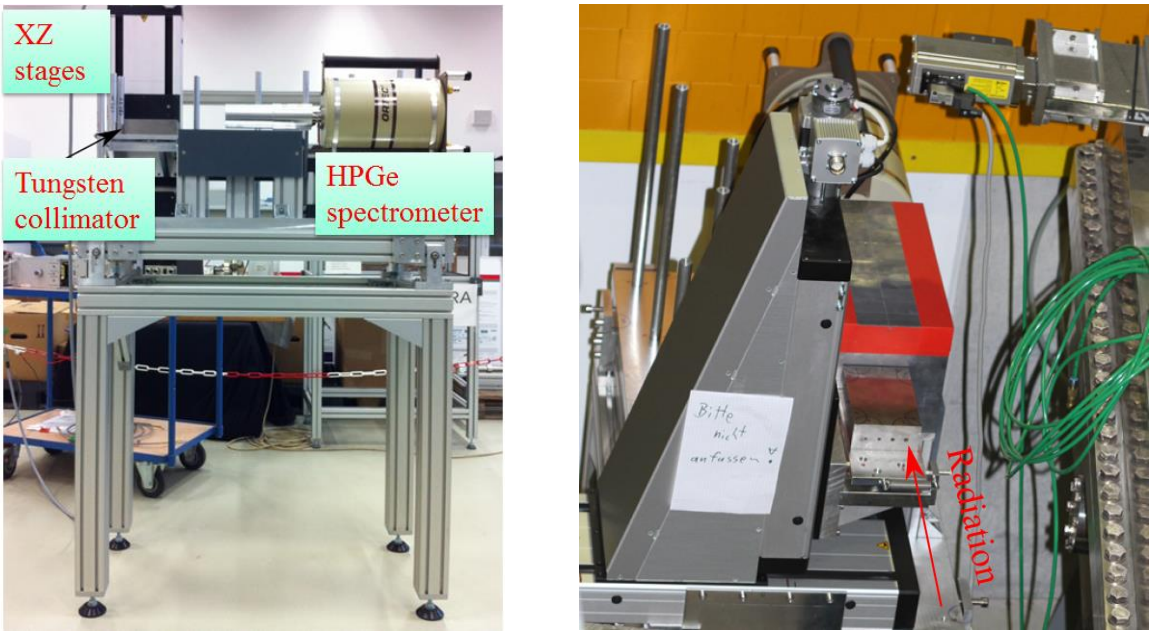

Figure 3.16: Detection system at the front end area.

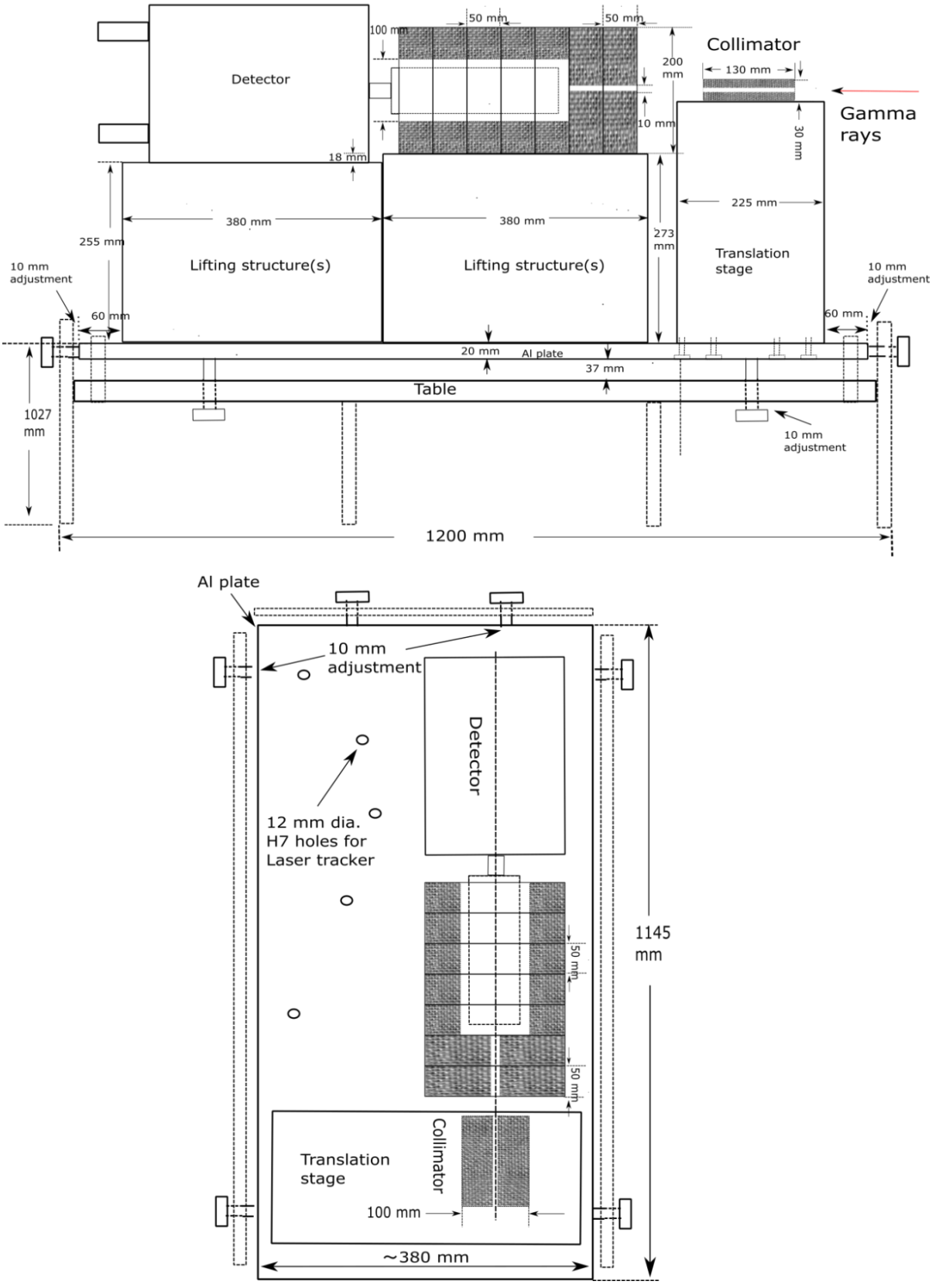

Figure 3.17: Layout of the detection table.

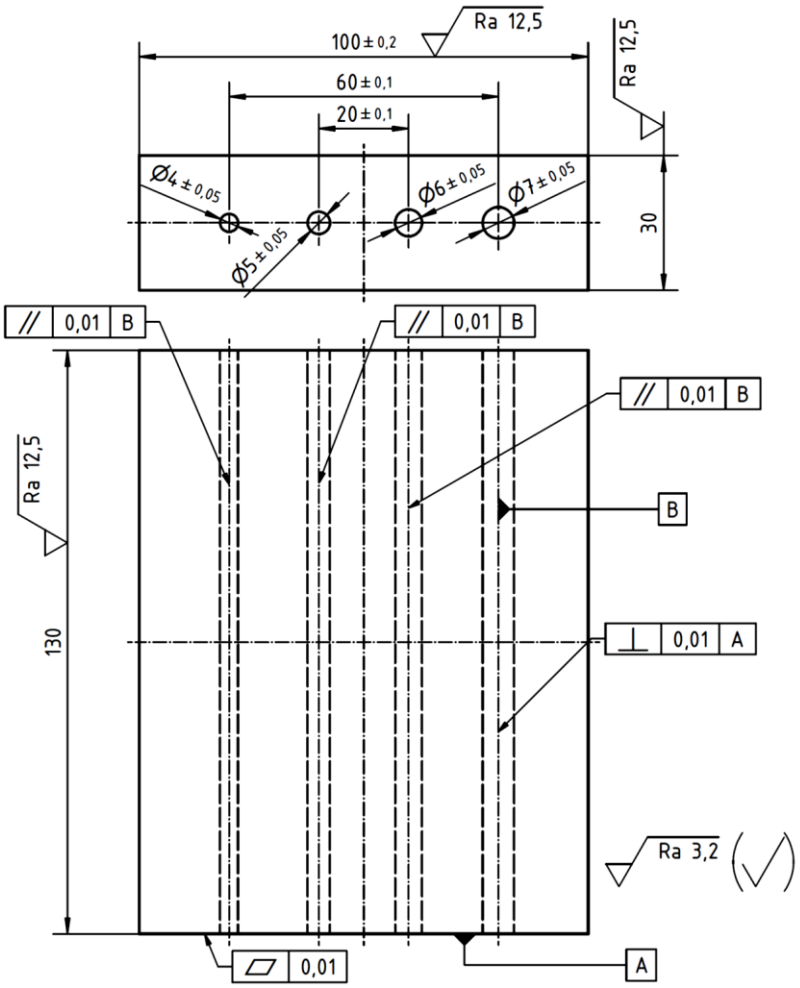

Figure 3.18: Design of the tungsten collimator.

Table 3.2: Remaining energy of gamma rays (percentage) passing through three materials of 10 cm thickness.

Energy / MeV	Iron	Lead	Tungsten
0.2	0.0224	1.23 E-29	8.44 E-42
0.5	0.101	3.20 E-05	6.03 E-07
0.6	0.107	4.38 E-04	1.81 E-05
0.8	0.118	5.16 E-03	4.29 E-04
1	0.129	1.59 E-02	1.83 E-03
1.25	0.143	3.38 E-02	4.92 E-03
1.5	0.156	5.01 E-02	8.38 E-03
2	0.177	6.88 E-02	1.30 E-02
3	0.200	7.19 E-02	1.35 E-02
4	0.209	6.22 E-02	1.06 E-02
5	0.210	5.24 E-02	7.97 E-03
6	0.208	4.45 E-02	6.10 E-03

As we can see the proportion of the photon energy transmitted through the three shielding material of 10 cm thickness summarized in Table 3.2, (the mass energy-absorption coefficients are from [61]), our design with the combination of 10 cm lead shielding blocks and 13 cm tungsten collimator can nearly stop all of the incident CBS photon energy, minimizing the non-signal radiation during measurement, sparing the limited detector live time for detection of the Compton edge photons.

3.2.2.7 Further discussion on instrumentation

If there is possibility that some beamline could accommodate the HPGe defector (some models have the design with detector head detachable from the Dewar), it is not necessary to have such detection table as well as the corresponding collimator and shielding structures, since the beamlines can already select the radiation size with motorized slits, like the IMAGE beamline we have used to detect the bremsstrahlung background, see section 4.3.

As for the laser coupling location, it only needs to be along the straight beam pipe between the bending magnets (not necessarily at the long/short straight section with insertion devices and acceleration cavities).There are normally several side ports of the ion pumps as we used at the current setup, and available free space for the laser table. Furthermore, if we adopt the compact commercial laser provided by Access Laser or remove away the cover box of the current laser we used, the size of the laser table can be further reduced to the half of its current size, provided that an beam expander is integrated into the design to adjust the input beam size on the focusing lens, see section 3.2.1.2. The S/N ratio can be further improved since beam pipe with shorter length has much less bremsstrahlung radiation than the current long straight section.

3.2.3 Coupling ports of the CBS photon beam

As shown in Fig. 3.19, the extension from synchrotron at the front-end area consists of a crotch absorber, an intensity absorber, a fast closing valve and a homemade copper end flange with central 10 mm dia. × 2mm thick plate. There is cooling water going around the copper end flange and the thickness of the central plate is minimized to let large portion of the Compton edge photons passing through it (~90% transmission at 1.3 GeV electron beam).

The crotch absorber has an opening of 50 mm (horizontal) × 5 mm (vertical) for the out coming radiation. The electron beam profile at ANKA is very flat with vertical rms size of ~100 μm and horizontal rms size of ~1000 μm, see section 4.1. The highly collimated Compton edge photons have nearly the same profile as the electron beam. Thus the opening of the crotch absorber is enough to let the signal beam pass through.

The opening of the intensity absorber is 10 mm vertically. However, the horizontal size is only 6 mm, which is nearly the same as the size of our signal beam. The top view of the intensity absorber copper block can be seen in Fig. 3.20. Moreover, the intensity absorber is misaligned by several mm towards the concrete wall (based on the laser tracker measurement, ~3-4 mm translation misalignment relative to the reference line set by the two quadrupole centers at the long straight section with additional tilt and rotation possibilities), making it extremely hard to get the signal beam through. During measurement we have to apply a very big local bump at the collision point to let most of our signal beam circumvent the absorber with a large propagation angle, see section 5.2.2.

With the cone shape of the opening, if photons hit on the edge of the absorber, they still can possibly pass through, and the transmitted proportion depends on the incidence position. For example, if the Compton edge photons with ~1.5 MeV strike on the middle of absorber cone, after passing through ~31 mm copper there are still 26% photons transmitted, but if the photon hit on the very beginning of the cone, after passing through ~62 mm copper, there are only 7% photons left without interaction. However, the scattered photons do not lose all of their energy to the copper block, some of them may also pass through with reduced energies and altered angles. The ones with slightly altered energies received by the detector would possibly enlarge the Compton edge width and affect its shape, therefore influencing determination of its average energy, see Chapter 5 and 6.

The collimator in front of the detector also has to be moved around to the "right" position, neither receiving too much of the bad signals hitting on the absorber, nor cutting off too much good signals. Misjudge of the collimator position or measuring without such local bump would cause a shape deformation or a much widening of the Compton edge, influencing our precise determination of the energy. But such engineering difficulty has nothing to do with the principle of the method itself and can be very well corrected. However a proper realignment must alter the magnet positions with big influence on the electron beam orbit and downstream beamlines, therefore the significant efforts and time involved exceeds the time window for this thesis.

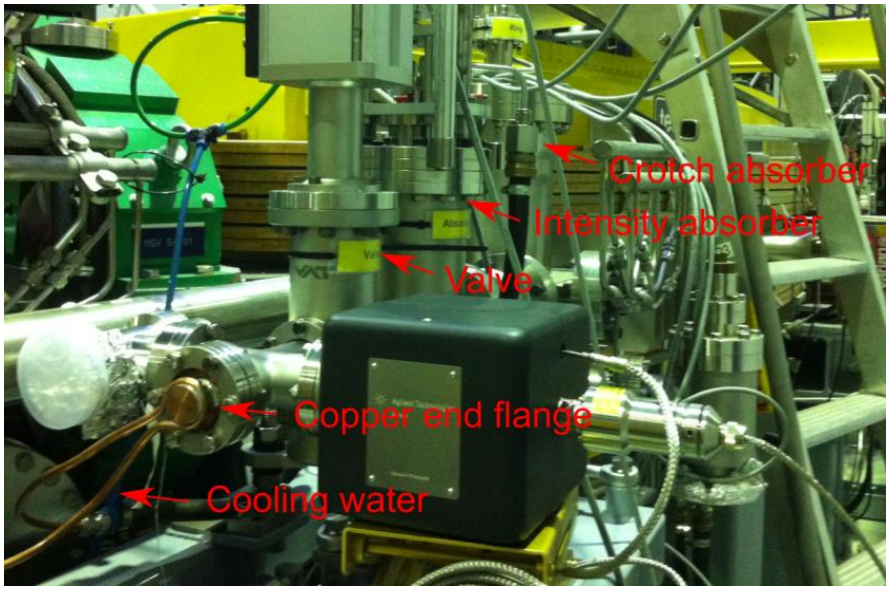

Figure 3.19: Out coupling port of CBS photons.

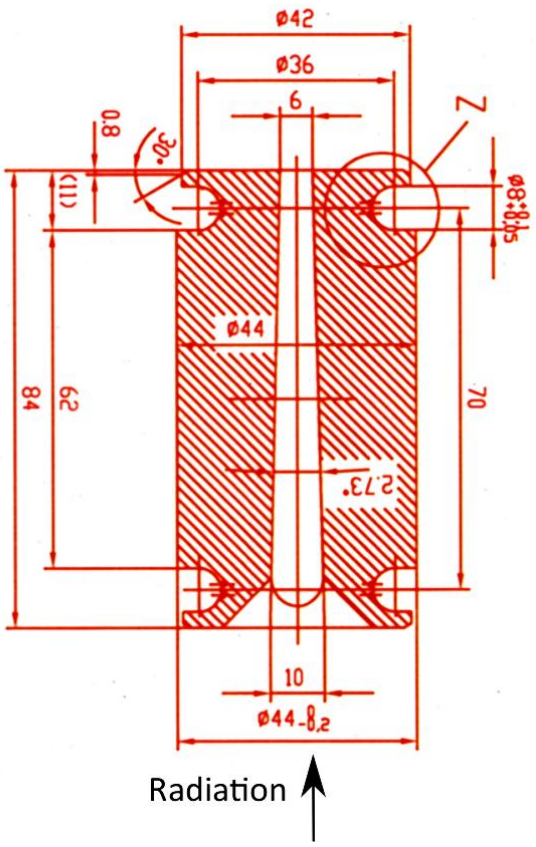

Figure 3.20: Copper block of the intensity absorber.

4. Simulation studies and background measurement

After we obtain the simulation results of the CBS photons, applying the mathematical model of the curve fitting to the simulated spectrum at the Compton edge, we can predict the influence of the misalignment of the collimator. Furthermore, by comparison of the background measurement and CBS photon simulation, we can obtain the expected signal to noise ratio, which is critical for our transverse setup compared to the conventional head-on collision.

4.1 Simulation of CBS photons

Based on the configuration and setups discussed before, we can study the characteristics of the CBS photon beam similar to that on the booster ring in Chapter 2. As for the basic electron beam parameters at different energies and operation modes, we can obtain them from Accelerator Toolbox (AT) of Matlab. Then we can obtain the characteristics of the CBS photon beam with CAIN2.42.

4.1.1 The transverse setup for the normal optics at 1.3 GeV

The basic parameters and configuration needed for simulation can be summarized in Table 4.1. The vertical focal spot size of the laser is taken from the measurement with the camera, and the horizontal size is from the simulation since it is too big for the camera aperture. The horizontal laser beam size does not have to be very accurate since the scattering process is insensitive to it, as we can see later in this section.

Table 4.1: Parameters of the transverse setup for the normal optics at 1.3 GeV.

Electron beam		Laser and Detector	
Current / mA	10	Wavelength / μm	10.23
Energy / GeV	1.3	CW laser power / W	20
Vertical size (RMS) / μm	~50	Vertical size (RMS) / μm	160
Horizontal size (RMS) / μm	689	Horizontal size (RMS) /μm	~7250
Bunch length(RMS) / ps	21.1	Polarization	Vertical
Energy spread (RMS)	4.76×10^{-4}	Collision angle	91.6°
Emittance / nm × rad	H: 27.5	Collimator's position after the CP / m	9.2
	V: ~0.3	Accumulation time / min	10

For the vertical emittance of the electron beam, assumption has been taken that it is ~1% of the horizontal value. Although based on the vertical beam sizes measured with Synchrotron Light Monitor (SLM) [77]] and conversion of β functions at the SLM and our collision point, the measured value tends to be smaller than the ~1% assumption adopted here. However since we have to take into account the deviation from the ideal match between the peak centers of the laser focal spot and the electron beam in the actual experiment, due to e.g. the distortion from the Gaussian laser profile (section 5.2.1), the drift of electron beam and especially the vertical vibration of the laser centroid (RMS ~16 μm, section 3.2.1.5), etc., the value we used in the simulation should be closer to

the actual measurement environment. Also from the luminosity viewpoint, the vertical electron beam size should not be critical for the CBS interaction process due to the much larger vertical focal spot size of the laser, see section 1.5.

Panel (a) of Fig. 4.1 is the entire energy spectrum of the CBS photons at the CP. The photon density at the Compton edge is ~1.8 $\times 10^4$/keV. Panel (b) shows the angular distribution of the signal gamma photons with the energies near the Compton edge, the scattering angles of most of the photons are less than 0.15 mrad, therefore it is no problem for them to pass through the 130 mm long collimator.

Panel (c) and (d) show the transverse contour of the CBS photons with different energies at the collimator. Since the electron beam at ANKA has much larger horizontal beam size than the vertical one, the scattered photons around Compton edge also has the same flat shape. We can see the horizontal size of the edge photons is ~5 mm, therefore it is much critical to get the edge photons passing through the horizontal opening of the intensity absorber (~6 mm see section 3.2.3). Since the Compton edge photons have zero scattering angle, their density profile just reflects the electron beam density profile at the CP, which is set as Gaussian distribution here. For the lower energies, the scattering angle increases and further enlarges the transverse profile after propagation of ~10 m to the collimator, but most of them still remain in the range of the tungsten collimator and get absorbed. Panel (e) and (f) show the transverse distribution of the photon density, due to the vertical polarization, the vertical distribution is much sharper than the horizontal profile.

Panel (g) shows the energy spectrum with different collimator apertures, we can further zoom in to inspect the Compton edge as panel (h). The width of the Compton edge is caused by the energy spread of the electron beam. The CBS photons with energies much lower than that of the Compton edge are not useful for the measurement but further take up the limited detection live time, therefore small collimator apertures are preferable to keep such background as low as possible. However, the aperture cannot be too small, otherwise it would lead to misjudgment of the Compton edge energy due to the emittance effect [22,48].

From panel (h) we can see the 3 mm diameter aperture already covers most of the Compton edge photons, but still slightly insufficient. The 4 mm dia. aperture should be optimum, which receives all the scattered photons at the Compton edge energy. For ~1.61 MeV gamma rays near the Compton edge, the intrinsic peak efficiency of our detector should not be far from ~13% for 1.33 MeV (see section 3.2.2.3), then we can use ~10% for a safe estimation. So the signal recorded by the detector at the Compton edge should be around 10^3/keV, which is enough to bring the statistic uncertainty of judging average Compton edge energy to a few 10^{-5} (see section 2.1). However under the actual measurement conditions, we have to further include the consideration of laser power clipped off by the coupling port window (~10%) and transmission reduction by the 2 mm copper of the end flange (~10%). Also the misalignment of the intensity absorber may further take away lots of scattered photons even with a large local orbit bump to have the CBS photon beam to circumvent the absorber. Therefore, the final scattered photon density registered by the detector at Compton edge energy can only be around several hundred per keV. Details of discussion can be found in section 4.3.3.

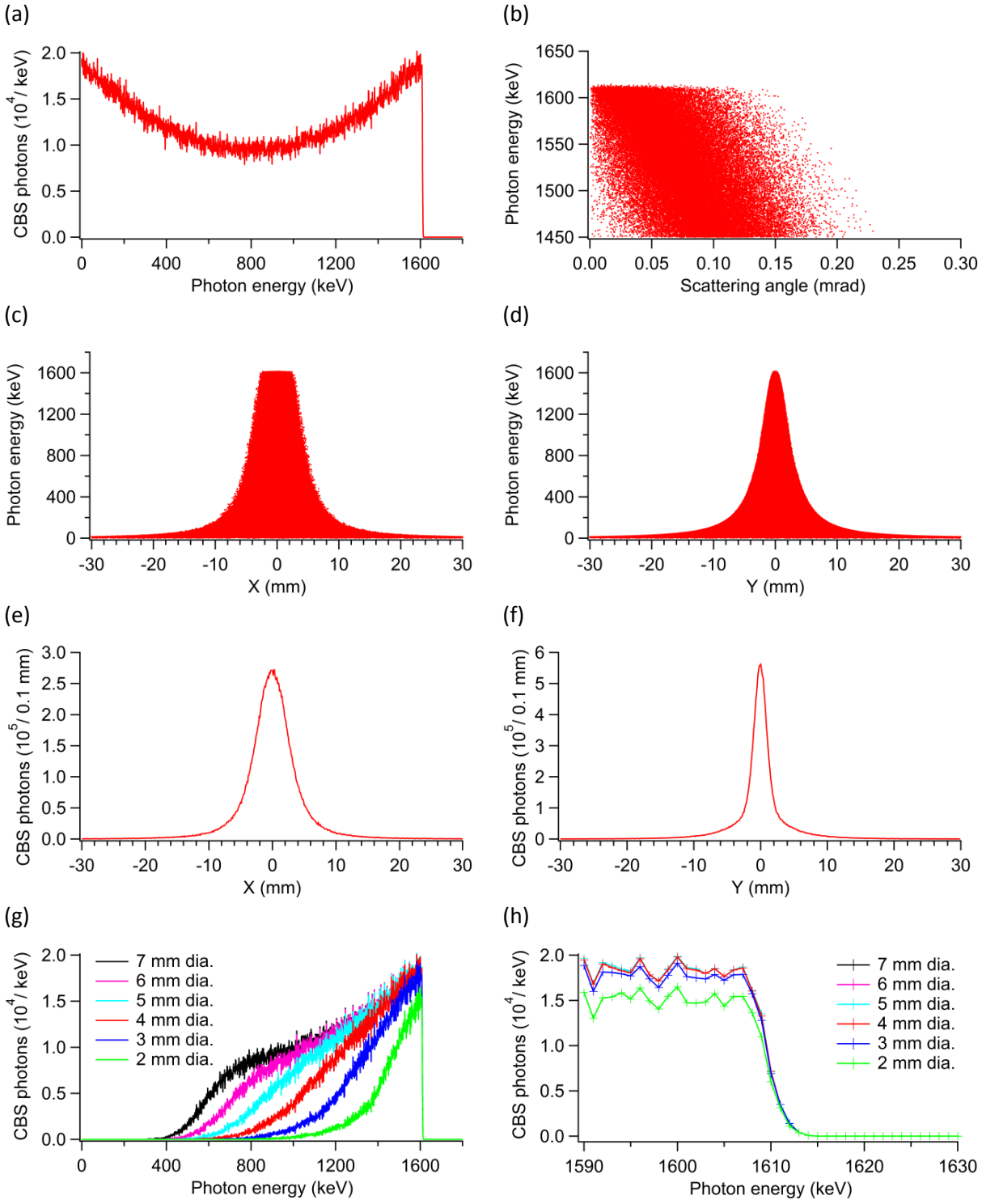

Figure 4.1: Transverse collision of vertically polarized and vertically focused CO_2 laser on 1.3 GeV electron beam at normal optics for 10 minutes. (a) Entire energy spectrum, (b) Angular distribution of photon energies, (c) (d) Transverse distribution of photon energies at the collimator, (e) (f) Transverse distribution of photon density at the collimator, (g) Energy spectra of scattered photons received by different collimator apertures, (h) Compton edge spectra received by different collimator apertures.

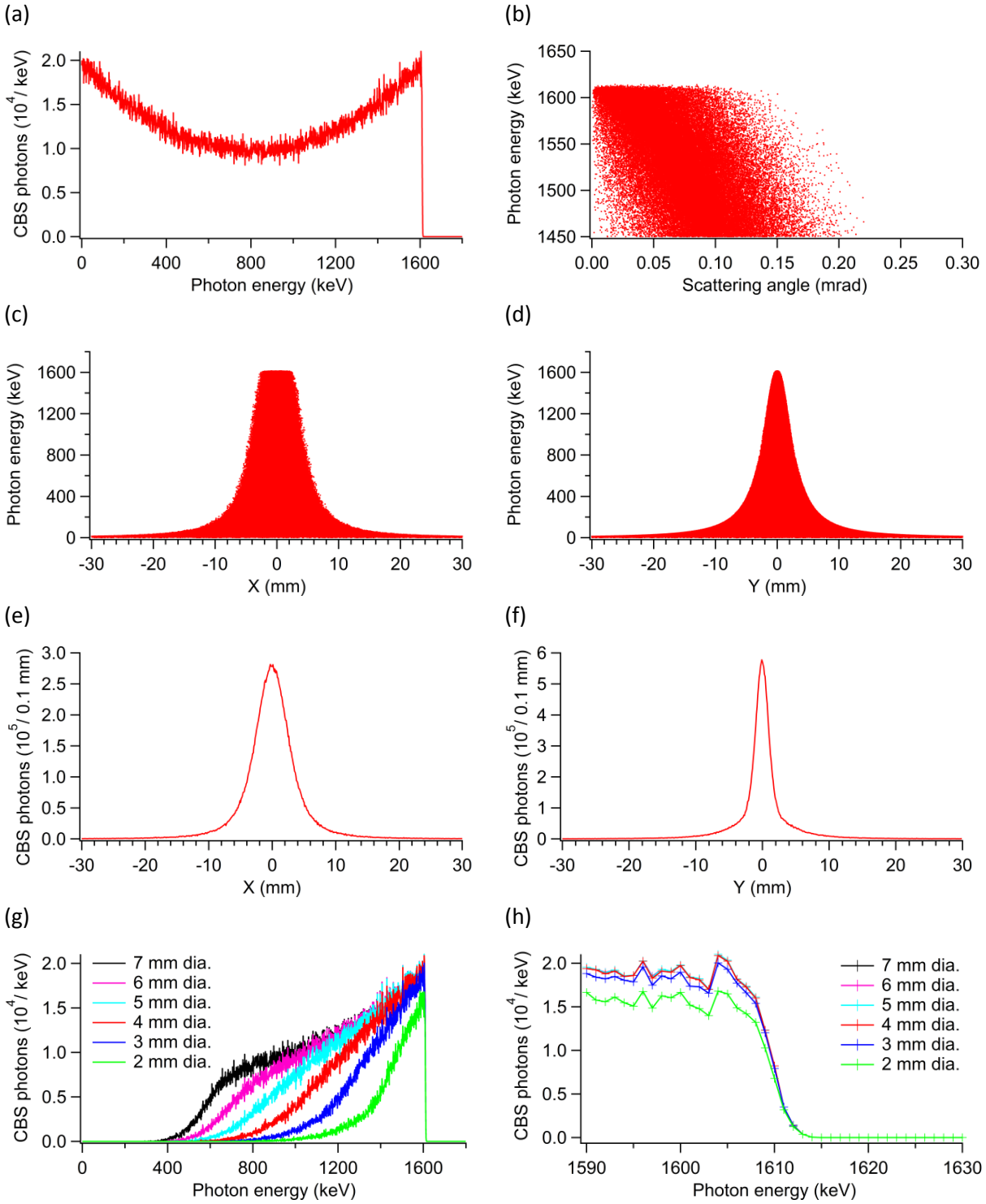

Figure 4.2: Transverse collision of vertically polarized CO_2 laser with a round focal spot on 1.3 GeV electron beam at normal optics for 10 minutes. (a) Entire energy spectrum, (b) Angular distribution of photon energies, (c) (d) Transverse distribution of photon energies at the collimator, (e) (f) Transverse distribution of photon density at the collimator, (g) Energy spectra of scattered photons received by different collimator apertures, (h) Compton edge spectra received by different collimator apertures.

We can simulate the properties of the scattered beam with same conditions except the laser has a round focal spot with the radius of 160 μm RMS. As we can see in Fig. 4.2 (a) – (h), the results are nearly the same as in Fig. 4.1, except the Compton edge shape is not that sharp due to the much larger horizontal divergence of the laser at the focal plane than the parallel beam. Thus the especially large horizontal beam size is preferable to our measurement.

4.1.2 The head-on collision for normal optics at 1.3 GeV

We can also simulate the situation of the head-on collision, assuming that the intensity absorber has been removed. Given that the long straight section is much longer than the ion pump, with the same window of 35 mm clear aperture, we can no longer focus the laser beam to ~160 μm RMS focal spot size, instead the beam RMS size can be achieved ~800 μm if the focal position is located at the middle of the long straight section, which is ~5 meter away from the coupling window. The electron beam is further assumed to remain the same size as around the middle of the long straight section (~690 μm × ~50 μm) for the optimum estimation.

From Fig. 4.3 we can get the photon density at the Compton edge is ~10^5/keV, nearly 5-6 times more than transverse setup. However, for such high energy gamma photons the detection efficiency is probably only half of that under transverse scattering since the Compton edge energy is twice as that of transverse configuration. Also, normally the scattered photons produced by head-on collision have to pass through at least the mirror used to reflect the CO_2 laser into the beam pipe, making the transmission even less [17][21]. So in total, only 2-3 times more Compton edge photons can be recorded in the spectrum under head-on collision than that via transverse configuration.

The Compton edge now is two times as broad as at transverse scattering, but the relative width is still the same, since the relative energy spread doesn't change. 3 mm dia. and 4 mm dia. aperture are still enough to receive nearly all of the signal photons on Compton edge.

Table 4.2: Parameters of the head-on collision for normal optics at 1.3 GeV.

Electron beam		Laser and Detector	
Current / mA	10	Wavelength / μm	10.23
Energy / GeV	1.3	CW laser power / W	20
Vertical size (RMS) / μm	~50	Vertical size (RMS) / μm	800
Horizontal size (RMS) / μm	690	Horizontal size (RMS) /μm	800
Bunch length(RMS) / ps	21.1	Polarization	Vertical
Energy spread (RMS)	4.76×10^{-4}	Collision angle	180°
Emittance / nm × rad	H: 27.5	Collimator's position after the CP / m	9.2
	V: ~0.3	Accumulation time / min	10

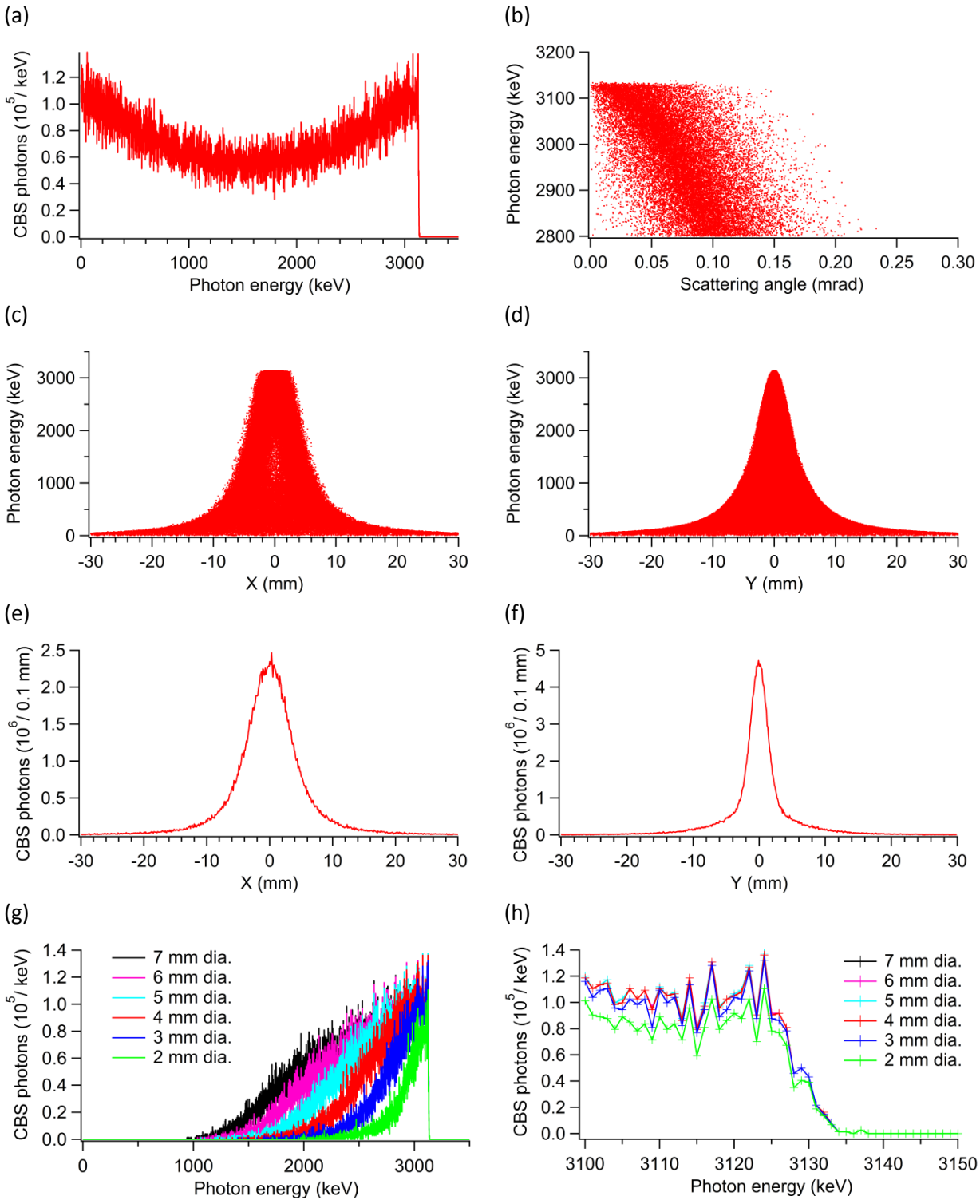

Figure 4.3: Head-on collision of vertically polarized CO_2 laser with a round focal spot on 1.3 GeV electron beam at normal optics for 10 minutes. (a) Entire energy spectrum, (b) Angular distribution of photon energies, (c) (d) Transverse distribution of photon energies at the collimator, (e) (f) Transverse distribution of photon density at the collimator, (g) Energy spectra of scattered photons received by different collimator apertures, (h) Compton edge spectra received by different collimator apertures.

4.1.3 The transvers setup for normal optics at 1.6 GeV

For 1.6 GeV, the parameter of the electron beam is shown in Table 4.3. As shown in Fig. 4.4, the photon density per keV on the Compton edge is ~1.2×10^4/keV, much lower than that at 1.3 GeV. It is because of the lower spectral differential cross section, see Eq. 1.6.

The Compton edge becomes wider, but the relative width corresponds well to the relative energy spread. Due to the horizontal beam size is larger than that of 1.3 GeV and also the electron beam divergence is bigger for 1.6 GeV at the interaction point, the 4 mm collimator aperture cannot receive all the scattered photons around Compton edge energy. Instead 5 mm is the optimum aperture, but the difference between 4 mm and 5 mm is really small. Considering the more background radiation will take up the limited detection live time, the 4 mm aperture may still be the optimum option.

Same as the 1.3 GeV head-on collision, since the Compton edge energy now is 1.5 times higher than that of 1.3 GeV, the detection efficiency should be lower accordingly. Therefore the photon density recorded on the spectrum for 1.6 GeV electron beam should be 2.7 times less than that for 1.3 GeV.

Table 4.3: Parameters of the transverse setup for normal optics at 1.6 GeV.

Electron beam		Laser and Detector	
Current / mA	10	Wavelength / μm	10.23
Energy / GeV	1.6	CW laser power / W	20
Vertical size (RMS) / μm	~60	Vertical size (RMS) / μm	160
Horizontal size (RMS) / μm	780	Horizontal size (RMS) /μm	7250
Bunch length(RMS) / ps	27.7	Polarization	Vertical
Energy spread (RMS)	5.86×10^{-4}	Collision angle	91.6°
Emittance / nm × rad	H: 38.7	Collimator's position after the CP / m	9.2
	V: ~0.4	Accumulation time / min	10

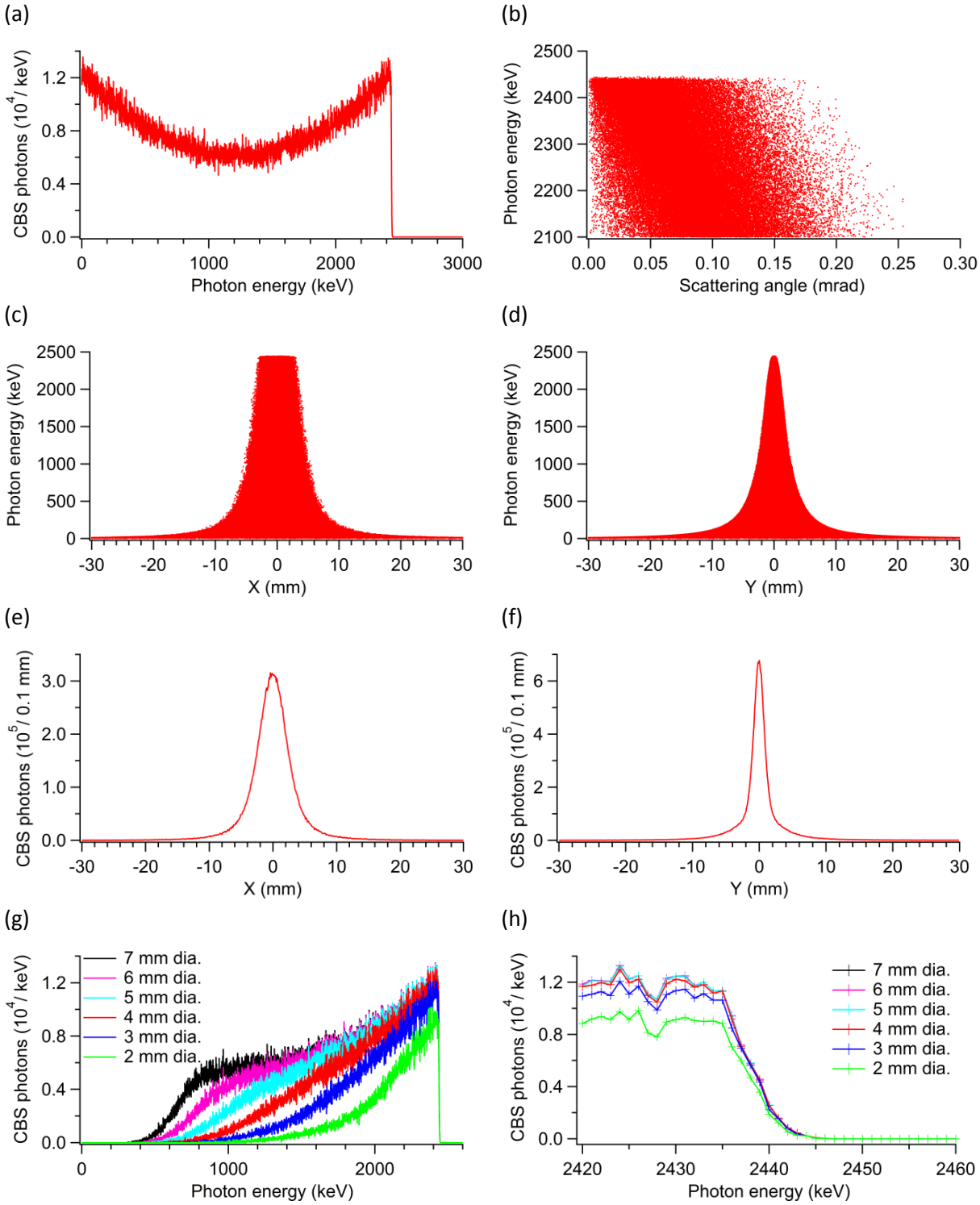

Figure 4.4: Transverse collision of vertically polarized and vertically focused CO_2 laser on 1.6 GeV beam at normal optics for 10 minutes. (a) Entire energy spectrum, (b) Angular distribution of photon energies, (c) (d) Transverse distribution of photon energies at the collimator, (e) (f) Transverse distribution of photon density at the collimator, (g) Energy spectra of scattered photons received by different collimator apertures, (h) Compton edge spectra received by different collimator apertures.

4.1.4 The transvers setup for normal optics at 2.5 GeV

For 2.5 GeV electrons, the maximum photon energy is ~6 MeV, nearly 4 times as large as that at 1.3 GeV electrons. According to Eq. 1.6, the differential cross section at the Compton edge energy is 4 times as low as that at 1.3 GeV, which gives only 5000 counts/keV in 10 minutes, see Fig. 4.5 (a). Also since now the relative energy spread of electron beam at 2.5 GeV is 1.9 times as that at 1.3 GeV, the relative width of the Compton edge is also 1.9 times as large as that at 1.3 GeV, which is shown in panel (h). The absolute width of Compton edge is ~50 keV, which is more than 7 times wider than that at 1.3 GeV.

Due to larger horizontal electron beam size and divergence at the collision point, the horizontal distribution of Compton edge photons is even wider than 1.6 GeV as shown in panel (c), resulting to bigger collimator aperture to cover all the edge photons as shown in panel (h).

Since the relative width of the Compton edge is nearly 2 times as wide as that at 1.3 GeV, and the spectral photon density at the edge is 4 times as low as that at 1.3 GeV, according to Eq. 2.6, the accumulation time should be at least 8 times longer than that at 1.3 GeV electron beam to reach the same statistical uncertainty at determination of the Compton edge energy. The assumption is taken that detection efficiency decreases linearly with the increasing photon energy. However, the actual detection efficiency may be even much smaller, thus it may require more than 10 times longer accumulation time, see section 6.1. Therefore it is much harder for measurement at higher energies than at lower energies due to smaller spectral photon density and detection efficiency, as well as larger relative width of the Compton edge.

Table 4.4: Parameters of the transverse setup for normal optics at 2.5 GeV.

Electron beam		Laser and Detector	
Current / mA	10	Wavelength / µm	10.23
Energy / GeV	2.5	CW laser power / W	20
Vertical size (RMS) / µm	~33	Vertical size (RMS) / µm	160
Horizontal size (RMS) / µm	1060	Horizontal size (RMS) /µm	~7250
Bunch length(RMS) / ps	42.6	Polarization	Vertical
Energy spread (RMS)	9.13×10^{-4}	Collision angle	91.6°
Emittance / nm × rad	H: 59.8	Collimator's position after the CP / m	9.2
	V: ~0.6	Accumulation time / min	10

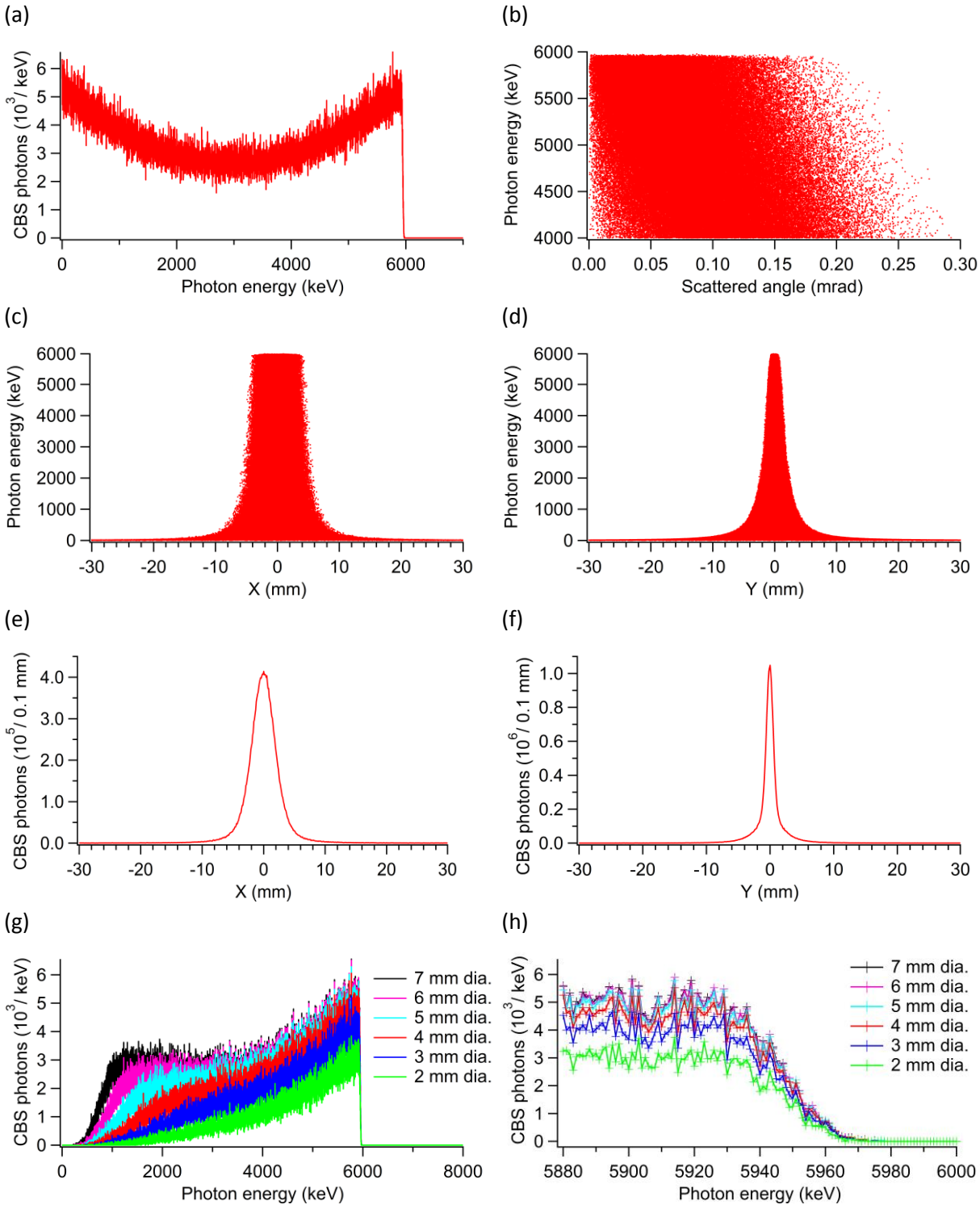

Figure 4.5: Transverse collision of vertically polarized and vertically focused CO_2 laser on 2.5 GeV electron beam at normal optics for 10 minutes. (a) Entire energy spectrum, (b) Angular distribution of photon energies, (c) (d) Transverse distribution of photon energies at the collimator, (e) (f) Transverse distribution of photon density at the collimator, (g) Energy spectra of scattered photons received by different collimator apertures, (h) Compton edge spectra received by different collimator apertures.

4.1.5 Low α_c mode at 1.3 GeV with laser of different polarization

One of the main purposes of our measurement is to determine the momentum compaction factor (α_c) at the low α_c mode. The electron beam parameters at low-α_c mode of 1.3 GeV (synchrotron frequency f_s: 8.4 kHz) can be summarized as in Table 4.5. From Fig. 4.6 (g) we can see that although the electron beam size is much larger, especially the vertical beam size is even nearly twice as big as that at normal mode at 1.3 GeV, the total photon flux and spectral photon density is only slightly less than that at the normal mode. It is the collision luminosity is insensitive to the sizes of the electron beam due to the large vertical focal size of the laser and the large Rayleigh range, see section 1.5. Our design is quite robust for accommodating all the electron beam conditions at ANKA.

Same as for 2.5 GeV, since the emittance of the low α_c mode is relatively large, therefore the horizontal divergence of the electron beam is larger than that of normal optics, given the horizontal beta functions are comparable. Therefore the scattering angle of the Compton edge photons (mainly the horizontal scattering angle), is larger than the normal optics as shown in panel (b). Also larger emittance gives lager horizontal electron beam size, which leads to larger Compton edge photon beam size. Therefore 6 mm or 7 mm dia. collimator aperture has a better reacceptance of the Compton edge photons as shown in panel (h), which is ~1.6×10^4/keV, almost the same as that at the normal optics. Thus there should be no problem for an energy measurement in the low-α_c mode.

The total production rate of the scattered photons is ~3×10^4/s. It means on average it takes 100 revolution of the electron beam to give out one scattered photon with average energy of 800 keV. The energy loss per turn due to CBS is only 8 keV, which is completely negligible compared to other sources of energy losses. Therefore the energy measurement based on CBS can be regarded as a non-intrusive method.

The transverse distributions of the gamma rays at the collimator are shown in panel (e) and (f). The photons can be shielded completely by the tungsten collimator and the lead shielding walls.

Table 4.5: Parameters for low α_c optics at 1.3 GeV with vertically polarized laser.

Electron beam		Laser and Detector	
Current / mA	10	Wavelength / µm	10.23
Energy / GeV	1.3	CW laser power / W	20
Vertical size (RMS) / µm	~100	Vertical size (RMS) / µm	160
Horizontal size (RMS) / µm	1190	Horizontal size (RMS) /µm	~7250
Bunch length(RMS) / ps	6.53	Polarization	Vertical
Energy spread (RMS)	4.76×10^{-4}	Collision angle	91.6°
Emittance / nm × rad	H: 77.6	Collimator's position after the CP / m	9.2
	V: ~0.8	Accumulation time / min	10

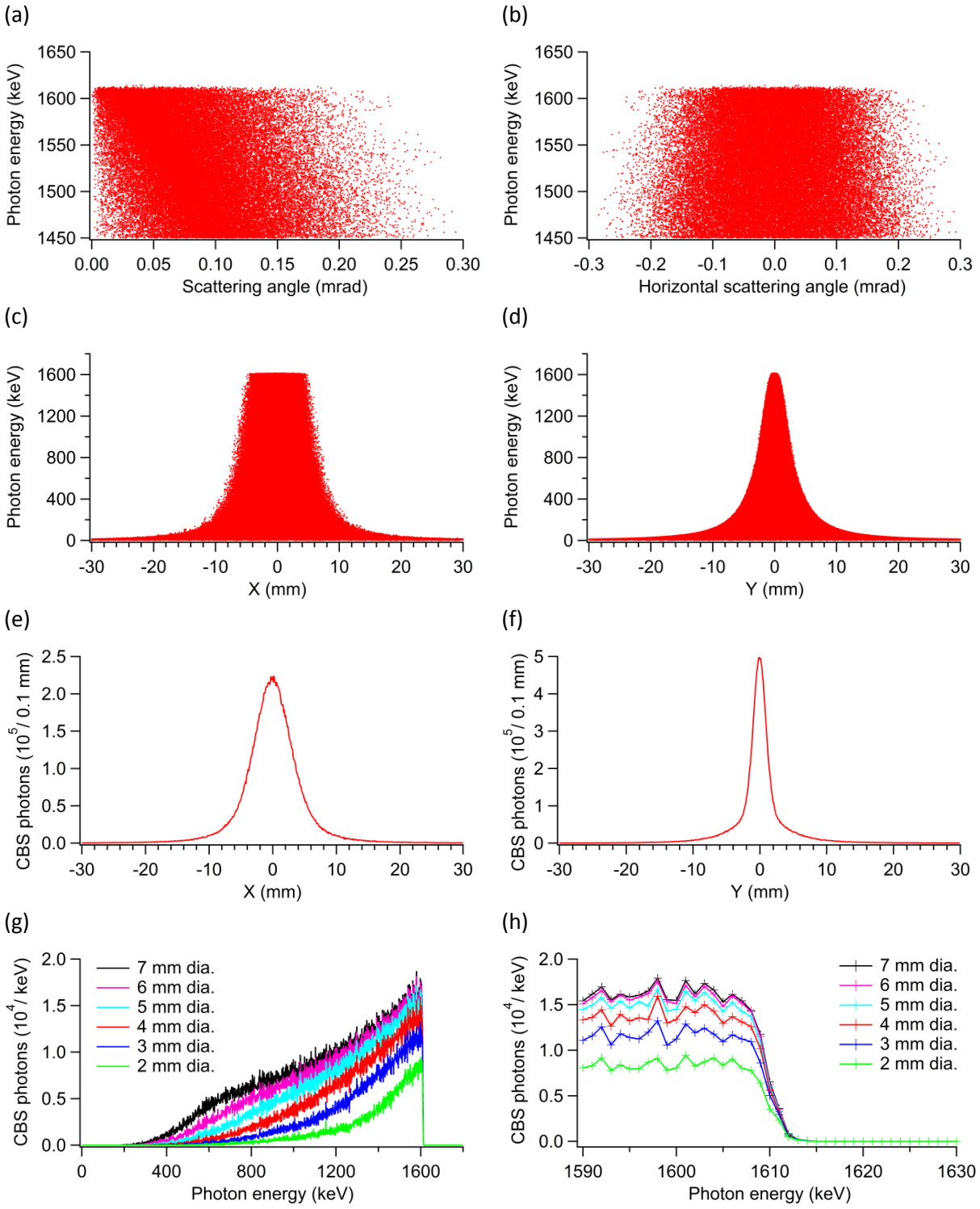

Figure 4.6: Transverse collision of vertically polarized and vertically focused CO_2 laser on 1.3 GeV electron beam at low α_c mode (f_s: 8.4 kHz V_{rf}: 150 kV) for 10 minutes. (a) Angular distribution of photon energies, (b) Horizontal angular distribution of photon energies (c) (d) Transverse distribution of photon energies at the collimator, (e) (f) Transverse distribution of photon density at the collimator, (g) Energy spectra of scattered photons received by different collimator apertures, (h) Compton edge spectra received by different collimator apertures.

If we adopted a horizontally polarized laser, the transverse distribution of the scattered photons would be much more homogeneous between horizontal plane and vertical plane as shown in Fig. 4.7 (e) and (f). It is because the horizontal scattering angle is much smaller than the vertical angle for the photons with very low energies as we can compare the transverse distributions of the scattered photon energies in Fig. 4.7 (c) and (d) to those under vertically polarized laser in Fig. 4.6 (c) and (d).

However, for the scattered photons near the Compton edge energy, the situation doesn't improve much, since the main reason for their angular shifts from exact zero scattering angle is the divergence of the electron beam. This is can be seen by comparison between Fig. 4.7 (a) and (b) and Fig. 4.6 (a) and (b). Both the total scattering angle and the horizontal scattering angles for high energy photons remain unchanged, as a result we still need 6 mm dia. or 7 mm dia. aperture to receive all the Compton edge photons as shown in Fig. 4.7 (h). However since now a lot of low energy scattered photons can propagate with small horizontal scattering angles therefore the low energy part of the energy spectra in Fig. 4.7 (g) increases, which is disadvantageous for the detection.

Table 4.6: Parameters for low α_c optics at 1.3 GeV with horizontally polarized laser.

Electron beam		**Laser and Detector**	
Current / mA	10	Wavelength / µm	10.23
Energy / GeV	1.3	CW laser power / W	20
Vertical size (RMS) / µm	~100	Vertical size (RMS) / µm	160
Horizontal size (RMS) / µm	1190	Horizontal size (RMS) /µm	~7250
Bunch length(RMS) / ps	6.53	Polarization	Horizontal
Energy spread (RMS)	4.76×10^{-4}	Collision angle	91.6°
Emittance / nm × rad	H: 77.6	Collimator's position after the CP / m	9.2
	V: ~0.8	Accumulation time / min	10

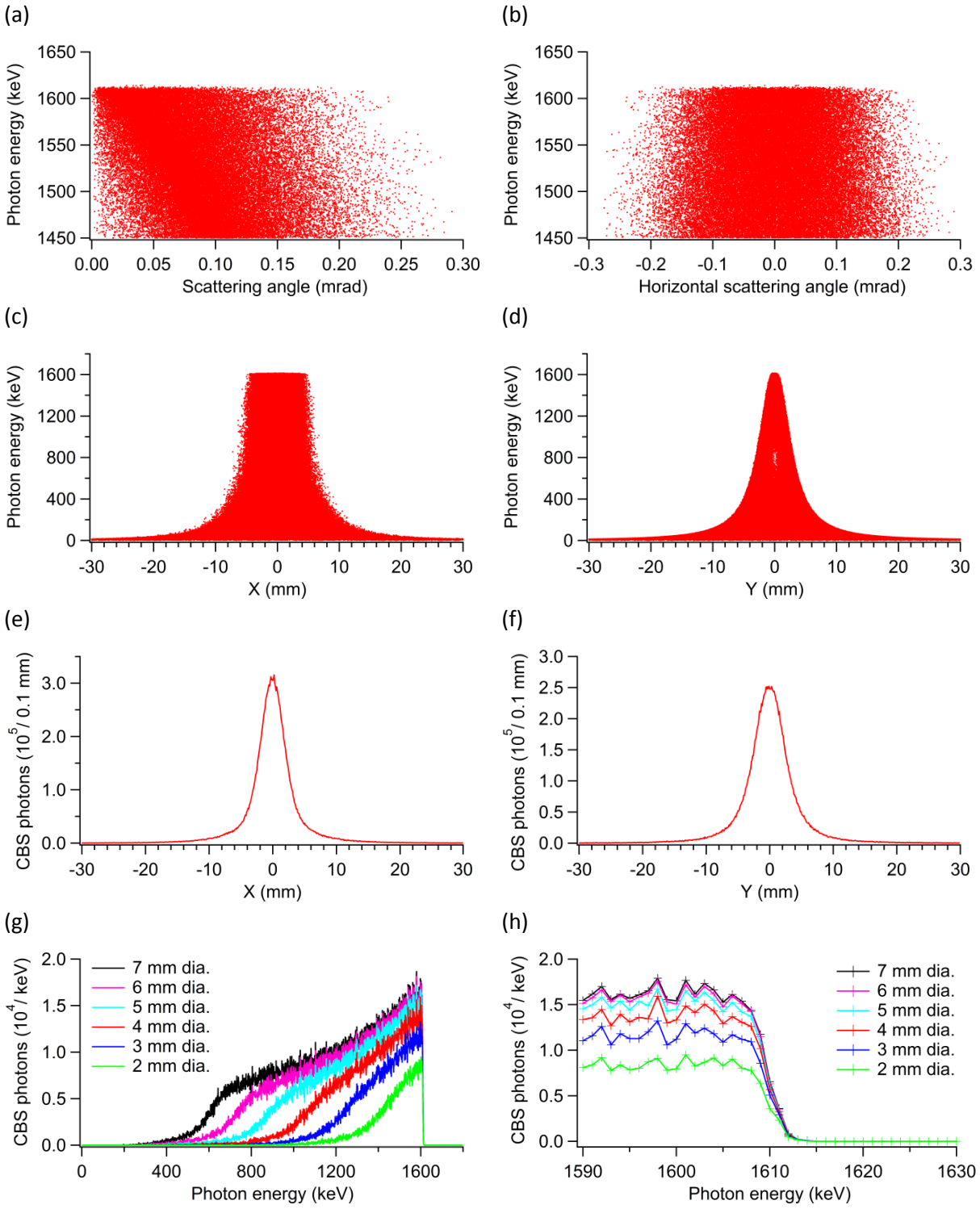

Figure 4.7: Transverse collision of horizontally polarized and vertically focused CO_2 laser on 1.3 GeV electron beam at low α_c mode (f_s: 8.4 kHz V_{rf}: 150 kV) for 10 minutes. (a) Angular distribution of photon energies, (b) Horizontal angular distribution of photon energies (c) (d) Transverse distribution of photon energies at the collimator, (e) (f) Transverse distribution of photon density at the collimator, (g) Energy spectra of scattered photons received by different collimator apertures, (h) Compton edge spectra received by different collimator apertures.

Circular polarized laser just gives results in between the situations with horizontally and vertically polarized laser as can be expected.

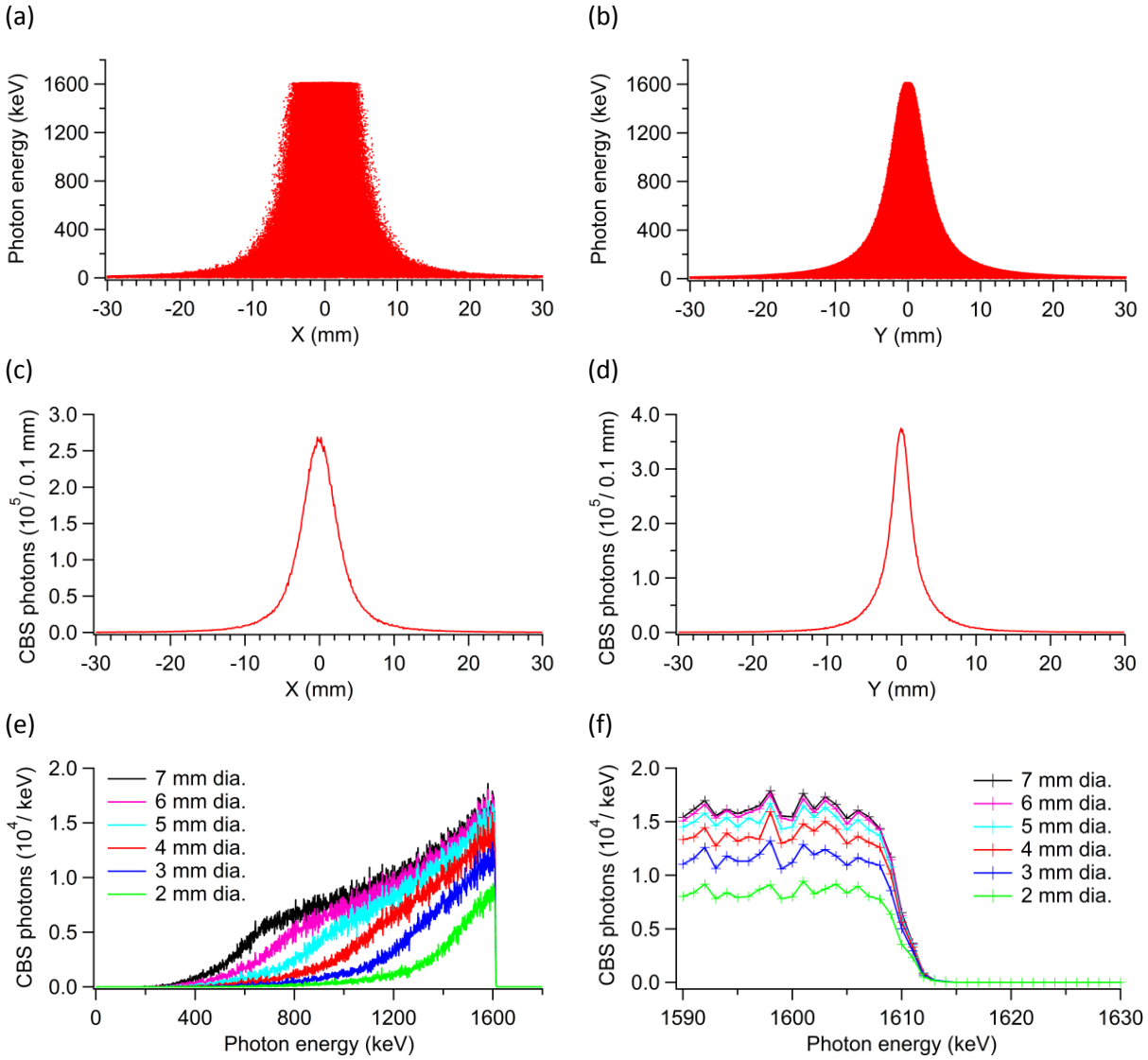

Figure 4.8: Transverse collision of circularly polarized and vertically focused CO_2 laser on 1.3 GeV electron beam at α_c mode (f_s: 8.4 kHz V_{rf}: 150 kV) for 10 minutes. (a) (b) Transverse distribution of photon energies at the collimator, (c) (d) Transverse distribution of photon density at the collimator, (e) Energy spectra of scattered photons received by different collimator apertures, (f) Compton edge spectra received by different collimator apertures.

4.2 Studies on effects from misalignment of the collimator

In Fig. 4.9, we can see that under conditions summarized in Table 4.1, if the 4 mm aperture of the collimator is horizontally misaligned by 0 – 3.5 mm, the photon count rate at the Compton edge can be much reduced, and the average photon energy moves towards the lower side of the spectrum.

Fig. 4.10 further zoom in to show the Compton edge area and edge fitting curve based on the model according to [18][22]. The edge parameters given by the fitting are summarized in Table 4.7. The width parameter stands for the standard deviation of the edge width and the parameter of the edge slope is obtained by the edge height divided by the width, which indicates the steepness of the edge. We can see that the edge width is ~1.5 keV which conforms well to the theoretical expectation based on Eq. 2.8. The simulation doesn't include the energy resolution of the detector. Therefore the energy spread of the electron beam now dominates the spread of the Compton edge.

The edge energy doesn't change much until the misalignment reaches the half size of the aperture (2 mm), afterwards the misjudgment of the fitting energy would reach the relative uncertainty of 10^{-4}, therefore undermine the precision of the measurement. Also after reaching the 2mm offset, the edge width begin to fluctuate. The edge slope decreases all the way down as the edge height continues to decrease.

The misalignment studies will show guidance for the setup optimization in Chapter 5.

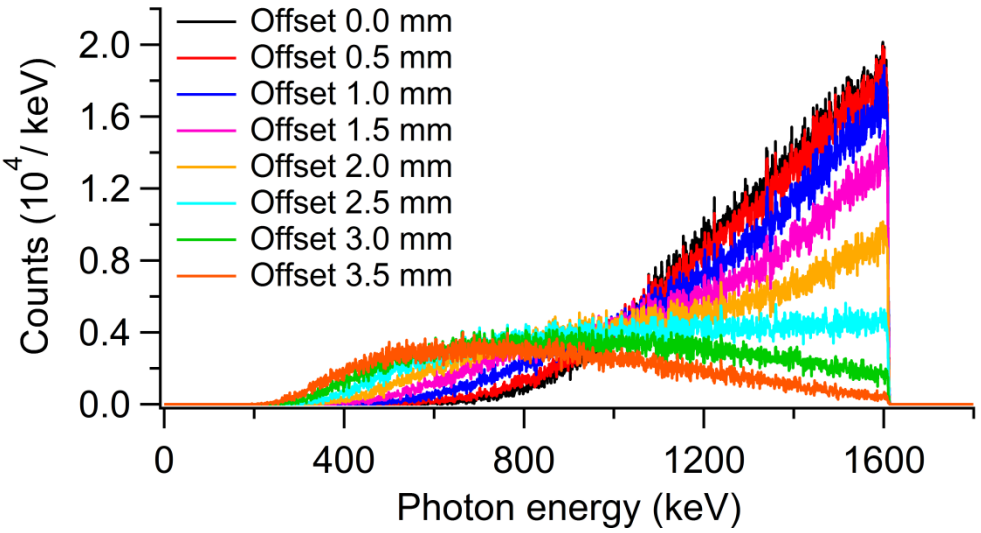

Figure 4.9: Simulated energy spectrum of the CBS photons passing through the horizontally misaligned 4 mm diameter collimator aperture. Parameters of the laser and electron beam are the same as those in Table. 4.1. The different offset is marked by different colors.

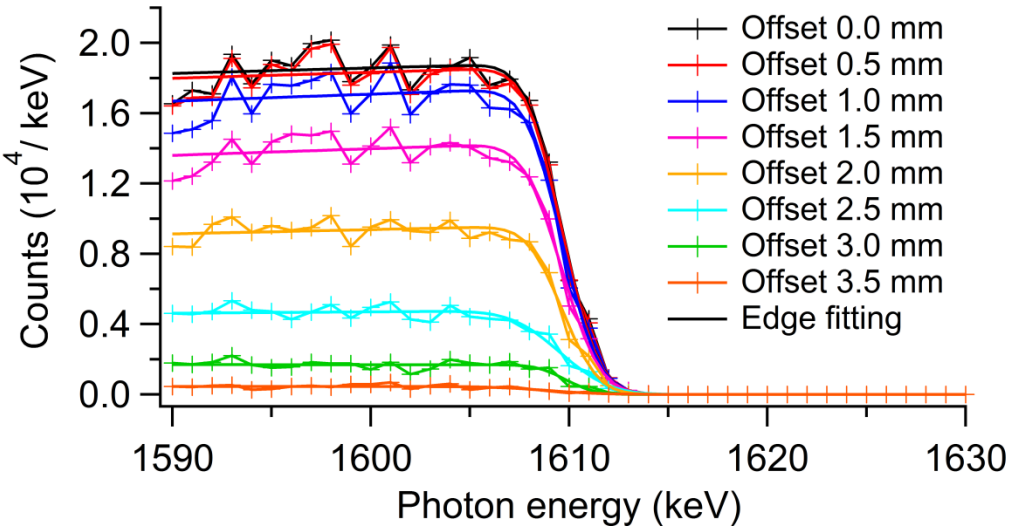

Figure 4.10: Compton edge and edge fitting of Fig. 4.9 with horizontally misaligned 4 mm diameter collimator aperture. Parameters of the laser and electron beam are the same as those in Table. 4.1. The different offset is marked by different colors.

Table 4.7: The edge parameters given by the curve fitting.

Offset (mm)	0	0.5	1	1.5	2	2.5	3	3.5
Edge energy (keV)	1609.66	1609.65	1609.64	1609.63	1609.66	1609.56	1609.82	1608.94
Edge width (keV)	1.46413	1.4602	1.46980	1.53247	1.41167	1.96141	1.16523	2.15796
Edge height (counts/keV)	18874.2	18650.6	17470.1	14343.8	9609.46	4778.97	1684.71	446.465
Edge slope (counts/keV^2)	12891.1	12772.6	11886.0	9359.92	6807.16	2436.50	1445.82	206.892

4.3 Background measurement and signal-to-noise ratio study

Since one major challenge of the transverse CBS method is the much lower interaction time in contrast to the head-on collision scheme. Therefore a further feasibility study has been carried out by comparison between a simulation of CBS photons and an actual bremsstrahlung background measurement with a 30% relative efficiency HPGe spectrometer.

4.3.1 Background measurement

When the electron beam scatters with residual gas in the beam pipe, the gas bremsstrahlung is generated and its energy can extend up to the electron beam energy, which composes significant background for our measurement. Same as Compton backscattered photons, it is also highly collimated, predominantly propagating in a forward narrow cone with half angle of ~1/γ. An analytical model has been proposed by [78], but in order to precisely study the spectral characteristics, especially the photon count rate near the Compton edge, we performed a

bremsstrahlung measurement at low-α_c mode of 1.3 GeV at ANKA. The background was measured at the long straight section of the IMAGE beamline, see Fig. 4.11. The HPGe detector was a Canberra GX3018, with an energy resolution of 1.80 keV (FWHM) at 1.33 MeV and an active volume of 139 cm3 (diameter 58 mm, length 52.5 mm). The full energy peak efficiency for ~1.6 MeV photons is estimated to be ~8.5%.

Figure 4.11: Background measurement at IMAGE beamline.

According to the equation proposed in [78], the bremsstrahlung flux has a linear dependence on the beam current, thus we can normalize the scattered photon count rate with respect to the electron current. Also since besides beam current, only the electron beam energy, the pressure in the beam pipe and the geometrical factor can influence bremsstrahlung generation, so in principle it has nothing to do with the operation modes and energies.

The measurements with different slits area have been carried out for high current at multi-bunch mode and low current at single bunch mode respectively as shown in Fig. 4.12 and Fig. 4.13. Since the low current measurement needs to accumulate a long time for a statistically reliable result, the spectra of the environmental radiation (natural radiation elements, cosmic radiation, etc.) has been taken separately and removed from the bremsstrahlung spectra.

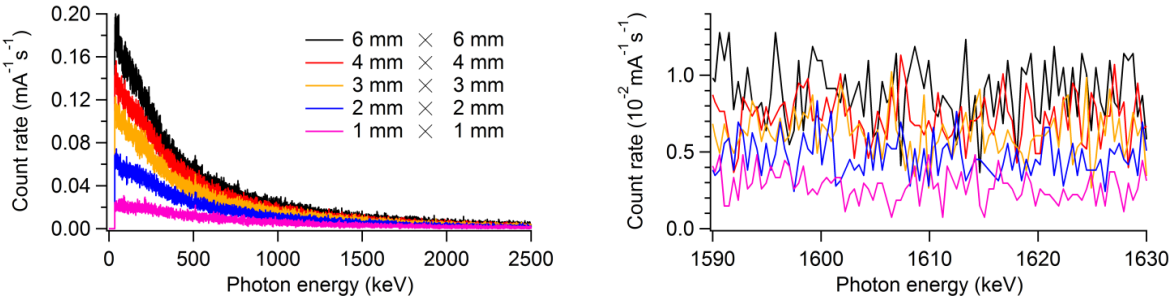

Figure 4.12: Bremsstrahlung background acquired for 60 seconds live time at low-α_c mode of 1.3 GeV under high electron beam current (~40-50 mA, multi-bunch mode) with 36 mm^2, 16 mm^2, 9 mm^2, 4 mm^2 and 1 mm^2 slits. The photon count rate has been normalized according to the respective beam current. Bin size of every channel is 0.4283 keV. The graph on the right side is the zoom in of the Compton edge area.

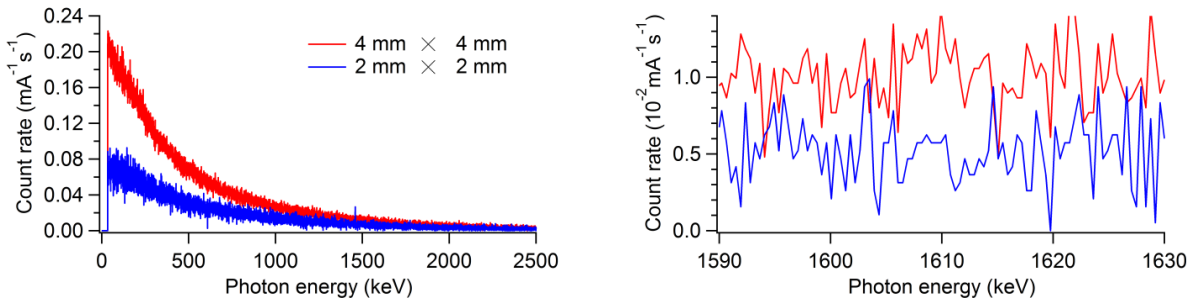

Figure 4.13: Bremsstrahlung background acquired for 2000 seconds live time at low-α_c mode of 1.3 GeV under low electron beam current (~1-2 mA, single bunch mode) with 16 mm^2 and 4 mm^2 slits. The photon count rate has been normalized according to the respective beam current. Bin size of every channel is 0.4283 keV. The graph on the right side is the zoom in of the Compton edge area.

4.3.2 Simulation of the Compton edge photons

Since the beamline slits in the background measurement has the same location as our collimator, we can adopt the same conditions as those used in section 4.1.5 for the simulation of the Compton edge photons. The only exception is the aperture areas and shapes. The simulated Compton edge spectra for respective aperture areas can be seen in Fig. 4.14. The HPGe full energy peak efficiency of 8.5% is assumed and included in the result. The photon counts have been normalized according to the electron beam current and detection accumulation time.

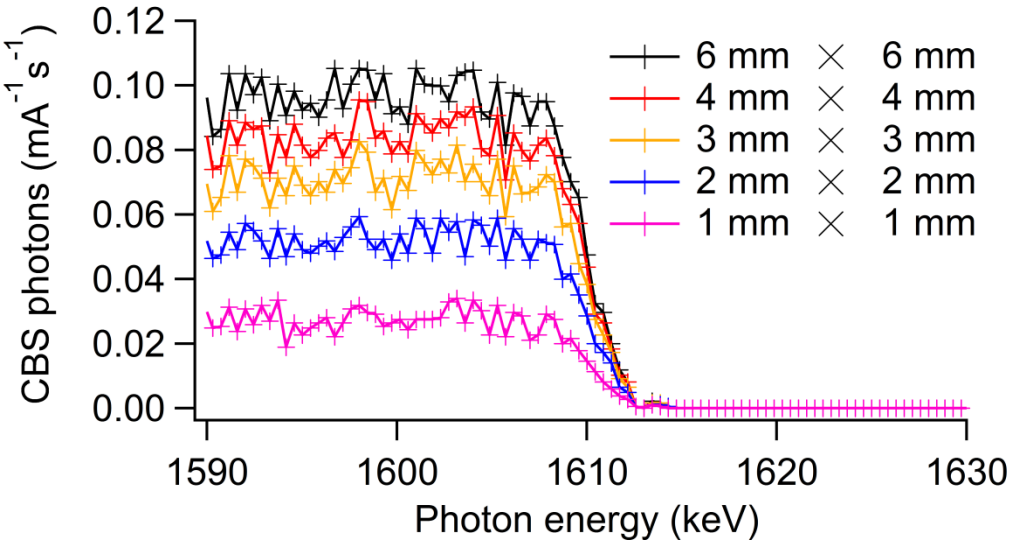

Figure 4.14: Simulated CBS photon spectra near the Compton edge for the same condition as in Table 4.5 but with square shaped collimator apertures. The photon count has been normalized according to the electron beam current and accumulation time. Bin size of every channel is 0.4283 keV. 8.5% full energy peak efficiency is included.

4.3.3 Signal-to-noise ratio

We can select the plateau of Compton edge as from 1590 keV to 1606 keV, the signal-to-noise ratio can then be obtained based on the comparison between the simulation in section 4.3.2 and actual background measurement in section 4.3.1, as summarized in Table 4.8 and 4.9.

Table 4.8: Average photon count rate at low electron current (photons/mA/s).

Slits/collimator area	16 mm^2	4 mm^2
Background (measured)	0.3609	0.2026
Signal (simulated, ~8.5% detection efficiency)	3.282	2.038

Table 4.9 : Average photon count rate at high electron current (photons/mA/s).

Slits/collimator area	36 mm^2	16 mm^2	9 mm^2	4 mm^2	1 mm^2
Background (measured)	0.3356	0.2713	0.2383	0.1802	0.1100
Signal (simulated, ~8.5% detection efficiency)	3.774	3.282	2.778	2.038	1.075

We can see that the bremsstrahlung background values under low current are slightly higher than those under high electron beam current. Since the beam current of our measurement is much closer to the low current situations, the background measurement at single bunch mode is better suited. Therefore our measurement conditions with S/N of ~9 can be expected. However, under actual experiment conditions,

(1) Losses on the optical components: the finite aperture of optical components, especially the clear aperture of the ZnSe viewport is only ~35 mm, will cut off the Gaussian laser beam on the edge. It cost ~10% laser power including the reflection and absorption losses of optical components.
(2) End copper disk: the end copper disk of 2 mm thickness mounted at the end of the long straight section will cost 10% loss of the Compton edge photons generated by 1.3 GeV electron beam.
(3) Throughput of detection: not all the photon being detected can be register in the memory of the detector at very high input count rate. At worst case only 50-60% signals can be registered on the spectrum due to the pile up effect. This can be improved by reducing the electron beam current or signal shaping time of detector setting.
(4) Intensity absorber: The intensity absorber stand at the middle between the collision point and the collimator. It is horizontally misaligned by ~3 mm and has only 6mm horizontal opening. The Compton edge photon beam has similar size. Even though a very large local bump can be applied to let the edge photons passing through the opening, there may still be ~10-20% signals hitting on the absorber.

Totally, it is possible that only ~70-80% of the signals in the ideal simulation can be expected in the actual measurements. The amount of signal photons enables us to determine the Compton edge energy with statistical uncertainty down to 10^{-4} for only 2-3 minutes according to Eq. 2.6, which is intrinsically valuable for low alpha mode measurement.

Although the bremsstrahlung radiation would also largely hit on the absorber, but their energy enable them to penetrate through the thinner edge of the absorber copper block. Whether secondary photons can be generated by the scattering of the bremsstrahlung radiation on the copper block and their propagation direction should be further studied.

5. Measurement method and optimization of the transverse CBS setup at ANKA

After the introduction of the setup design in Chapter 3 and the simulation results in Chapter 4, the measurement procedure of the innovative setup will be established in this chapter. Also, the optimization of the setup will be presented.

5.1 Method of the energy measurement based on the transverse CBS setup

Figure 5.1 (b) shows a typical CBS spectrum with a distinct Compton edge compared to the radiation background as Fig. 5.1 (a). The signal-to-noise ratio is approximately 4. With this as an example I will show in the following how to obtain the precise electron beam energy values.

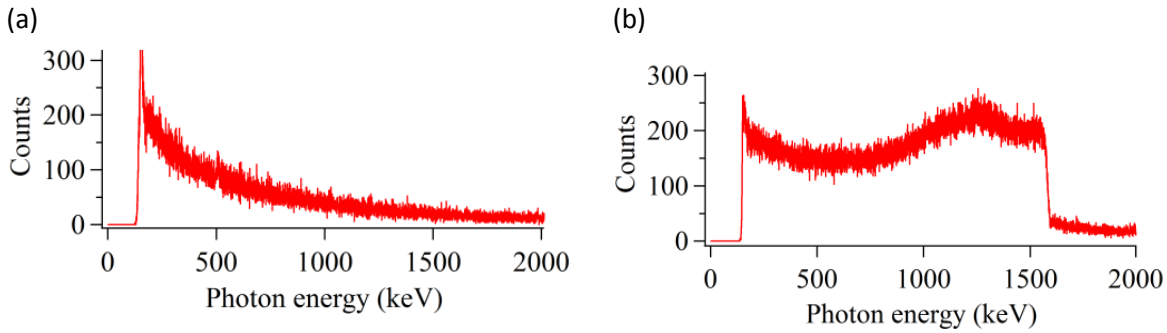

Figure 5.1: Gamma ray spectrum at 1.3 GeV for 120 seconds: (a) radiation background (laser off, e^- beam ~10.7 mA); (b) CBS signal and radiation background (laser on, e^- beam ~9.3 mA).

5.1.1 Precise determination of the laser propagation direction

In contrast to the traditional head-on collision, the transverse setup requires a very accurate knowledge of the collision angle, see section 2.2. We use the mechanical centers of two quadrupoles as a Reference Line (RL) as shown in Fig. 5.2, then the laser direction can be measured relative to the RL with a laser tracker (Leica Absolute Tracker AT401) and a camera (Spiricon Pyrocam IV). We also use Beam Position Monitors (BPMs) to monitor the electron orbit orientation relative to the RL. The collision angle φ can then be determined.

The main part of φ is between the RL and the vector set by the two camera positions. It is measured as 91.648° with the laser tracker. After consideration of the drift of the beam centroid shown in Table 5.1, the laser direction was determined to be 91.630° relative to the RL. Since the laser tracker is very accurate (maximum permissible error: ±15 µm + 6 µm/m) compared to the beam centroid stability (σ_X in Table 5.1), its measurement uncertainty is negligible. If we assume the worst case that σ_X is solely caused by angular drift rather than parallel beam movement, the angular uncertainty of the laser direction can then be determined as 0.23 mrad = 0.013°. So the laser beam is 91.630 ° ± 0.013° relative to the RL.

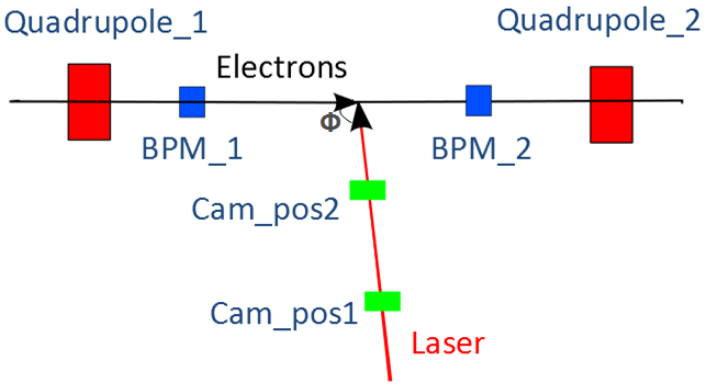

Figure 5.2: Determination of collision angle. Quadrupole_1 and 2 are MQ1_S3_02 and MQ1_S4_01. BPM_1 and 2 are DBPM_S3.09 and DBPM_S3.10. Camera position 1 and 2 are Marked in Fig. 3.8.

Table 5.1: Centroid Measurement.

	pos1	pos2
X center of 10000 samples (μm)	13877	14259
σ_X (μm)	199	194
Distance between pos. 1 and 2 (m)	1.2010	

The BPM_1 and 2 are calibrated to Quadrupole_1 and 2 respectively via Beam Based Alignment (BBA), which guarantees their zero scales are aligned to the centers of the quadrupoles, therefore the readings of the electron beam orbits have the same reference as the laser beam. From estimation based on the BPM system at ANKA, the uncertainty of the calibration of BPM based on beam based alignment should be much less than the order of 0.1 mrad/0.006°. Besides the BPM calibration, the other possible uncertainties are mainly mismatch between the magnetic and mechanical centers of the quadrupoles, which is < 0.05 mrad and electron orbit drift during measurement, which is < 0.01 mrad, based on the measurement results. All of them are negligible compared to the uncertainty contour we use for the laser drift during measurement.

According to the readings from BPM_1 and BPM_2, the electron beam orientation relative to the RL is -0.17 mrad = -0.010°. Then the collision angle φ is 91.620° ± 0.013°, which gives $\sigma_\phi/2\tan(\phi/2)$ = 1.1 × 10^{-4} in Eq. 2.5.

The laser propagation direction remains stable once the optics are set up and fixed. The electron beam orbit is very close to the RL and also stays relatively stable when the automatic orbit correction is turned on. Therefore the collision angle needs to be calculated only once for one fill, then the energy can be continuously measured and monitored. But in our case special care should be taken to calculate the collision angle every time, since a very big local orbit bump has to be applied to circumvent the misaligned absorber (see section 3.2.3), and the strength of the magnetic bump cannot be memorized by the control system therefore can hardly be repeated manually.

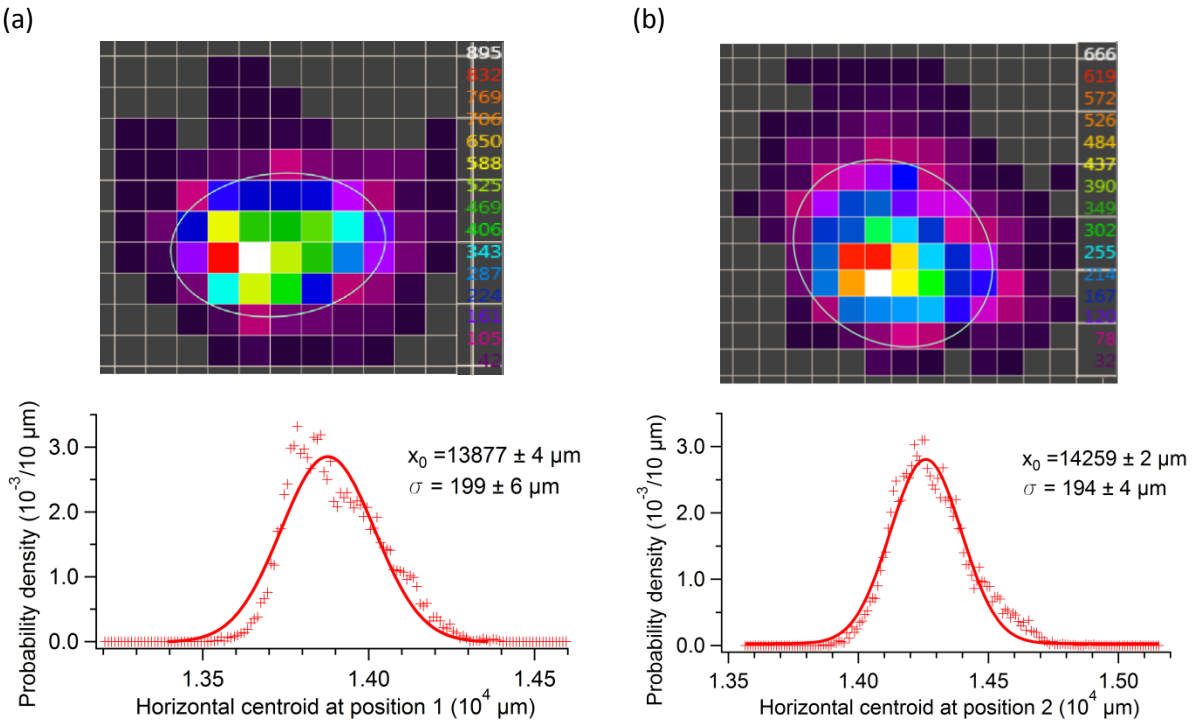

Figure 5.3: Long term monitor of horizontal laser beam centroid with the tracking image from the camera and the Gaussian distribution fitting. (a) at position 1 (Gaussian distribution fitting: average position is 13877 ± 4 μm, one standard deviation is 199 ± 6 μm); (b) at position 2 (Gaussian distribution fitting: average position is 14259 ± 2 μm, one standard deviation is 194 ± 4 μm).

5.1.2 Preparation and calibration of HPGe

The highest channel (No. 16383) of the MCA (see section 3.2.2.4) has been set to ~6300 keV (0.382 keV/channel) to accommodate the highest possible Compton edge energy at 2.5 GeV (~5.8 MeV). Since our dewar is only 7 liters, it needs to be refilled every 5 days. If sometimes the shifts schedule of the storage ring does not allow such refilling pattern, the detector has to warm up and cool down again, then it has to be recalibrated based on the same calibration procedure. It is efficient for our proof of principle experiment, but for a proper instrument, further continuous refilling mechanism like a pressure fill bayonet and a transfer line should be considered if the detection system remains inside the concrete wall.

It is not trivial to calibrate the HPGe with the relative uncertainty down to less than 10^{-4} as needed in the measurement. The calibration of the HPGe at ANKA has been tested only based on detection of the natural radiation elements. It further spares the efforts to obtain the man-made gamma radiation sources with all the related operation permission. In order to increase the incident photon rate, the HPGe is taken out of the lead blocks every time for calibration. The radiation lines we select as calibration references have good count amounts (normally, net peak area more than 10000 counts) and good peak shapes on the spectrum. They are best to spread equally over the whole energy range. Including more radiation lines does not necessarily improve the calibration uncertainty.

The highest radiation line in the natural environment is 2614.51 keV of Tl-208. Thus due to the possible nonlinearity of the MCA channel-energy relationship, high energy radiation source (e.g. 244Cm/13C [21] or 238Pu/13C [17]) is better to be adopted, especially for ~6 MeV Compton edge energy for 2.5 GeV electron beam. But studies have shown that the calibration error for linear fit due to lack of such high energy source can still remain below 10^{-4} at the energy region below ~6 MeV [17]. Therefore for our transverse setup the uncertainties due to laser beam drift and edge curve fitting still dominate the total measurement uncertainty.

For the energy range below 3 MeV, the linear fit is sufficient and the relative uncertainty of calibration reaches only 1.8×10^{-5} (the relative uncertainty of the linear term), as shown in Fig 5.5. It is already negligible compared to the uncertainty estimation of collision angle discussed in section 5.1.1. Therefore, to our aim of energy measurement to achieve relative uncertainty of 10^{-4}, the natural radiation background is enough to calibrate the HPGe. Introducing more man-made radiation sources with higher radiation intensity will speed up the calibration procedure and may have the potential to further reduce the calibration uncertainty, e.g. according to [22], using the radiation source of Ra-226 and Co-60 together with K-40, the calibration uncertainty achieves 2.5×10^{-5} in 20 minutes by linear fit.

There is another calibration example shown in Fig. 5.6 and Fig. 5.7 (accumulation time around 100 hours). We can see the relative uncertainty of the linear term (3.1×10^{-5}) is a little worse compared to that of 60 hours accumulation in Fig 5.5. The reason is probably the longer accumulation time may also include more noise counts. Less than ~60 hours accumulation may not be sufficient for good statistic count of some low count rate radiation lines such as 2204.21 keV line of Bi-214 (less than 10000 counts for the net peak area), therefore undermining the calibration uncertainty. For example, about 40 hours measurement gives 4.1×10^{-5} relative uncertainty of the linear term, while around 17 hours accumulation shows only 7.3×10^{-5} for the calibration uncertainty from the linear fit.

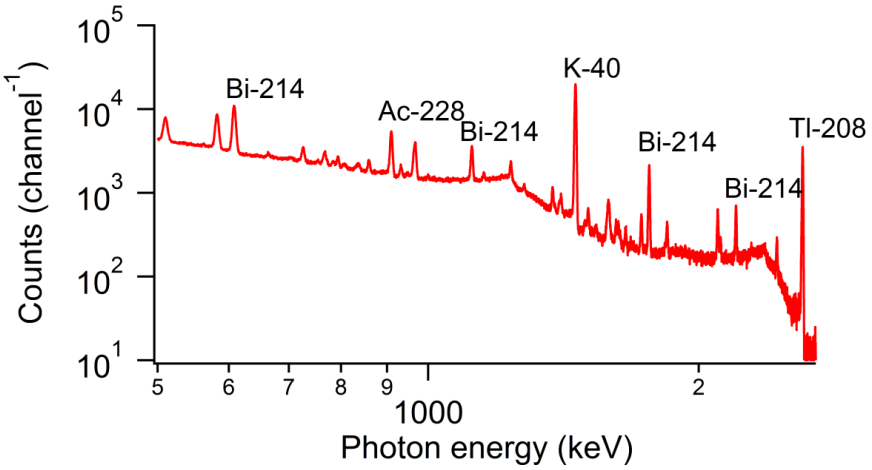

Figure 5.4: Natural radiation lines used to calibrate the HPGe. Accumulation time is about 60 hours.

Table 5.2: HPGe calibration measurement for around60 hours.

Channel	**Energy (keV) [79]**	**Nuclides**
1589.58	609.312 ± 0.007	Bi-214
2378.40	911.196 ± 0.006	Ac-228
2924.63	1120.29 ± 0.01	Bi-214
3814.40	1460.822 ± 0.006	K-40
4607.74	1764.49 ± 0.01	Bi-214
5756.45	2204.21 ± 0.04	Bi-214
6828.90	2614.51 ± 0.01	Tl-208

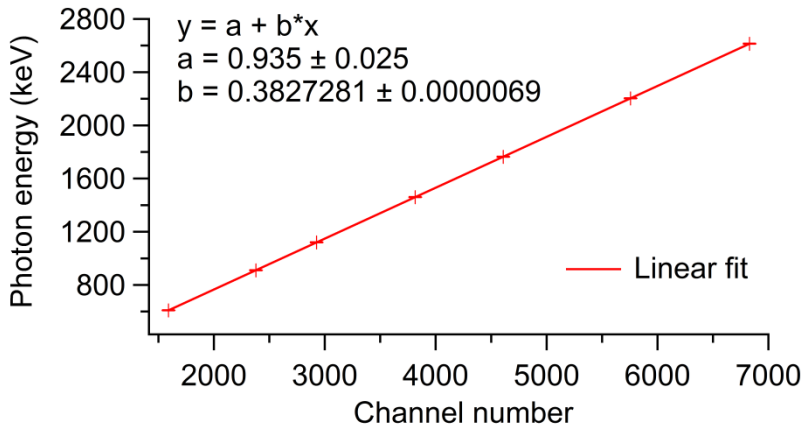

Figure 5.5: The calibration curve of the natural background radiation lines listed in Table 5.2. The linear fit gives energy-channel coefficients and the corresponding uncertainty. (χ^2/ndf = 5.011/5)

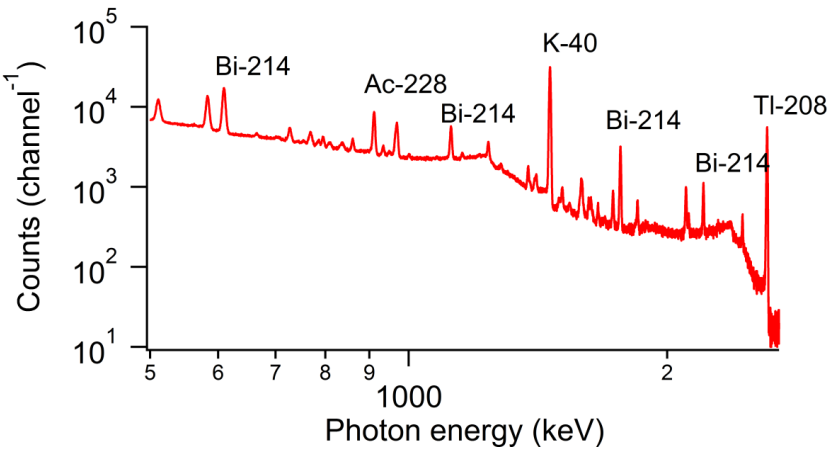

Figure 5.6: Natural radiation lines used to calibrate the HPGe. Accumulation time is about 100 hours.

Table 5.3: HPGe calibration measurement for around100 hours.

Channel	**Energy (keV) [79]**	**Nuclides**
1589.85	609.312 ± 0.007	Bi-214
2378.76	911.196 ± 0.006	Ac-228
2924.86	1120.29 ± 0.01	Bi-214
3815.04	1460.822 ± 0.006	K-40
4608.59	1764.49 ± 0.01	Bi-214
5757.32	2204.21 ± 0.04	Bi-214
6830.07	2614.51 ± 0.01	Tl-208

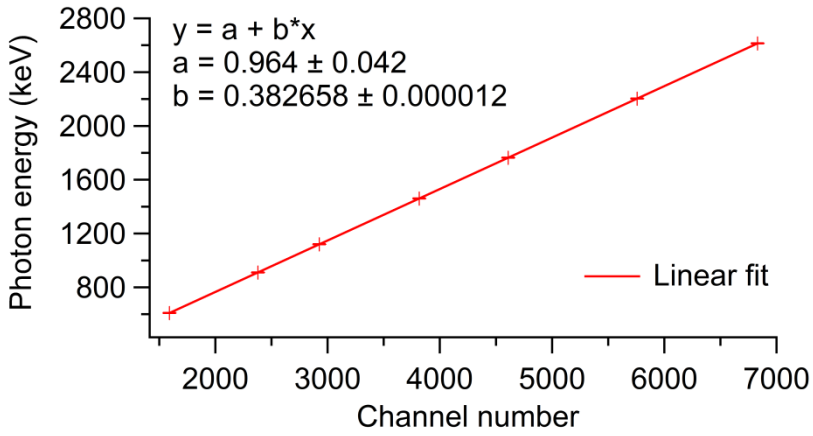

Figure 5.7: The calibration curve of the natural background radiation lines listed in Table 5.3. The linear fit gives energy-channel coefficients and the corresponding uncertainty. (χ^2/ndf = 5.001/5)

5.1.3 Curve fitting to determine average energy of Compton edge

According to [17,18,21], the Compton edge curve can be fitted by a six-parameter function to determine the average value of the Compton edge energy:

$$f(x) = \frac{1}{2}[p_2(x-p_0)+p_3] * erfc\left(\frac{x-p_0}{\sqrt{2}p_1}\right) - \frac{p_1 p_2}{\sqrt{2\pi}} \exp\left[-\frac{(x-p_0)^2}{2{p_1}^2}\right] + p_4(x-p_0) + p_5,$$

with

$$erfc(x) = 1 - \mathrm{erf}(x) = \frac{2}{\sqrt{\pi}} \int_x^{\infty} exp(-t^2)\, dt, \tag{5.11}$$

where p_0 is the average Compton edge energy E_{max}, p_1 is the standard deviation of the edge width, p_2 is the slope above the edge, p_3 is the amplitude of the edge, p_4 is the slope below the edge and p_5 is the background offset.

For Fig. 5.1 (b), the edge fitting gives E_{max} as 1580.50 keV ± 0.28 keV, as shown in Fig. 5.8. Given that the systematic uncertainty from the detector calibration is much smaller than 10^{-4}, then the statistical uncertainty dominates σ_{Emax}/E_{max}, which is 1.8×10^{-4}.

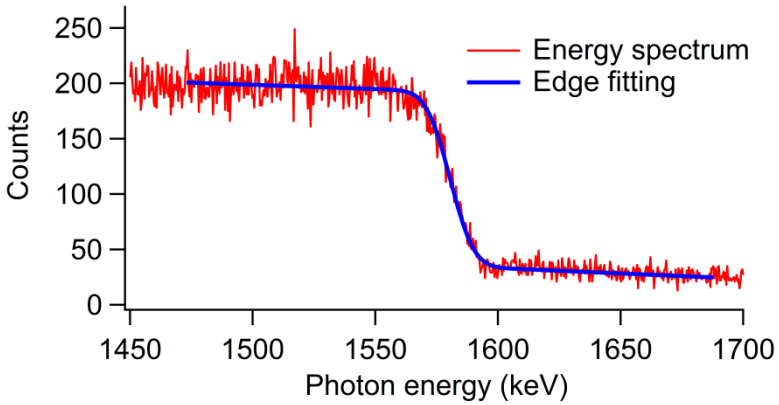

Figure 5.8: Zoom into Compton edge of Fig. 5.1 (b) and curve fitting at 1.3 GeV, χ^2/ndf = 528/555.

5.1.4 Calculation of electron beam energy and its relative uncertainty

Using well known literature parameters mc^2 = 0.5109989 MeV, E_l = 0.1211591 eV and the measured values φ = 91.620°, E_{max} = 1580.50 MeV, we can calculate E_e = 1286.98 MeV using Eq. 2.4. We can also get $\sigma_{Ee}/E_e = 1.4 \times 10^{-4}$ using Eq. 2.5. Subsequently, we can determine the energy we measured at 1.3 GeV is $E_e \pm \sigma_{Ee}$ = 1287.0 MeV ± 0.2 MeV.

5.2 Optimization of the system

In order to maximize the recorded CBS edge photons, the position of the laser focal spot has been optimized by adjusting the focusing cylindrical lens. The influence of detection shaping time (the rise time) has been studied. Also the position and aperture size of the collimator together with the amplitude of the electron beam orbit bump have been investigated.

5.2.1 Overlap between laser beam and electron beam

Fig. 5.9 shows a sketch of geometrical configuration of the motorized STANDA translation stages with focusing cylindrical lens. The travel range for each stage is 1- 25 mm with full step resolution of 1.25 µm and repeatability of 1 µm. We can scan in Z and Y direction to get the optimum working position for overlap between the laser and the electron beam. Fig. 5.10 and Fig. 5.11 show the measurement results for the initial detection table position and electron beam orbit with all the correctors on and no orbit bump applied (referred as the unaltered beam orbit hereafter). The optimum Z position is around9.45 mm and Y position is around 13 mm, around 16 mm and around 20 mm. About 6 months later, another measurement shows similar profiles as in Fig. 5.12 and Fig. 5.13 except the optimum Z position is around9.66 mm and Y position is around 14.0 mm or around 20.5 mm, when the electron beam is set around -0.0175° relative to the RL with around 0.994 mm transverse offset at the collision point (CP) to circumvent the misaligned absorber. Due to the orbit bump at CP, the optimum Y position increases around 1 mm. The reason that the Z position needs to be 2 mm higher is probably because the holding structure for the laser table becomes lower as time goes by.

The fluctuation of the Compton edge height indicates the change of the electron-laser interaction luminosity, thus further infers the ununiformed profile and intensity distribution near the laser focal plane along Z and Y direction.

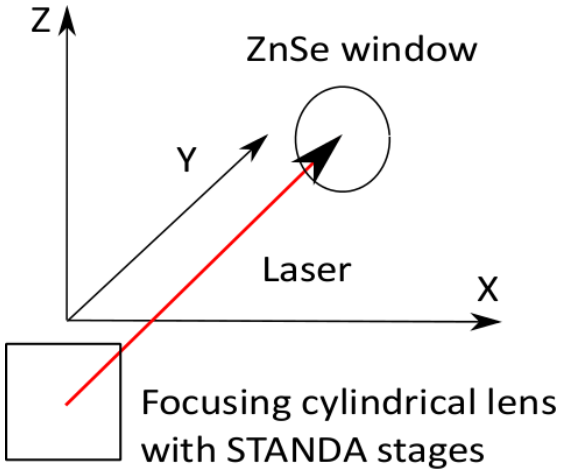

Figure 5.9: Geometrical configuration of the motorized translation stages with the cylindrical lens.

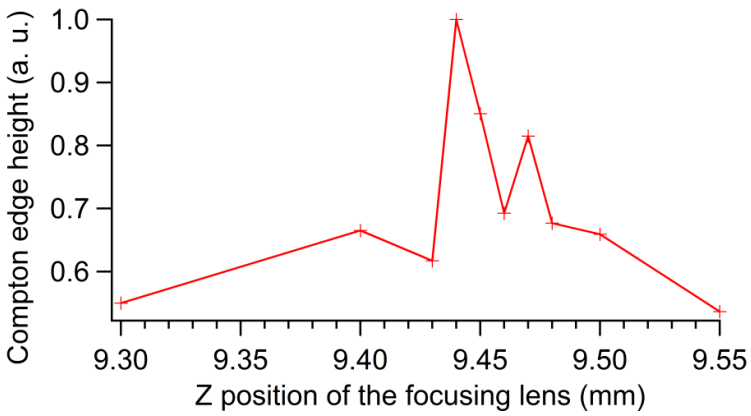

Figure 5.10: Vertical scan of the focusing cylindrical lens, Y position fixed at 13 mm, optimum position is around 9.45 mm. Results are obtained with the initial detection table position and electron beam orbit with all the correctors on and no orbit bump applied.

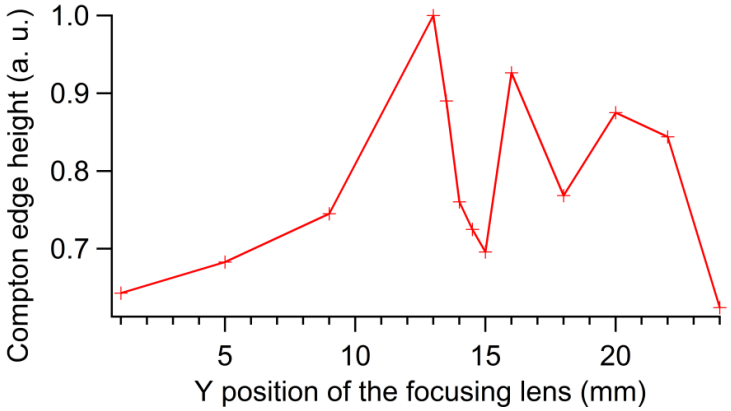

Figure 5.11: Y scan of the focusing cylindrical lens, Z position fixed at 9.45 mm, optimum position is around 13 mm. Results are obtained with the initial detection table position and electron beam orbit with all the correctors on and no orbit bump applied.

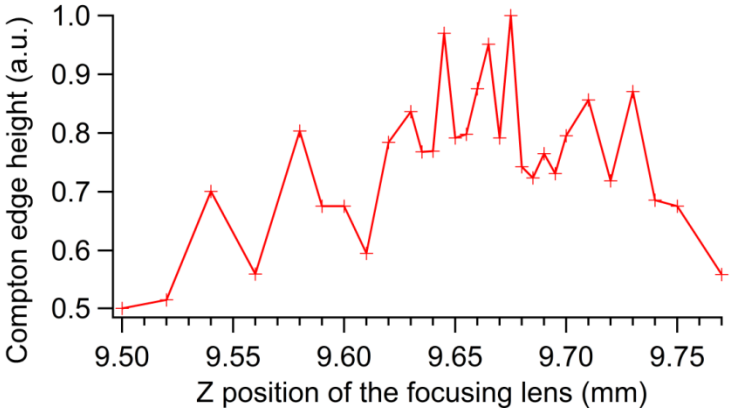

Figure 5.12: Vertical scan of the focusing cylindrical lens, Y position fixed at 13 mm, optimum position is around 9.66 mm. Results are obtained with the new detection table position and electron beam orbit 6 months after the measurement in Fig. 5.10.

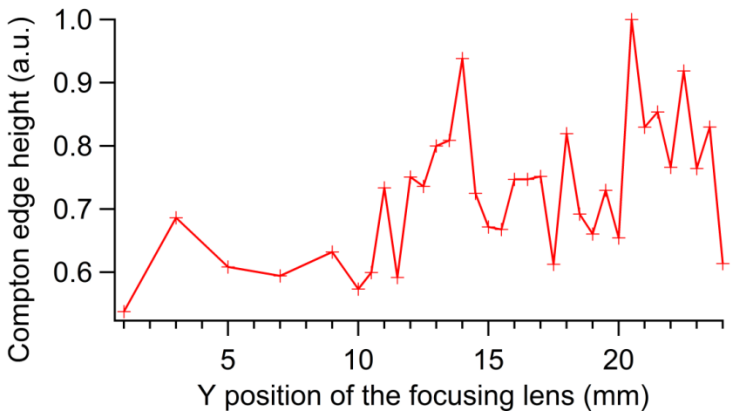

Figure 5.13: Y scan of the focusing cylindrical lens, Z position fixed at 9.66 mm, optimum position is around 14.0 mm or 20.5 mm. Results are obtained with the new detection table position and electron beam orbit 6 months after the measurement in Fig. 5.11.

5.2.2 Optimization of the electron beam orbit and the collimator position

Fig. 5.14 shows geometrical configuration of the motorized ISEL translation stages with the collimator. The travel range for each stage is 490 mm with repeatability of ± 0.02 mm. Behinds the collimator there is the shielding lead blocks with 10 mm diameter opening at the center. When the collimator moves to the X position around 12.7 mm, 32.7 mm, 52.7 mm and 72.7 mm and Y position around 25.7 mm, the center of the collimator aperture and the center of the lead blocks overlap with each other. The whole detection system has been pre-aligned with respect to a reference of the multi-magnet package nearby.

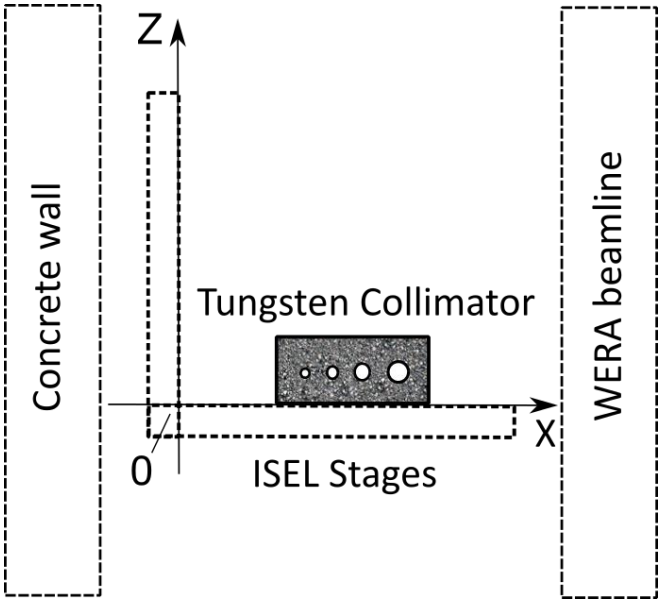

Figure 5.14: Geometrical configuration of the ISEL motorized translation stages. The tungsten collimator with different apertures is located on the horizontal stage. There is lead shielding blocks with a 10 mm opening behinds the collimator. Detail description can be found in section 3.2.2.6.

5.2.2.1 Measurement at the unaltered electron beam orbit

Since the unaltered electron beam propagation direction is nearly the same as the RL with negligible offset angle around 10^{-5} rad, the optimum position to receive the maximum Compton edge photons under unaltered electron beam obit shown in Fig. 5.15 indicates the detection system originally has around 2 mm offset relative to the RL.

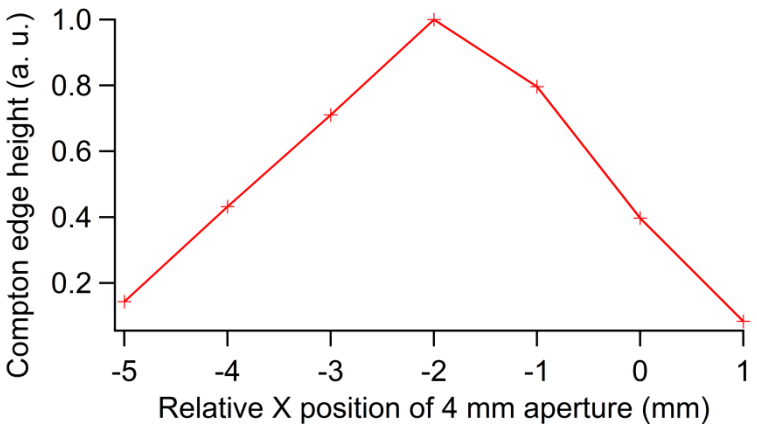

Figure 5.15: Compton edge height from unaltered electron beam orbit received by the 4 mm collimator aperture at different relative X position. The X position is the relative position to the center of the lead blocks. The edge height is normalized to the maximum value.

The different collimator apertures receive the energy spectrum as shown in Fig 5.16 when they are located at their optimum positions. Since now the electron beam orbit is very close to the RL, most Compton edge photons would hit on and scatter with the absorber. After scattering, the edge gains additional energy spread, its height becomes lower and width becomes wider than the expected value. The width of the Compton edge with such unaltered electron beam orbit is around 15 keV.

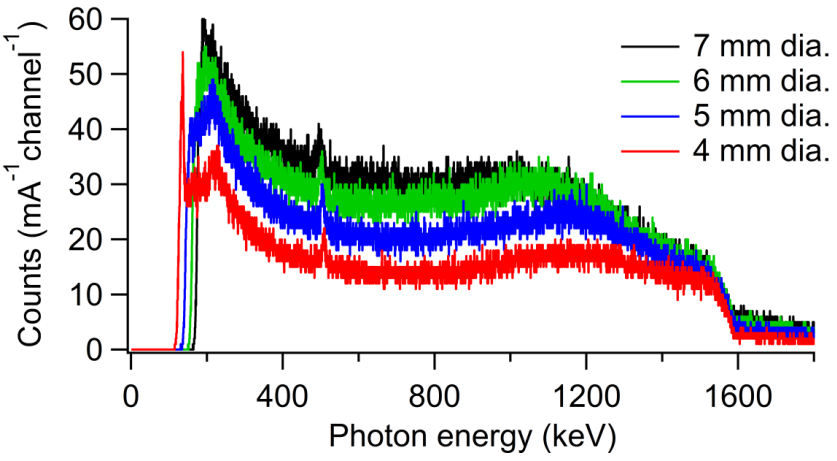

Figure 5.16: CBS photons from unaltered electron beam orbit received by different collimator aperture located at the optimum X positions. The photon counts are normalized with respective electron beam current. The detection live time is set to 120 seconds for each spectrum with every channel around 0.382 keV.

Although we cannot determine the edge energy precisely from such spectrum, it is clear that the 4 mm aperture receives much fewer low energy CBS photons than the bigger apertures, and yet covers well the Compton edge signal photons.

5.2.2.2 Measurement with an orbit bump

When the horizontal corrector MCH_S04_01 is turned off (since it is between the two BPMs in Fig. 5.2, it has to be turned off, otherwise we cannot determine the electron propagation direction and thus the precise collision angle), the electron beam orbit gains a relatively large angle around 0.0092° relative to the RL, and the transverse offset of the orbit at the CP is still close to 0. With such large angle, much more Compton edge photons can circumvent the absorber and reach the detector. Also the optimum X position of the collimator now changes further to -3 mm, as shown Fig. 5.17. The collimator at -3 mm already reaches the edge of the lead block opening for such 4 mm aperture.

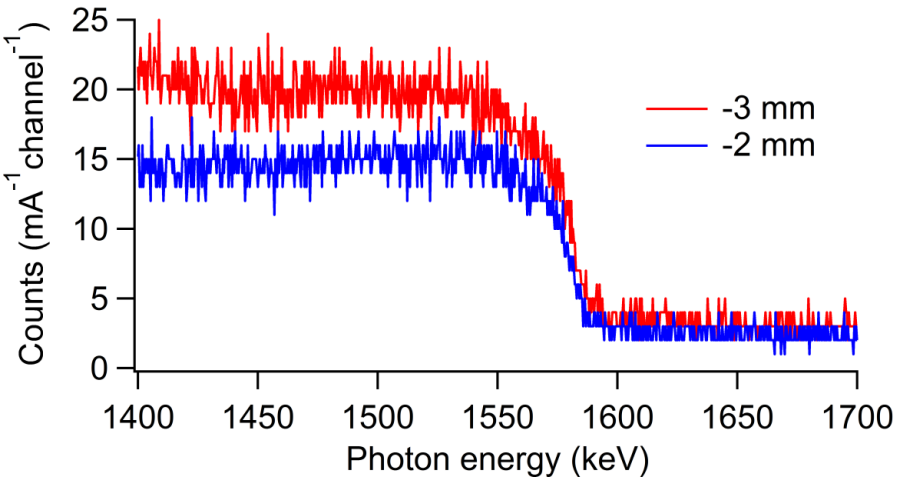

Figure 5.17: CBS photons with the corrector MCH_S04_01 turned off. The electron orbit now is around 0.0092° relative to the RL, the transverse offset at the CBS collision point is still close to 0. The red line indicates the 4 mm aperture at the relative X position of -3 mm, receiving much more Compton edge photons, which already reaches the limit of the lead block opening. The photon counts are normalized with the respective electron beam current. The detection live time is set to 120 seconds for each spectrum with every channel around 0.382 keV.

Although the Compton edge photon intensity improves a lot, its shape and width still does not reach the optimum state, thus an additional orbit bump has to be applied to let more edge photons pass through. The comparison between different electron beam orbits can be seen in Fig. 5.18. The orbit bump gives an electron beam with a propagation angle of around 0.012° relative to the RL and estimated 0.22 mm transverse offset at the CP, although it is only slightly larger than that without the orbit bump, the Compton edge shape is much more improved.

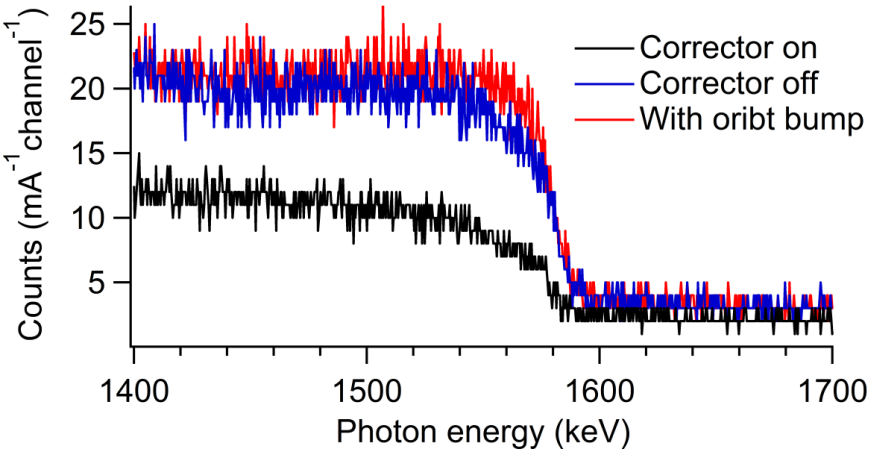

Figure 5.18: Comparison between different electron beam orbits. Black: the unaltered orbit close to the RL; Blue: with the corrector MCH_S04_01 turned off; Red: with the corrector off and an additional orbit bump of around 0.012° propagation angle relative to the RL and 0.22 mm transverse offset at the CP. The relative X position of the collimator 4 mm aperture is -3 mm. The photon counts are normalized with respective electron beam current. The detection live time is set to 120 seconds for each spectrum with every channel around 0.382 keV.

However, the orbit bump cannot be too big as we can see in the comparison between different orbit bumps in Fig. 5.19 and Table 5.2. The orbit bump strength increases as the index number increases, therefore the propagation angle relative to the RL and the transverse offset at the CP becomes larger. The edge shape parameters are from curve fittings based on Eq. 5.1. The optimum bumps for the edge height are indexed 2 and 3. The further increase of the orbit bumps does not improve the edge height, because very large obit bumps would push the signal beam exceeding the other limit of the collimator aperture, and the 4 mm collimator aperture already moves to the limit relative to the lead block opening behind the collimator.

The edge width decreases as the orbit bump strength increases, especially from bump 1 to bump 3. It means that fewer edge photons received by the detector have hit on and passing through the absorber copper block, therefore the edge shape is not altered by the pseudo energy spread towards low energy from photon-absorber interaction. For bump 4, however, the edge width only slightly decreases in contrast to bump 3, but the edge height decreases so much that the edge slope is not as steep as that of bump 3. Therefore it should be the effect of cutting off too many Compton edge photons by the collimator aperture. Thus the optimum orbit bump strength should be around bump 3 in such circumstances.

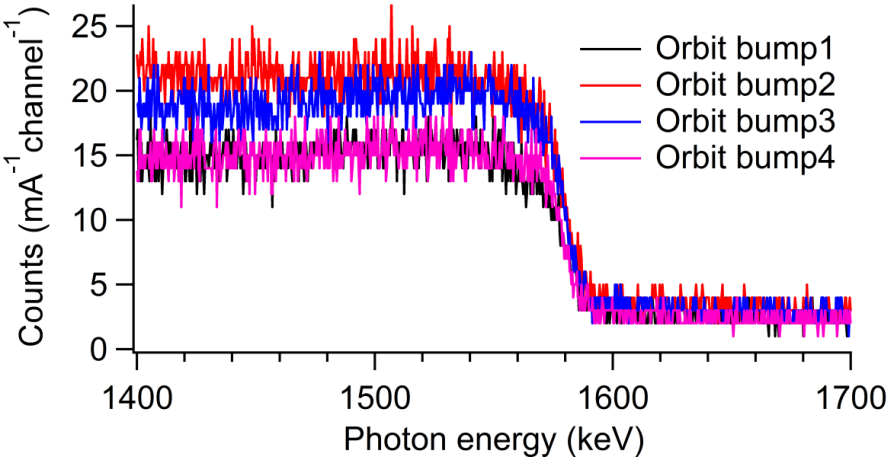

Figure 5.19: Comparison of the Compton edge with different electron beam orbit bumps and the corrector MCH_S04_01 turned off. Black: Orbit bump 1; Red: Orbit bump 2; Blue: Orbit bump 3; Purple: Orbit bump 4. Their angle to the RL and transverse offset at the CP is summarized in Table 5.2. The relative X position of the 4 mm aperture is -3 mm. The photon counts are normalized with respective electron beam current. The detection live time is set to 120 seconds for each spectrum with every channel around 0.382 keV.

Table 5.2: Compton edge shape parameters from curve fitting under 4 different orbit bumps.

Orit bump	Angle relative to the RL (degree)	Transverse offset at CP (mm)	Compton edge height (counts/channel/mA)	Edge width (keV)	Edge slope (counts/channel/ mA/keV)
1	0.00625	-0.231	11.6	8.13	1.42
2	0.0120	0.093	16.3	7.57	2.15
3	0.0153	0.203	15.9	6.51	2.44
4	0.0187	0.248	12.2	6.41	1.90

5.2.2.3 Measurement with the improved detection table position

Since the opening of the lead blocks limits the amplitude of the orbit bump we can apply, the whole detection table is further translated by around -1.5 mm to improve acceptance of the signal photons. From Fig. 5.20, we can see that with the corrector MCH_S04_01 turned off, the best relative X position of the collimator aperture now is -1.5 mm, confirming the expectation.

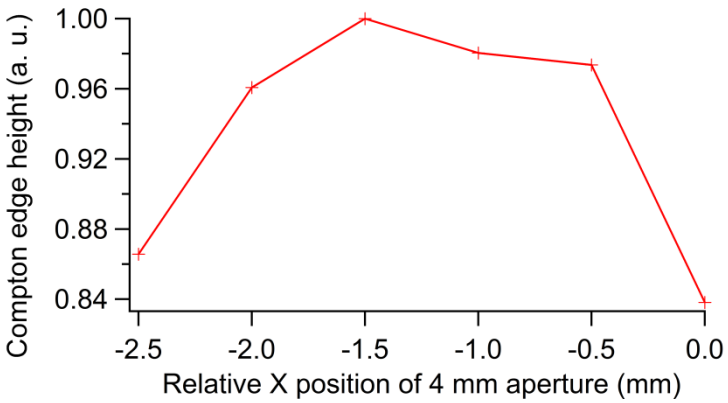

Figure 5.20: Compton edge height received by the 4 mm collimator aperture at different relative X position after the table was translated around -1.5 mm. The X position is relative to the center of the lead blocks. The corrector MCH_S04_01 is turned off. The edge height is normalized to the maximum value.

With an orbit bump applied, the optimum collimator position to receive Compton edge photons would further move to -2 mm as we can see in Fig. 5.21. The influence of the collimator position over the shape and energy of the Compton edge can be found in Table 5.3. Note that the Compton edge energies and the corresponding uncertainties given by edge fitting are based on the total spectrum without normalization according to respective current. The orbit bump should be big enough to allow most of the Compton edge photons pass though the absorber without scattering.

Table 5.3: Shape and energy parameters of Compton edge for measurement in Fig. 5.21.

Relative X position (mm)	Compton edge height (counts/channel/mA)	Edge width (keV)	Edge slope (counts/channel/ mA/keV)	Compton edge energy (keV)
0	13.90056	6.5419	2.124851	1579.99 ± 0.27
-1.0	16.68711	7.75731	2.151147	1580.10 ± 0.28
-1.5	17.61923	7.90125	2.22993	1580.62 ± 0.29
-2.0	18.27728	8.5582	2.135646	1580.23 ± 0.29
-2.5	16.93677	7.60617	2.226715	1580.51 ± 0.28
-3.0	15.6757	6.97609	2.247061	1581.49 ± 0.27

As we can see from Table 5.3, although the optimum position to receive the maximum edge photons is at -2.0 mm, the width is also the biggest compared to other positions, meaning that a large amount of pseudo edge photons can be recorded. If we move the collimator further back towards 0 mm, fewer pseudo edge photons can reach the detector but the edge height decreases, therefore the edge width is smaller and the steepness of the slope is not improved. However, if the collimator is moved further towards -3.0 mm, the edge also becomes narrower with the slope even steeper, thus the reduction of edge width cannot be caused by the small aperture size effect as discussed in [22,48]. The energy determined from the edge curve at -3.0 mm is much higher than those from the other positions, which corresponds to less reception of pseudo edge photons. The comparison between the edge shape and curve fitting can be seen in Fig. 5.22. The edge curve is much steeper at

X position of -3.0 mm. Thus, -3.0 mm should be the best position of the collimator. Note that -3.0 mm already reaches the limitation of the lead block opening.

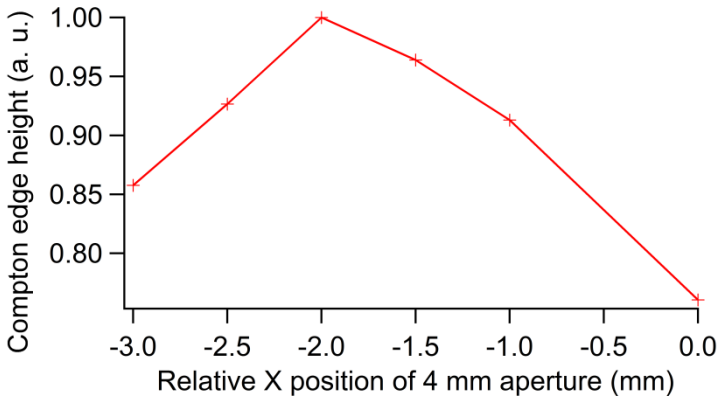

Figure 5.21: Compton edge height received by the 4 mm collimator aperture at different relative X position with corrector MCH_S04_01 turned off and an orbit bump of around 0.00959° propagation angle relative to the RL and 0.855 mm transverse offset at the CP. The RF frequency is 499.72 kHz. The detection table was translated around 1.5 mm towards the concrete wall now. The X position is relative to the center of the lead blocks. The edge height is normalized to the maximum value.

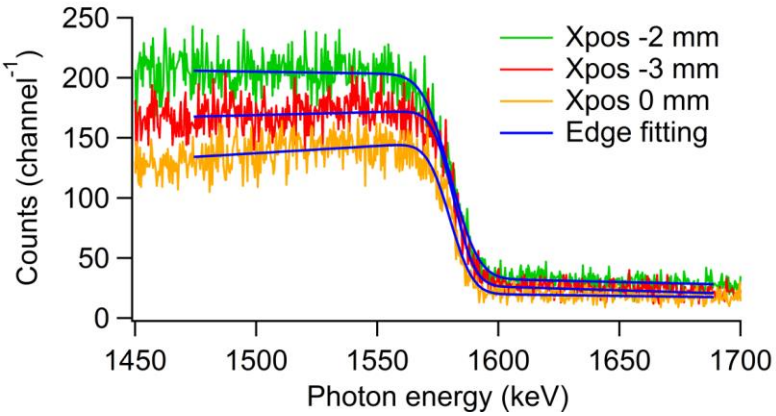

Figure 5.22: Comparison between Compton edges for measurements in Fig. 5.21. Green: X position at -2.0 mm for 9.2 mA electron beam current; Red: X position at -3.0 mm for 9.3 mA electron beam current; Yellow: X position at 0 mm for 8.9 mA electron beam current.

Even if the orbit bump is only slightly deficit (an orbit bump of around 0.00916° propagation angle relative to the RL and 0.397 mm transverse offset at the CP), much more edge photons would hit on the absorber and the edge can hardly be narrow any more with a proper edge height as shown in Table 5.4. As we can see the Compton edge height in Fig. 5.23, the optimum position to receive maximum edge photons is still around -2.0 mm, but it is not sensitive any more, over a large distance towards 0 mm the signal count rate does not change significantly.

Table 5.4: Shape and energy parameters of Compton edge for measurement in Fig. 5.23.

Relative X position (mm)	Compton edge height (counts/channel/mA)	Edge width (keV)	Edge slope (counts/channel/ mA/keV)	Compton edge energy (keV)
-0.5	14.16102	8.29404	1.707373	1580.33 ± 0.31
-1.0	15.07969	8.41785	1.791395	1580.31 ± 0.32
-1.5	15.08479	8.12111	1.857479	1580.85 ± 0.31
-2.0	15.17115	8.75621	1.732616	1580.18 ± 0.33
-2.5	5.609937	6.88774	0.814482	1581.23 ± 0.44

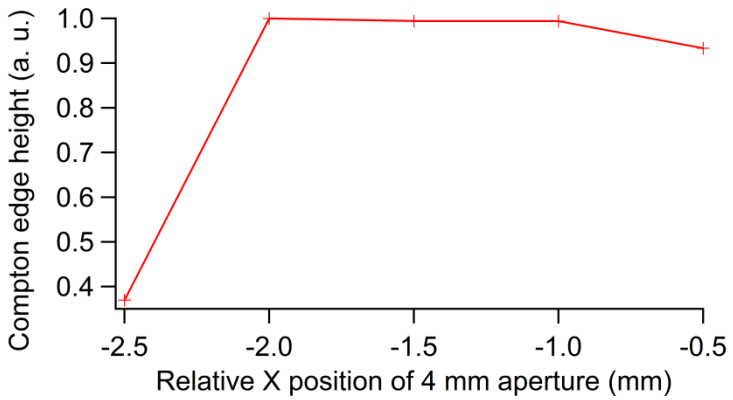

Figure 5.23: Compton edge height received by the 4 mm collimator aperture at different relative X position with corrector MCH_S04_01 turned off and an orbit bump of around 0.00916° propagation angle relative to the RL and 0.397 mm transverse offset at the CP. The RF frequency is 499.72 kHz. The detection table is translated around -1.5 mm. The X position is relative to the center of the lead blocks. The edge height is normalized to the maximum value.

5.2.2.4 Measurement beyond the limitation of the lead block opening

If the collimator further moves towards the concrete wall, beyond the limitation of the lead block opening, the actual aperture to receive CBS photons is smaller than the entire collimator aperture. As we can see in Table 5.5 (with a similar orbit bump as that for Table 5.4, around 0.00979° propagation angle relative to the RL and 0.845 mm transverse offset at the CP, the RF frequency: 499.7207 kHz), the edge width will continuously decrease but the edge slope reaches the maximum at the relative position of -3.5 mm.

As we have calculated in section 4.2 that if the 4 mm aperture is misaligned by 2 mm, the misjudgment of the edge energy would reach the same level as the measurement uncertainty of around 10^{-4}, the determination of the edge energy is not accurate anymore. If we assume that the 4 mm aperture at -2.0 mm, which receives the most signal, is the correct collimator position relative to the edge photons, then the position at -4.0 mm already reaches the limit of the properly aligned range. Also we can see that the energy determined by the Compton edge signals at -4.0 mm is much larger than those at -2.5 mm, -3.0 mm and -3.5 mm, which is already beyond the statistical

uncertainty around 0.3 keV. It indicates that the energy determination at -4.0 mm is not accurate any more. Therefore, the collimator located at -3.5 mm should be optimum.

Table 5.5: Shape and energy parameters of Compton edge beyond the limitation of the lead block.

Relative X position (mm)	Compton edge height (counts/channel/mA)	Edge width (keV)	Edge slope (counts/channel/ mA/keV)	Compton edge energy (keV)
-2.0	11.6749	6.74054	1.73204	1578.08 ± 0.27
-2.5	11.2386	6.38035	1.76145	1579.16 ± 0.28
-3.0	10.8780	5.90205	1.84308	1579.11 ± 0.26
-3.5	9.88000	5.04785	1.95727	1578.93 ± 0.24
-4.0	7.22861	4.64684	1.55560	1579.77 ± 0.27

Under the same fill and orbit bump, we can also compare different aperture size with the respective aperture center located at -3.5 mm, see Fig. 5.24. The Compton edge has been covered well by 4 mm aperture just as expected from simulation results, and the low energy CBS photons are much less than those received by the bigger apertures.

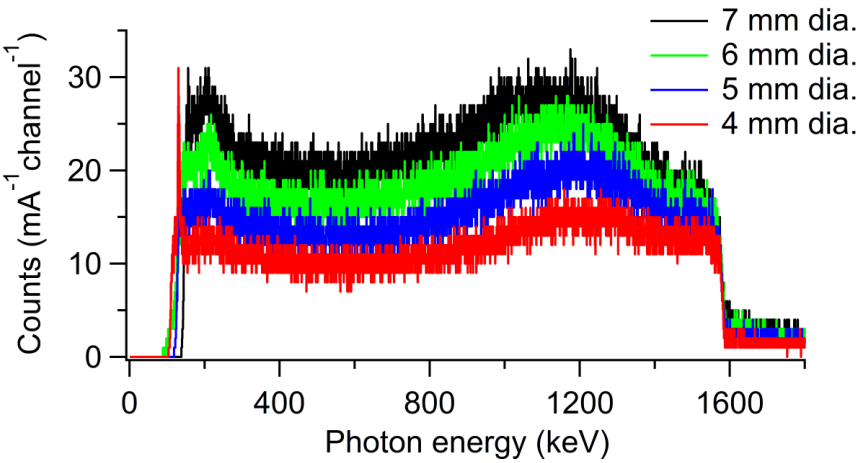

Figure 5.24: Comparison between the energy spectra received by different collimator apertures at 1.3 GeV for 120 seconds live time with aperture center located at -3.5 mm. The corrector MCH_S04_01 is turned off and an orbit bump of around 0.00979° propagation angle relative to the RL and 0.845 mm transverse offset at the CP is applied. The RF frequency is 499.7207 kHz. The photon counts have been normalized with regard to respective electron beam current.

We can further zoom in to compare the edge area in Fig. 5.24 as Fig. 5.25 and Table 5.6. The edge energy determined by edge curve fitting decreases continuously as the aperture size increases, because bigger aperture tends to receive more pseudo edge photons with slightly lower energy from scattering on the absorber. The edge height also increases until the aperture size reaches 6 mm, then reduces slightly for 7 mm aperture. The edge width also has the same tendency. Since the edge photons and the noise photons (photons with energies much lower than the Compton edge energy) compete over the limited detection time, i.e. the chances to be recorded, it is possible that 6 mm aperture is already big enough to cover all of the edge photons. Further increase of the aperture will

receive noise photons, therefore the proportion of the edge photons drops and the edge height recorded is even smaller than that of the 6 mm aperture. Since the proportion between noise photons and edge photons changes, the shape of the curve is possibly altered, thus the edge fitting gives an even smaller edge width for 7 mm aperture.

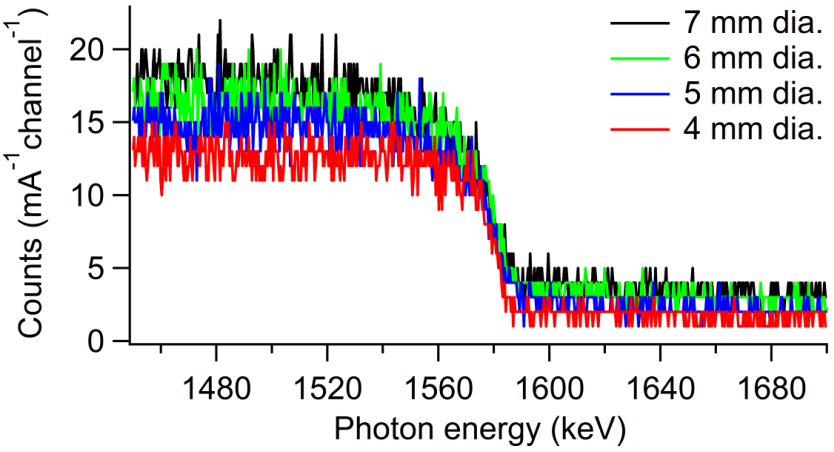

Figure 5.25: Comparison between Compton edges received by different collimator apertures at 1.3 GeV for 120 seconds live time with aperture center located at -3.5 mm. The corrector MCH_S04_01 is turned off and an orbit bump of around 0.00979° propagation angle relative to the RL and 0.845 mm transverse offset at the CP is applied. The RF frequency is 499.7207 kHz. The photon counts have been normalized with regard to respective electron beam current.

Table 5.6: Shape and energy parameters of Compton edge for different collimator apertures.

Aperture size (mm)	Compton edge height (counts/channel/mA)	Edge width (keV)	Edge slope (counts/channel/ mA/keV)	Compton edge energy (keV)
4	9.88000	5.04785	1.95727	1578.93 ± 0.24
5	10.6955	7.04654	1.51784	1578.36 ± 0.31
6	11.3721	8.16444	1.39288	1577.75 ± 0.35
7	10.9179	6.82253	1.60027	1577.49 ± 0.33

Table 5.7: Shape and energy parameters of Compton edge for different positions of 7 mm apertures.

Relative X position (mm)	Compton edge height (counts/channel/mA)	Edge width (keV)	Edge slope (counts/channel/ mA/keV)	Compton edge energy (keV)
-1.5	11.6163	12.5719	0.923989	1574.61 ± 0.57
-2.0	11.5907	11.9686	0.968429	1574.40 ± 0.53
-2.5	11.7041	10.5175	1.112817	1576.13 ± 0.46
-3.0	11.3730	9.42925	1.206140	1576.11 ± 0.42
-3.5	11.4096	8.33986	1.368083	1576.95 ± 0.38

As for the 7 mm aperture, the different positions also have influence on the shape of the Compton edge and the judgment of the edge energy, as summarized in Table 5.7 (around 0.00954° propagation angle relative to the RL and 0.832 mm transverse offset at the CP, the RF frequency: 499.7206 kHz). The Compton edge height nearly does not change, which means the 7 mm aperture is big enough to cover all the edge signals. However, the edge width continuously decreases with less and less pseudo edge photons recorded by the detector. The determined edge energy grows from -2.0 mm to -2.5 mm, and remains relatively the same afterwards.

5.2.2.5 Optimization for low α_c mode

For a low α_c optics at 1.3 GeV (23 k steps), we can see the influence of 7 mm aperture position on the edge shape and energy determination in Table 5.8 (around 0.00961° propagation angle relative to the RL and 0.909 mm transverse offset at the CP, the RF frequency: 499.7206 kHz). The edge height nearly does not change from -2.5 mm to -4.0 mm, then continuously decreases from -4.0 mm to -6.0 mm, which means when the aperture center moves to -4.0 mm the edge photons begin to be cut off severely. The edge width decreases from -2.5 mm all the way down to -5.5 mm, then increases again to -6.0 mm, similarly the edge slope increases until the position reaches -5.5 mm, then reduces dramatically. It indicates that less and less pseudo edge photons are included in the spectrum until the aperture center reaches -5.5 mm.

When the aperture moves further to -6.0 mm, the opening between the left edge of the lead block opening and the right edge of the collimator aperture becomes too small, which is only 2.5 mm, the determination from the edge fitting will become fluctuating, thus the edge width even increases, but the slope decreases dramatically. Including all the consideration above, 7 mm aperture centered at -5.5 mm should be the best position to receive the edge photons. Also the edge energy at -5.5 mm is the largest with the smallest statistical uncertainty compared to those at other collimator positions.

Table 5.8: Shape and energy parameters of Compton edge for low α_c mode with 7 mm apertures.

Relative X position (mm)	Compton edge height (counts/channel/mA)	Edge width (keV)	Edge slope (counts/channel/ mA/keV)	Compton edge energy (keV)
-2.5	7.34401	11.5721	0.634631	1574.48 ± 0.59
-3.0	7.36051	9.91831	0.742113	1576.29 ± 0.51
-3.5	7.34630	8.90996	0.824504	1576.72 ± 0.46
-4.0	7.48412	8.59763	0.870486	1577.08 ± 0.43
-4.5	7.04622	7.55874	0.932195	1578.01 ± 0.39
-5.0	6.68121	6.40439	1.043224	1578.21 ± 0.35
-5.5	5.49488	4.74674	1.157611	1579.36 ± 0.30
-6.0	3.51974	5.64083	0.623976	1578.94 ± 0.42

5.2.3 Optimization of detector rise time

The rise time setting can also be optimized by comparison of the shape parameters of the Compton edge. The measurement with different rise time as summarized in Table 5.9, when the corrector MCH_S04_01 is turned off and the 4 mm collimator aperture is placed at optimum position to cover the most edge photons given by around 10 mA electron current at 1.3 GeV normal optics. The different rise time setting would cause different detection dead time, therefore all the detection conditions are set with live time of 120 seconds to minimize the effect. Due to the longer dead time, the total detection time increases accordingly.

Although the short rise times can save the real detection time, but possibly lead to ballistic deficit effect (see section 3.2.2.4), therefore undermine the energy resolution. We can see this effect by comparison of the Compton edge width with rise time settings of 1 μs, 3 μs, 6 μs and 12 μs, the edge width continuously improves as the rise time increases. For the rise time of 16 μs and 23 μs, however, the edge width increases again since rise time around 12 μs is sufficient to fully eliminate the ballistic effect, longer rise times would include much more noise, therefore even degrade the energy resolution. The edge slope can be a good indicator, since the edge height can compensate the degraded edge width for our edge energy determination by curve fitting according to Eq. 2.6. From the table we can see that rise time around 12 μs is the optimum regarding slope steepness, independent of the detector live time or the total measurement time.

Table 5.9: Edge shape and energy parameters for different rise times without orbit bump.

Rise time (μs)	Compton edge height (counts/channel/mA)	Edge width (keV)	Edge Slope (counts/channel/ mA/keV)	Total measurement time (s)
1	13.5671	13.2528	1.02372	127.26
3	13.8947	10.8286	1.28315	130.48
6	13.4265	10.8424	1.23833	136.64
12	13.2607	9.01407	1.47111	145.82
16	11.8543	10.1672	1.16593	149.82
23	11.0796	11.9296	0.928749	161.44

For the electron orbit with a local bump and appropriate position of the collimator aperture (7 mm aperture centered at relative position of -5.0 mm, electron beam current around 3.6 mA, the RF frequency: 499.7170 kHz, orbit bump: around -0.0109° propagation angle relative to the RL and 0.838 mm transverse offset at the CP), the influence of choosing different rise time can be found in Table 5.10. We can see that during the total measurement time of 120 seconds, the detector live time does not change significantly, since the photon count rate under around 3.6 mA electron current is much lower than that shown in Table 5.9. At this low electron current, the 23 μs rise time has the best edge width and slope steepness, but 12 μs still has the second best slope steepness. Furthermore, for such low electron current the detection time should be much longer than that for around 10 mA to reach the same statistical uncertainty. Therefore 12 μs rise time still has advantages. (Note that since the edge widths in Table 5.10 are under a special orbit bump and optimized collimator position, thus it is not directly comparable to those in Table 5.9.)

Table 5.10: Edge shape and energy parameters for different rise times with an orbit bump.

Rise time (μs)	Compton edge height (counts/channel/mA)	Edge width (keV)	Edge slope (counts/channel/ mA/keV)	Detector live time (s)
1	8.80073	7.96197	1.10535	118.34
6	10.6244	5.16767	2.05593	115.70
12	10.5014	4.75573	2.20816	112.74
18	10.0630	4.95498	2.03089	109.84
23	9.39443	3.81709	2.46115	108.20

In summary, for a normal current around 10 mA used in the 1.3 GeV measurement, 12 μs rise time should be optimal, while for a specially low current longer rise time can be used for further improvement of shorter detection time or better measurement uncertainty. Similar studies can be carried out for other energies, e.g. for 0.5 GeV both 6 μs and 12 μs rise time are appropriate because it only needs short rise time to appropriately process around 240 keV edge photons.

6. Measurement on electron beam energies at ANKA

Based on the established procedures and optimized settings in previous chapters, we can carry out systematic studies on precise measurements of the electron beam energies at ANKA. The momentum compaction factors of different optics at 1.3 GeV have also been measured.

6.1 Measurement during energy ramp up

Our transverse setup can well cover the whole energy range of ANKA from 0.5 GeV to 2.5 GeV. Fig. 6.1 to Fig. 6.10 show respective curve fitting and edge shape. Note that not every electron orbit bump is optimized with respect to the individual collimator's position. The 7 mm aperture is centered at -5.5 mm for 0.5 GeV, 0.6 GeV, 0.75 GeV, 1.0 GeV, 1.3 GeV, 1.85 GeV and 2.5 GeV; at -5.0 mm for 1.3 GeV, 1.6 GeV, 1.85 GeV, 2.1 GeV, 2.3 GeV and 2.5 GeV. Note that when the electron beam energy reaches 1.3 GeV, the CBS photons hitting on the detectors carrying too much energy lead to too high dead time of the detector, thus the electron beam current is reduced to around 3 - 4 mA, which is also suitable for further measurement at 2.5 GeV without saturation of the detector.

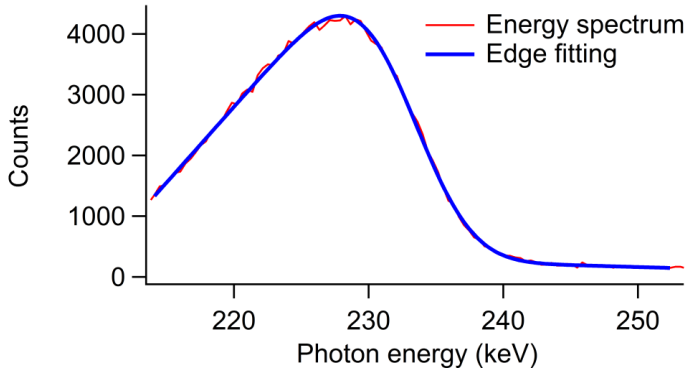

Figure 6.1: Compton edge and curve fitting for around 45 mA at 0.5 GeV for 120 seconds live time with the RF frequency of 499.7170 kHz. 7 mm aperture centered at -5.5 mm. Electron beam around -0.00528° relative to the RL and 1.76 mm transverse offset at the CP. φ = 91.625°. χ^2/ndf = 147/95, $E_{max} \pm \sigma_{Emax}$ = 232.99keV ± 0.03 keV, $E_e \pm \sigma_{Ee}$ = 494.11 ± 0.06 MeV.

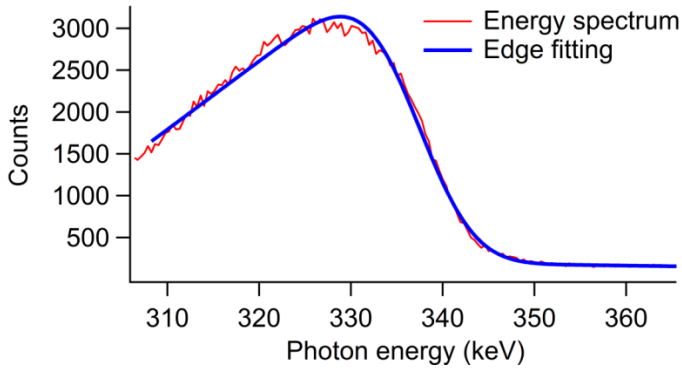

Figure 6.2: Compton edge and curve fitting for around 42 mA at 0.6 GeV for 120 seconds live time with the RF frequency of 499.7170 kHz, 7 mm aperture centered at -5.5 mm. Electron beam around -0.0109° relative to the RL and 0.888 mm transverse offset at the CP. φ = 91.619°, χ^2/ndf = 396/145, $E_{max} \pm \sigma_{Emax}$ = 337.01 keV ± 0.05 keV, $E_e \pm \sigma_{Ee}$ = 594.29 ± 0.08 MeV.

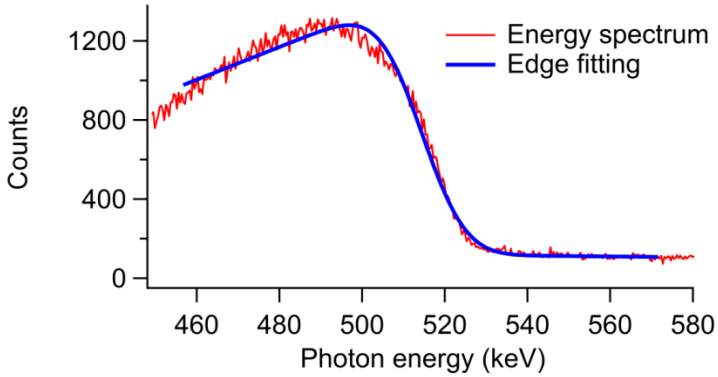

Figure 6.3: Compton edge and curve fitting for around 36 mA at 0.75 GeV for 120 seconds live time with the RF frequency of 499.7170 kHz. 7 mm aperture centered at -5.5 mm. Electron beam is around -0.00975° relative to the RL and 0.773 mm transverse offset at the CP. φ = 91.620°. χ^2/ndf = 606/295, $E_{max} \pm \sigma_{Emax}$ = 514.04 keV ± 0.12 keV, $E_e \pm \sigma_{Ee}$ = 734.0 ± 0.1 MeV.

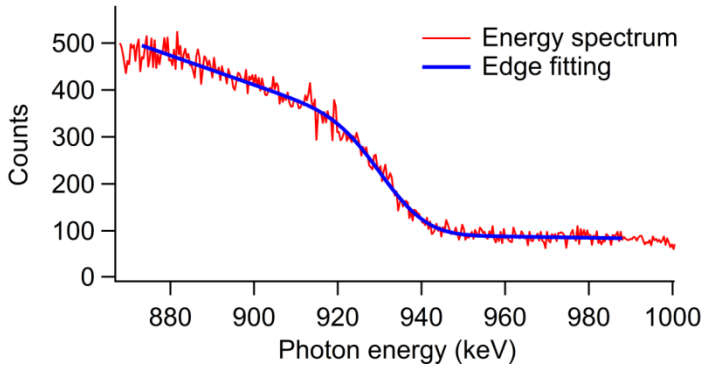

Figure 6.4: Compton edge and curve fitting for around 34 mA at 1.0 GeV for 120 seconds live time with the RF frequency of 499.7170 kHz. 7 mm aperture centered at -5.5 mm. Electron beam is around -0.00835° relative to the RL and 0.826 mm transverse offset at the CP. φ = 91.622°. χ^2/ndf = 316/295, $E_{max} \pm \sigma_{Emax}$ = 931.04 keV ± 0.44 keV, $E_e \pm \sigma_{Ee}$ = 987.8 ± 0.3 MeV.

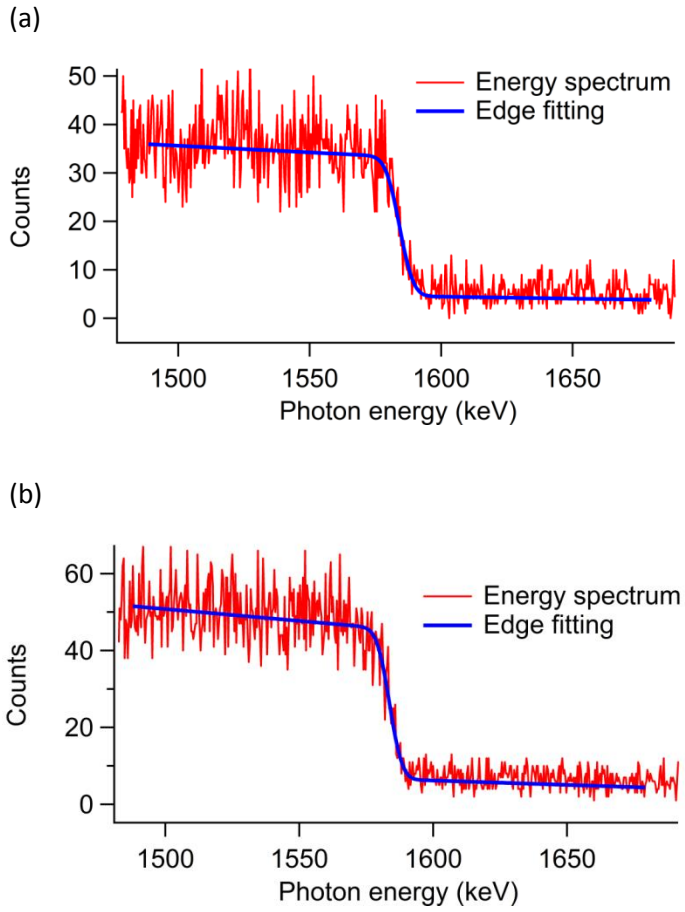

Figure 6.5: Compton edge and curve fitting for around 3.8 mA at 1.3 GeV for 120 seconds live time with the RF frequency of 499.7170 kHz. Electron beam is around -0.0109° relative to the RL and 0.838 mm transverse offset at the CP. φ = 91.619°. (a) -5.5 mm: $E_{max} \pm \sigma_{Emax}$ = 1584.13 keV ± 0.42 keV, χ^2/ndf = 617/494. $E_e \pm \sigma_{Ee}$ = 1288.5 ± 0.2 MeV. (b) -5.0 mm: $E_{max} \pm \sigma_{Emax}$ = 1583.71 keV ± 0.34 keV, χ^2/ndf = 576/495 $E_e \pm \sigma_{Ee}$ = 1288.3 ± 0.2 MeV.

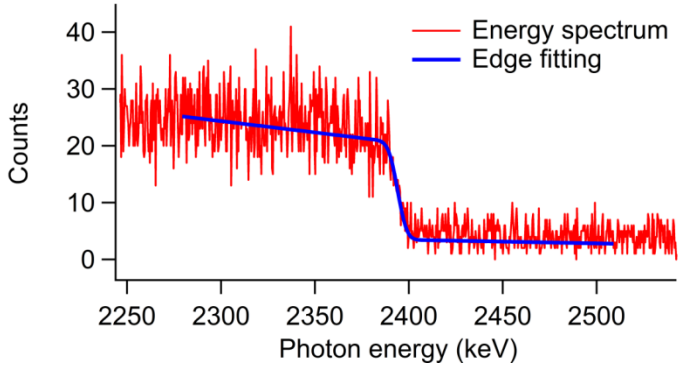

Figure 6.6: Compton edge and curve fitting for around 3.5 mA at 1.6 GeV for 120 seconds live time with the RF frequency of 499.7170 kHz. 7 mm aperture centered at -5.0 mm. Electron beam is around -0.0118° relative to the RL and 0.920 mm transverse offset at the CP. φ = 91.618°. χ^2/ndf = 672/593, $E_{max} \pm \sigma_{Emax}$ = 2394.02 keV ± 0.52 keV, $E_e \pm \sigma_{Ee}$ = 1584.0 ± 0.2 MeV.

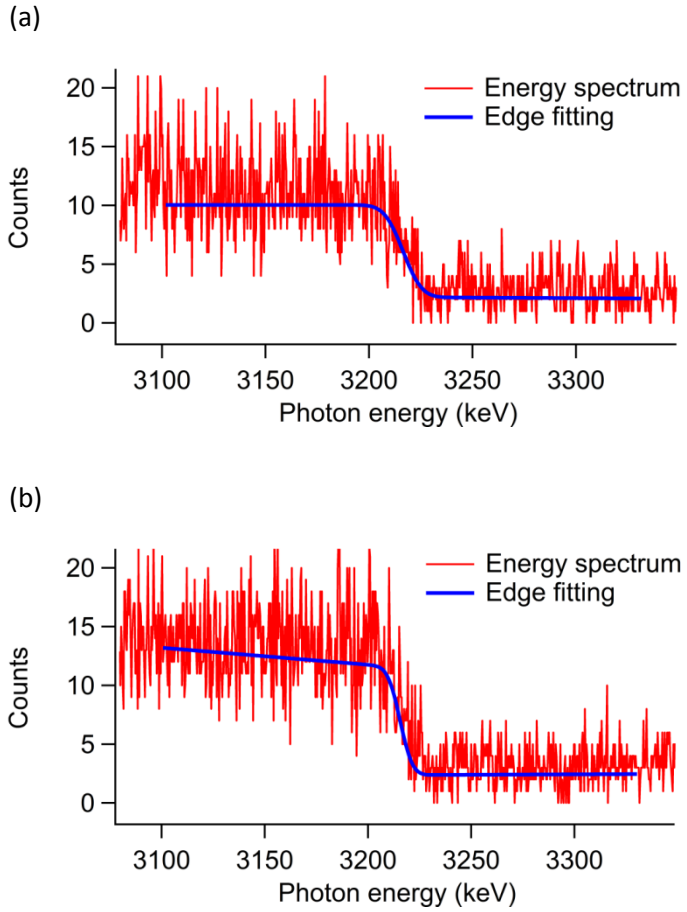

Figure 6.7: Compton edge and curve fitting for around 3.5 mA at 1.85 GeV for 120 seconds live time with the RF frequency of 499.7170 kHz. Electron beam is around -0.0159° relative to the RL and 0.609 mm transverse offset at the CP. φ = 91.614°. (a) -5.5 mm: $E_{max} \pm \sigma_{Emax}$ = 3216.5 keV ± 1.2 keV, χ^2/ndf = 583/578, $E_e \pm \sigma_{Ee}$ = 1836.0 ± 0.4 MeV. (b) -5.0 mm: $E_{max} \pm \sigma_{Emax}$ = 3215.57 keV ± 0.83 keV, χ^2/ndf = 626/582, $E_e \pm \sigma_{Ee}$ = 1835.8 ± 0.3 MeV.

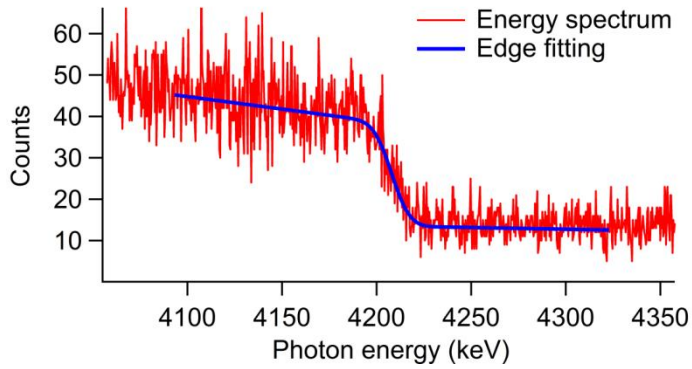

Figure 6.8: Compton edge and curve fitting for around 3.5 mA at 2.1 GeV for 600 seconds live time with the RF frequency of 499.7170 kHz. 7 mm aperture centered at -5.0 mm. Electron beam is around -0.0195° relative to the RL and 1.19 mm transverse offset at the CP. φ = 91.610°. χ^2/ndf = 646/595, $E_{max} \pm \sigma_{Emax}$ = 4208.05 keV ± 0.84 keV, $E_e \pm \sigma_{Ee}$ = 2100.1 ± 0.3 MeV.

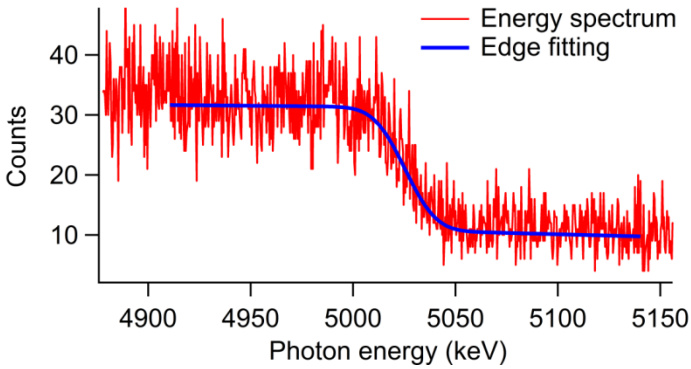

Figure 6.9: Compton edge and curve fitting for around 3.4 mA at 2.3 GeV for 600 seconds live time with the RF frequency of 499.7170 kHz. 7 mm aperture centered at -5.0 mm. Electron beam is around -0.0141° relative to the RL and 0.752 mm transverse offset at the CP. φ = 91.616°. χ^2/ndf = 605/595, $E_{max} \pm \sigma_{Emax}$ = 5025.3 keV ± 1.3 keV, $E_e \pm \sigma_{Ee}$ = 2294.9 ± 0.4 MeV.

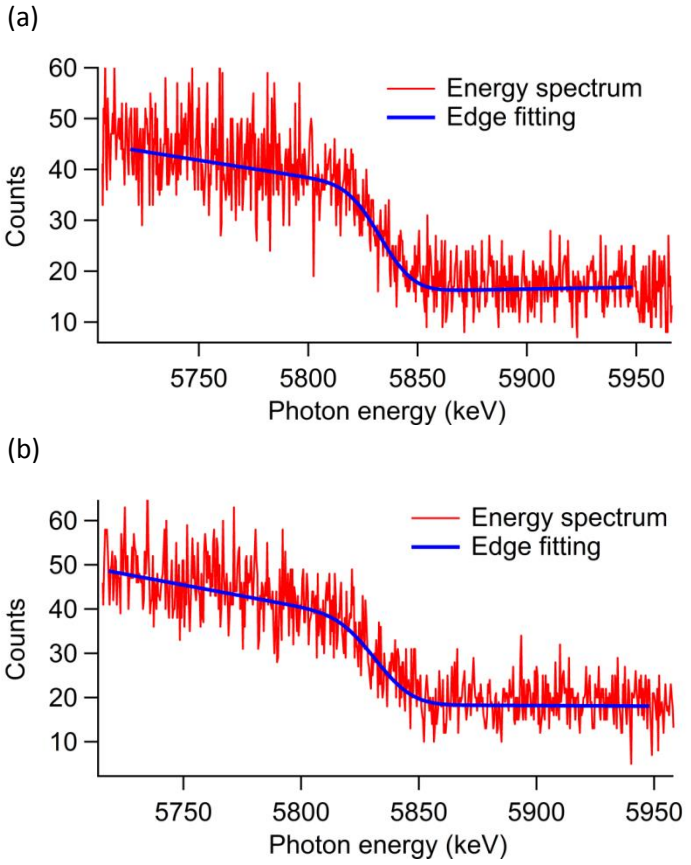

Figure 6.10: Compton edge and curve fitting for around 3.4 mA at 2.5 GeV for 1200 seconds live time with the RF frequency of 499.7170 kHz.

(a) -5.5 mm: Electron beam is around -0.0140° relative to the RL and 0.757 mm transverse offset at the CP. φ = 91.616°. χ^2/ndf = 657/595, $E_{max} \pm \sigma_{Emax}$ = 5833.4 keV ± 1.5 keV, $E_e \pm \sigma_{Ee}$ = 2472.6 ± 0.4 MeV.

(b) -5.0 mm: Electron beam is around -0.0108° relative to the RL and 0.882 mm transverse offset at the CP. φ = 91.619°. χ^2/ndf = 638/595, $E_{max} \pm \sigma_{Emax}$ = 5832.0 keV ± 1.8 keV, $E_e \pm \sigma_{Ee}$ = 2472.2 ± 0.5 MeV.

From the spectral edge shape and also from the χ^2/ndf, we can see that fitting curves at 0.5 GeV, 0.6 GeV, 0.7 GeV and 1.0 GeV are not very accurate, but are much improved for the higher energies from 1.3 GeV to 2.5 GeV. It is probably because the low energy Compton edge photons are much more easily scattered by the misaligned absorber and interfere with the Compton edge shape, since the collimator position is not optimized for the respective electron orbit. The high electron beam current would even magnify this effect. Thus the additional uncertainty from the pseudo edge photons makes the energy determination less accurate. However, these energies of 0.5 GeV, 0.6 GeV, 0.7 GeV and 1.0 GeV as summarized in Table 6.1, can still be regarded as a good reference within the relative uncertainty range of 10^{-3}.

For the nominal energies of 1.3 GeV, 1.85 GeV and 2.5 GeV, measurement results with 7 mm collimator aperture at -5.5 mm are slightly higher than those at -5.0 mm, because -5.5 mm tends to receive less pseudo edge photons than -5.0 mm.

For measurement at energies higher than 1.3 GeV, the edge width continuously grows, which can be an indicator of the increasing energy spread. In Table 6.2 we can see that the statistical uncertainty (σ_{Emax}/E_{max}) remains relatively the same until 1.85 GeV for the same amount of detection time. Above 1.85 GeV, much longer detection time is needed to keep the uncertainty at the same level for higher energies.

Table 6.1: Measurement with 7 mm collimator aperture at -5.5 mm. The σ_{Emax}^{*} is rescaled by multiplying square root of the χ^2/ndf and leads to σ_{Ee}^{*}.

Nominal operation energy (GeV)	$E_e \pm \sigma_{Ee}^{*}$ (MeV)	E_{max} (keV)	$\sigma_{Emax}^{*} / E_{max}$ (10^{-4})	Edge width (keV)	Current (mA)	Detection live time (s)
0.500	494.11 ± 0.07	232.99	1.71	3.55	45	120
0.607	594.3 ± 0.1	337.01	2.45	4.85	42	120
0.749	734.0 ± 0.1	514.04	3.34	8.52	36	120
0.999	987.8 ± 0.3	931.04	4.90	9.31	34	120
1.300	1288.5 ± 0.2	1584.13	2.96	4.15	3.8	120
1.853	1836.0 ± 0.4	3216.5	3.76	7.11	3.5	120
2.500	2472.6 ± 0.4	5833.4	2.70	11.8	3.4	1200

Table 6.2: Measurement with 7 mm collimator aperture at -5.0 mm. The σ_{Emax}^{*} is rescaled by multiplying square root of the χ^2/ndf and leads to σ_{Ee}^{*}.

Nominal operation energy (GeV)	$E_e \pm \sigma_{Ee}^{*}$ (MeV)	E_{max} (keV)	$\sigma_{Emax}^{*} / E_{max}$ (10^{-4})	Edge width (keV)	Current (mA)	Detection live time (s)
1.300	1288.3 ± 0.2	1583.71	2.50	3.74	3.8	120
1.601	1584.0 ± 0.3	2394.02	2.31	3.82	3.5	120
1.853	1835.8 ± 0.3	3215.57	2.58	4.67	3.5	120
2.112	2100.1 ± 0.3	4208.05	2.08	7.53	3.5	600
2.314	2294.9 ± 0.4	5025.3	2.61	12.0	3.4	600
2.500	2472.2 ± 0.5	5832.0	3.20	12.5	3.4	1200

6.2 Measurement with long detection time

Fig. 6.11 - Fig. 6.15 show the measurement at frequently used energies of 1.3, 1.6 and 2.5 GeV with especially long detection time. Compared to the measurement results in Section 6.1, due to the influence of the more pseudo edge photons, the long accumulation time/higher beam current tends to include more deformation of the edge curve as indicated by the larger edge width. It is especially the case for 1.3 GeV as in Fig. 6.11 and 6.12 in contrast of Fig. 6.5. For 1.6 GeV, the edge shape discrepancy between the short time/low current and the long time/high current is already reduced as comparison between Fig. 6.6 and Fig. 6.13. When the energy reaches 2.5 GeV, the overnight measurement in Fig. 6.15 shows the edge curve without much difference as that in Fig. 6.14 or Fig. 6.10. Although σ_{Emax}/E_{max} can be reduced despite of larger edge width, the uncertainty due to the laser centroid drift dominates the measurement uncertainty eventually. Therefore the especially long accumulation does not improve the final uncertainty significantly, especially for 1.3 and 1.6 GeV.

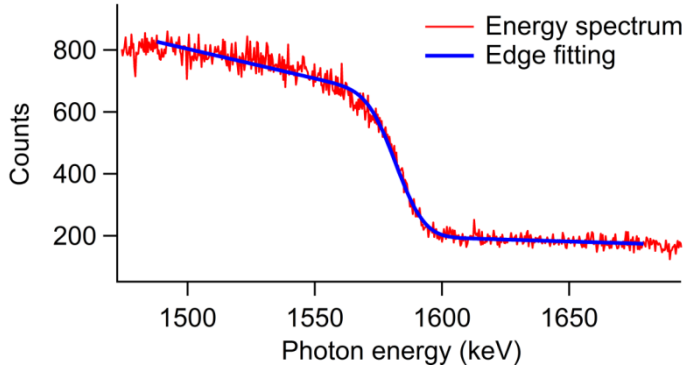

Figure 6.11: Compton edge and curve fitting for around 30 mA at 1.3 GeV for 480 seconds live time with the RF frequency of 499.7170 kHz. 7 mm aperture centered at -5.5 mm. Electron beam is around -0.0111° relative to the RL and 0.887 mm transverse offset at the CP. φ = 91.619°. Edge width is 8.83 keV. χ^2/ndf = 632/495, $E_{max} \pm \sigma_{Emax}$ = 1582.02 keV ± 0.23 keV, $E_e \pm \sigma_{Ee}$ = 1287.6 ± 0.2 MeV. Rescaling by square root of the χ^2/ndf gives σ_{Emax}^* as 0.26 keV but σ_{Ee}^* remains the same.

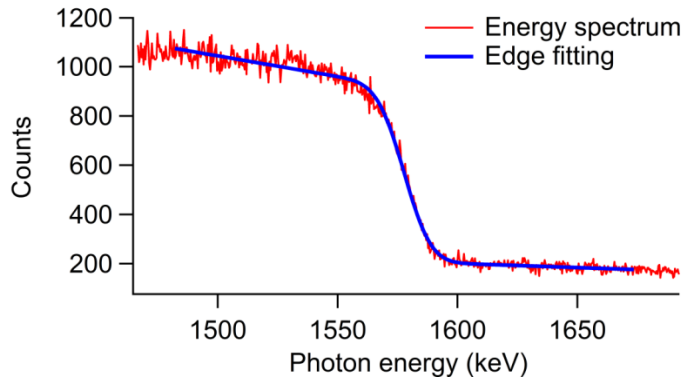

Figure 6.12: Compton edge and curve fitting for around 11 mA at 1.3 GeV for 1200 seconds live time with the RF frequency of 499.7237 kHz. 7 mm aperture centered at -5.0 mm. Electron beam is around -0.00760° relative to the RL and 0.822 mm transverse offset at the CP. φ = 91.622°. Edge width 8.77 keV. χ^2/ndf = 573/495, $E_{max} \pm \sigma_{Emax}$ = 1577.82 keV ± 0.17 keV, $E_e \pm \sigma_{Ee}$ = 1285.9 ± 0.2 MeV. Rescaling by square root of the χ^2/ndf gives σ_{Emax}^* as 0.18 keV but σ_{Ee}^* remains the same.

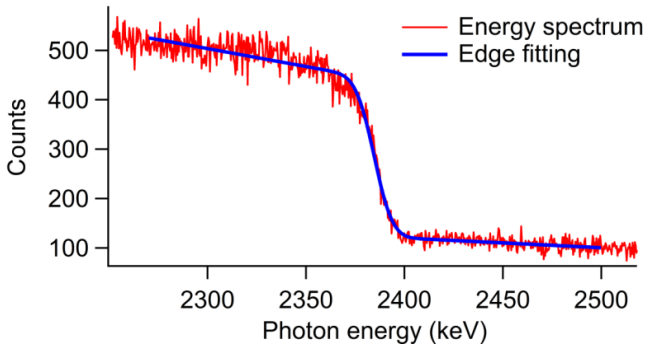

Figure 6.13: Compton edge and curve fitting for around 10.2 mA at 1.6 GeV for 1200 seconds live time with the RF frequency of 499.7229 kHz. 7 mm aperture centered at -5.0 mm. Electron beam is around -0.0110° relative to the RL and 0.922 mm transverse offset at the CP. φ = 91.619°. Edge width 7.28 keV. χ^2/ndf = 674/595, $E_{max} \pm \sigma_{Emax}$ = 2384.67 keV ± 0.21 keV, $E_e \pm \sigma_{Ee}$ = 1580.85 ± 0.2 MeV. Rescaling by square root of the χ^2/ndf gives σ_{Emax}^* as 0.22 keV but σ_{Ee}^* remains the same.

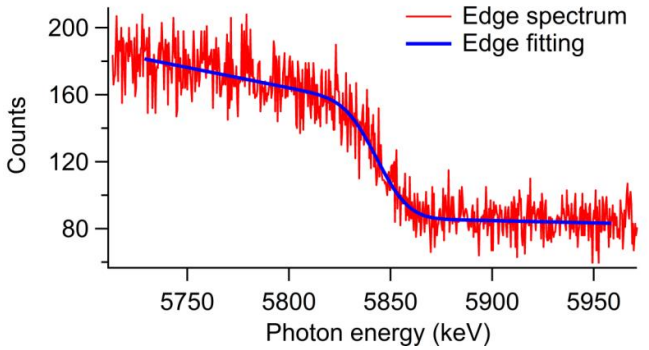

Figure 6.14: Compton edge and curve fitting for around 4.4 mA at 2.5 GeV for 3600 seconds live time with the RF frequency of 499.7114 kHz. 7 mm aperture centered at -5.0 mm. Electron beam around -0.0129° relative to the RL and 0.920 mm transverse offset at the CP. φ = 91.617°. Edge width 12.29 keV. χ^2/ndf = 650/595, $E_{max} \pm \sigma_{Emax}$ = 5843.6 keV ± 1.0 keV, $E_e \pm \sigma_{Ee}$ = 2474.7 ± 0.3 MeV. σ_{Emax}^* remains as 1.0 keV after rescaling by square root of the χ^2/ndf.

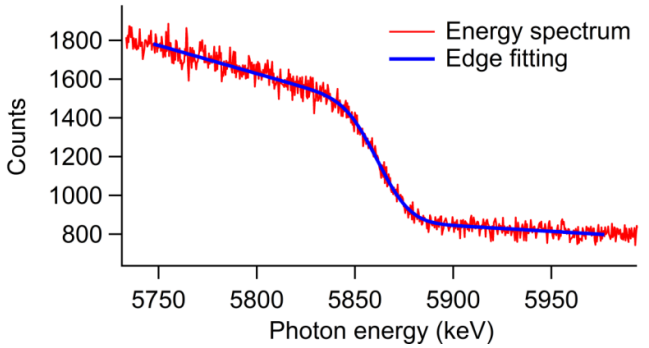

Figure 6.15: Compton edge and curve fitting for around 5 mA at around 2.5 GeV for around 60000 seconds live time with the RF frequency of 499.7052 kHz. 7 mm aperture centered at -5.0 mm. Electron beam around -0.00965° relative to the RL and 0.876 mm transverse offset at the CP. φ = 91.620°. Edge width 12.98 keV. χ^2/ndf = 615/595, $E_{max} \pm \sigma_{Emax}$ = 5861.97 keV ± 0.38 keV, $E_e \pm \sigma_{Ee}$ = 2478.5 ± 0.3 MeV. Rescaling by square root of the χ^2/ndf gives σ_{Emax}^* as 0.39 keV but σ_{Ee}^* remains the same.

6.3 Measurement of the momentum compaction factors at 1.3 GeV

The momentum compaction factor α_c is important, because they describe the relative change of orbit length due to the relative change of beam energy, which therefore has influence on the electron bunch length. The low-α_c optics at ANKA is obtained by changing the magnet strength step by step from the normal optics, thus various α_c values can be achieved continuously. The normal optics is referred as uncompressed optics, whereas the low-α_c optics is normally quoted using their undergone steps in the procedure as so called "squeeze steps". The larger step number means the shorter bunches are compressed. Frequently used low-α_c modes are 23 k steps, 25 k steps and 27 k steps.

A common way to measure the momentum compaction factor is to measure the beam energies at different RF frequencies,

$$\frac{\Delta L}{L_0} = -\frac{\Delta f_{RF}}{f_{RF0}} = \alpha_c \frac{\Delta E}{E_0}. \tag{6.2}$$

The momentum compaction factor can be further regarded as polynomial function of energy deviation as

$$\alpha_c = \alpha_0 + \alpha_1 \frac{\Delta E}{E_0} + \alpha_2 \left(\frac{\Delta E}{E_0}\right)^1 + \alpha_3 \left(\frac{\Delta E}{E_0}\right)^2 + \cdots. \tag{6.3}$$

We measured the momentum compaction factors mainly for low α_c mode at 1.3 GeV. Fig. 6.16 – Fig. 6.19 are the measurement at fill 5603 (A fill is from the injection to the dump of the electron beam, the number indicates its operation sequence.). Fig. 6.16 shows measurement result at normal optics of 1.3 GeV, linear fit can give α_0 as 0.0082 ± 0.0001. Fig. 6.17 shows measurement for low α_c optics with 23 k squeeze steps, the curve is not linear anymore, the quadratic term α_1 is -0.023 ± 0.007. As for 25 k squeeze steps in Fig. 6.18, even a cubic term appears, although the value is not very significant (α_0 is 0.00047 ± 0.00002, α_1 is -0.016 ± 0.004, α_2 is -2.0 ± 1.6).

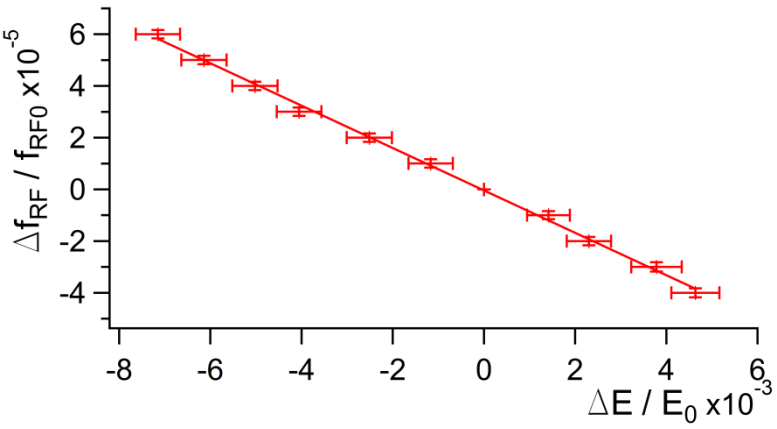

Figure 6.16: Momentum compaction factor for 1.3 GeV normal optics with central frequency f_{RF0} of 499.7206 kHz. The electron beam is around 10 mA. The 7 mm aperture centered at -2.5 mm. The vertical error bars are calculated from the horizontal error bars obtained from the energy measurement assuming linear dependence. The vertical error bars are rescaled once based on the initial χ^2/ndf value. Final linear fit of the curve gives α_0 as 0.0082 ± 0.0001, χ^2/ndf = 8.00/8.

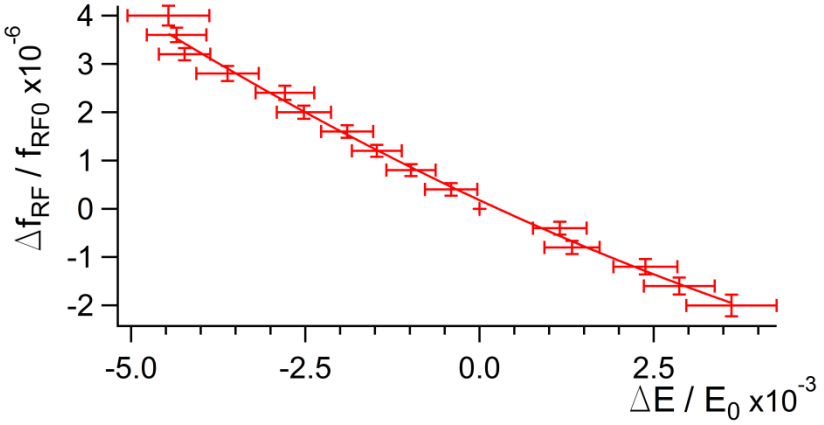

Figure 6.17: Momentum compaction factor for 1.3 GeV 23 k squeeze steps with central frequency f_{RF0} of 499.7206 kHz. The electron beam is around 6-11 mA. The 7 mm aperture centered at -5.5 mm. The vertical error bars are calculated from the horizontal error bars obtained from the energy measurement assuming linear dependence. The vertical error bars are rescaled once based on the initial χ^2/ndf value. Final quadratic fit of the curve gives α_0 as 0.00067 ± 0.00002, α_1 as -0.023 ± 0.007, χ^2/ndf = 11.99/12.

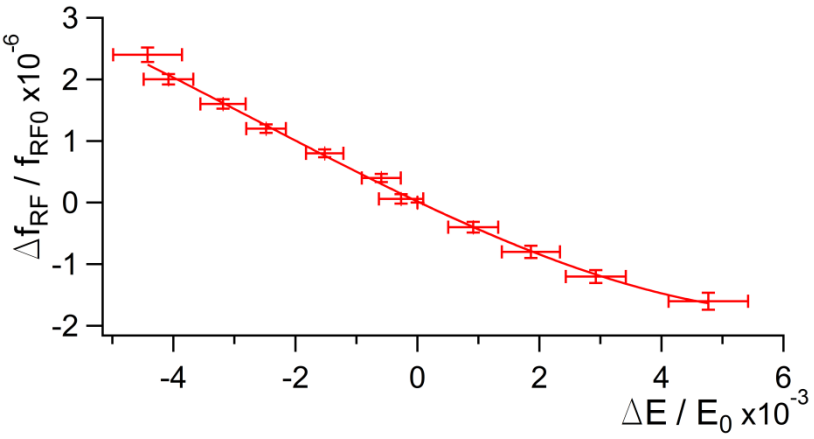

Figure 6.18: Momentum compaction factor for 1.3 GeV 25 k squeeze steps with central frequency f_{RF0} of 499.7206 kHz. The electron beam is around 4-6 mA. The 7 mm aperture centered at -5.5 mm. The vertical error bars are calculated from the horizontal error bars obtained from the energy measurement assuming linear dependence. The vertical error bars are rescaled once based on the initial χ^2/ndf value. Final cubic fit of the curve gives α_0 as 0.00047 ± 0.00002, α_1 as -0.016 ± 0.004, α_2 as -2.0 ± 1.6, χ^2/ndf = 6.99/7.

For 27 k squeeze steps in Fig. 6.19, there are fewer RF frequencies available for a stable beam condition, because for such fully compressed optics the momentum acceptance will also become extremely low. Based on the 8 points in Fig. 6.19, we still can see its clear tendency of nonlinearity. Although both quadratic fit and cubic fit does not give very significant value for high order terms, the χ^2/ndf values indicates the cubic fit gives the best result.

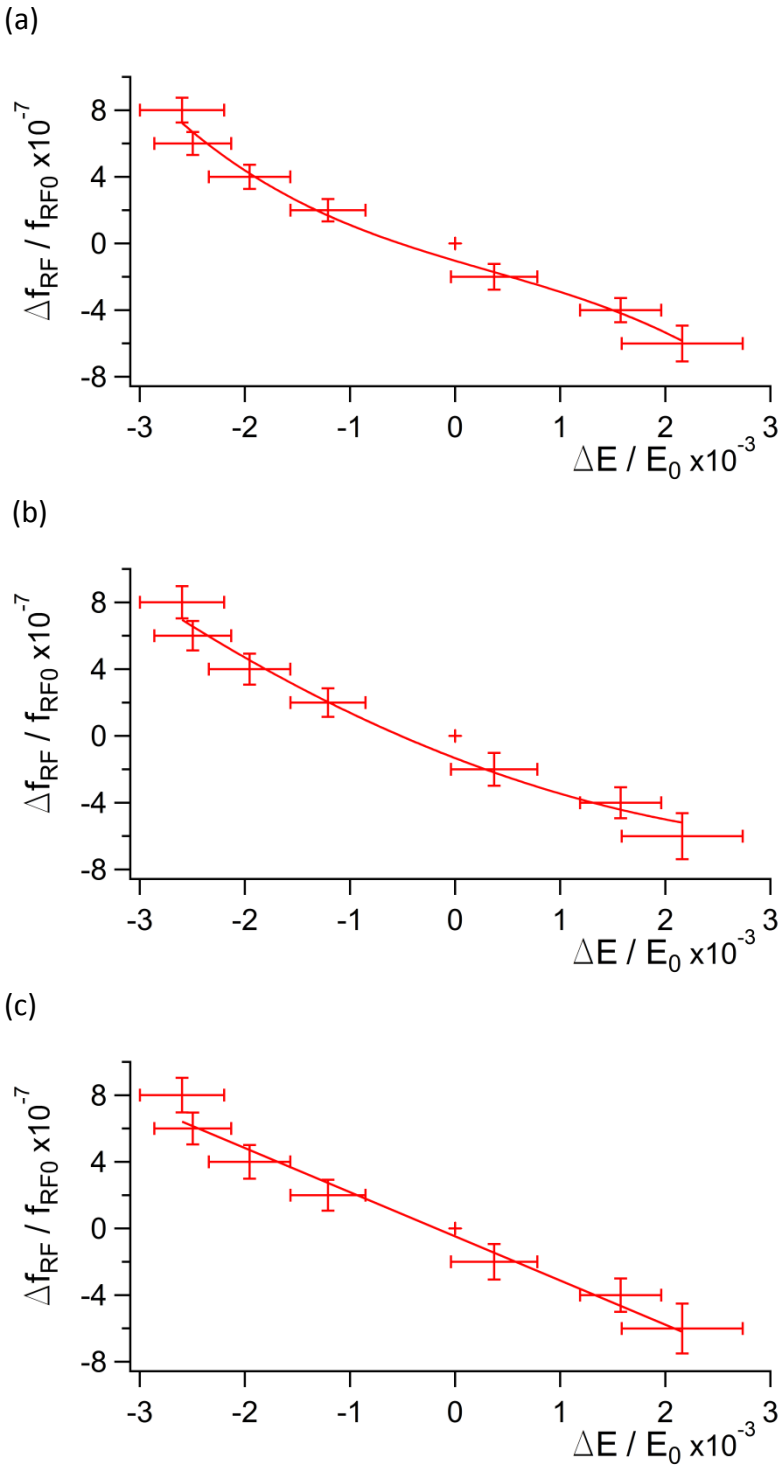

Figure 6.19: Momentum compaction factor for 1.3 GeV 27 k squeeze steps with central frequency f_{RF0} of 499.7206 kHz. The electron beam is around 2-4 mA. The 7 mm aperture centered at -5.5 mm. (a) Cubic fit gives α_0 as 0.00019 ± 0.00005, α_1 as -0.014 ± 0.020, α_2 as 14 ± 12, χ^2/ndf = 2.59/3; (b) Quadratic fit of the curve gives α_0 as 0.00024 ± 0.00003, α_1 as -0.029 ± 0.019, χ^2/ndf = 2.49/4; (c) Linear fit gives α_0 as 0.00027 ± 0.00002, χ^2/ndf = 4.15/5. The vertical error bars are calculated from the horizontal error bars obtained from the energy measurement assuming linear dependence. Based on the χ^2/ndf values, the cubic fitting is the best. After scaling by the initial χ^2/ndf value, the final cubic fitting gives α_0 as 0.00019 ± 0.00005, α_1 as -0.014 ± 0.018, α_2 as 14 ± 11, χ^2/ndf = 3.00/3.

Fig. 6.20 and Fig. 6.21 show additional measurement in fill 5688 for 25 k steps and fill 5697 for 27 k steps. Measurement for 25 k steps only shows several points near f_{RF0} for a linear fit. And 27 k steps measurement gives a clear quadratic term α_1 as -0.022 ± 0.014.

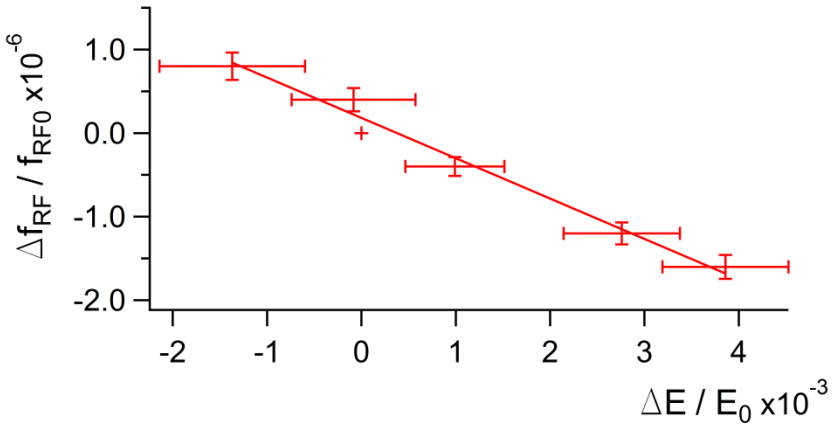

Figure 6.20: Momentum compaction factor for 1.3 GeV 25 k squeeze steps with central frequency f_{RF0} of 499.7219 kHz. The electron beam is around 2-5 mA. The vertical error bars are calculated from the horizontal error bars obtained from the energy measurement assuming linear dependence. The vertical error bars are rescaled once based on the initial χ^2/ndf value. Final linear fit gives α_0 as 0.00048 ± 0.00004, χ^2/ndf = 3.00/3.

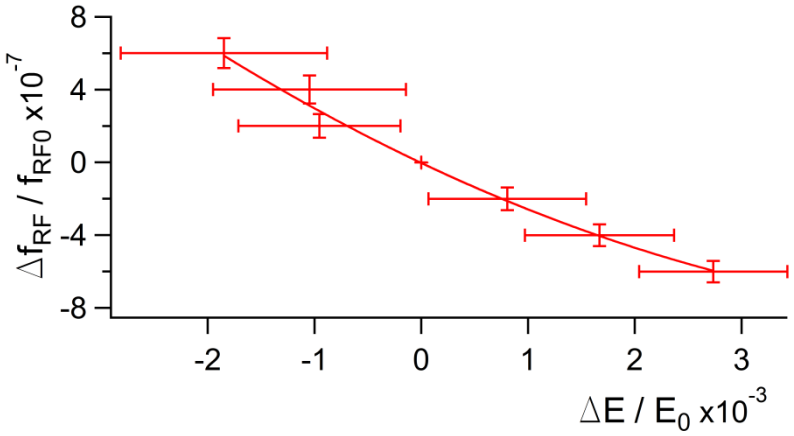

Figure 6.21: Momentum compaction factor for 1.3 GeV 27 k squeeze steps with central frequency f_{RF0} of 499.7209 kHz. The electron beam is around 3-5 mA. The 7 mm aperture centered at -2.5 mm. The vertical error bars are calculated from the horizontal error bars obtained from the energy measurement assuming linear dependence. The vertical error bars are rescaled once based on the initial χ^2/ndf value. Final quadratic fit of the curve gives α_0 as 0.00028 ± 0.00002, α_1 as -0.022 ± 0.014, χ^2/ndf = 2.99/3.

So far the obtained α_c values have been proved accurate and serve as the corner stone for the measurement at ANKA. It significantly helped to better match the bursting threshold measurements to the theoretical prediction based on the measured α_c values, since now they are much more accurate than the assumed ones used before.

7. Summary

Energy is one of the most fundamental concepts in physics. In modern science and technology, synchrotron light sources have become indispensable and provided extremely intensive/bright photons covering the entire spectrum ranging from hard X-rays to THz radiations. As the parameter of energy is included in various aspects of the machine physics and related applications, its accurate calibration is crucial to correctly control the optics, produce accurate photon spectrum and understand the machine. For example, the deviation of α_c greatly influences the calculation of the bursting threshold for the coherent synchrotron radiation generated at low-α_c modes, which can significantly enhance the production of IR/THz radiation, whereas the accurate energy measurement is usually needed for the accurate determination of α_c.

The precise and accurate measurement on electron beam energies above 2 GeV (up to 2.5 GeV) based on the CBS was for the first time demonstrated successfully at ANKA. A completely new approach with a near-perpendicular configuration was carefully designed, developed and implemented instead of the traditional setup based on the head-on collision. The near-perpendicular configuration reduces the Compton edge energy by a factor of two in contrast to the head-on collision. This greatly extends the measurement capability of the CBS method due to the limited detectable range of the HPGe spectrometer, or makes the spectrometer calibration especially easier due to the upper energy limits of the available calibration sources. The detection efficiency is also much increased due to the low energies of the scattered gamma photons.

The new configuration doesn't require any mirror at the front-end area of the beamline to reflect the laser beam into the beam pipe as in the head-on collision. Therefore the new setup can be very compact and used at storage rings with restricted space at the front-end area. In fact, to couple in the laser, it only needs a side port around the ring (except the bending magnet region where the electron beam under deflection), which is commonly available, e.g. the ion pump side port we used at ANKA.

To realize such innovative setup at ANKA, the studies were carried out both analytically and numerically to calculate the anticipated measurement performance and uncertainties. Different experiment locations were evaluated, including various scenarios on the booster ring and the main storage ring. The detailed simulation studies on the characteristics of the scattered photons were performed based on the various parameters of the electron beam and the laser beam at the collision point. The radiation background at the storage ring, mainly the gas bremsstrahlung, was measured and compared to the CBS photon spectra from the simulation to obtain the expected signal-to-noise ratio, including the consideration of various factors in the actual environment.

The laser was carefully selected with the appropriate wavelength and the frequency stability for our setup requirement. The optical subsystem was designed based on both analytical and numerical calculation. A focusing cylindrical lens was adopted to achieve an elliptical focal beam profile to keep vertical beam tightly focused for large interaction luminosity, while the large horizontal beam size significantly increased the beam area shedding on the beam pipe to facilitate the heat dissipation. Given the limitation of the in-coupling apertures, the beam waist sizes were calculated and compared in several scenarios with respect to the enlargement factors and power losses from the clipping/diffraction effect of the laser. The actual beam focal profile was measured and achieved the

same as the theoretical values. The divergence of the laser beam was fully taken advantage of without further requirement of the beam expander. Design with the laser propagation angle off exact 90 degree not only circumvented the mechanical obstruction on the optical path, but also spared the necessity of optical isolators for the possible reflected laser power. The laser propagation angle was determined accurately using the laser tracker and centroid tracking from a camera, which was critical for the determination of the electron beam energy. An HPGe spectrometer was chosen from the comparison with other types of gamma ray detectors. The shielding system was carefully designed since the HPGe was placed inside the concrete shielding walls. The detection table was capable of being adjusted precisely by the laser tracker. The calibration of the HPGe was carried out with only elemental radiation lines from the natural environment. The appropriate natural radiation lines were carefully selected to meet the calibration requirement, and also the influence of the acquisition time on the calibration uncertainty was studied.

The measurement procedure based on the transverse setup was established with the accurate determination of the edge energy from edge curve fitting as well as the accurate collision angle from the laser and electron beam propagation direction. To optimize the setup performance, the laser beam was scanned vertically and longitudinally to achieve the best overlap between the laser and electron beam with the maximum signal rate. Different rise time settings of the HPGe were tested for the optimum solution. The influence of the misaligned absorber at the front-end area was elaborately studied to achieve the best orbit bump of the electron beam in combination with the suitable collimator position.

With the optimized setup at the ANKA storage ring, numerous energies from 0.5 GeV to 2.5 GeV were accurately measured with typical uncertainties of a few 10^{-4}. The momentum compaction factors of different optics at 1.3 GeV was also accurately determined using the setup, which significantly improves the optics control and machine understandings at ANKA, e.g. to precisely calculate the bursting threshold current at low-α_c modes for THz coherent synchrotron radiation production. The successful measurement demonstrated the realization of an innovative and compact setup with low cost and few alternations on the machine, and yet covering much wider energy range in contrast to the conventional method based on the CBS.

Although the near-perpendicular setup with the side port of the ion pump was enough to cover the entire energy range of ANKA (0.5 -2.5 GeV), to further extend the measurement capabilities based on the transverse CBS, a dedicated interaction chamber was designed with dimensions to replace a safety valve on the ANKA storage ring as an example. Such a chamber with an additional out-coupling window and large acceptance angle for the in-coupling laser could allow to enhance the laser power and beam focusing and to improve the signal-to-noise ratio. It may even achieve a versatile instrument with further functions, such as a laser wire system which can be used for the precise measurement of the transverse beam profile. Further adaption to other facilities could be made to allow a collision angle smaller than 90 degree for higher energy measurement, e.g. ~30 degree for the 8 GeV electron beam at Spring-8.

Bibliography

1. Hartemann, F.V., et al., "*High-energy scaling of Compton scattering light sources".* Physical Review Special Topics-Accelerators and Beams, 2005. **8**(10).
2. http://www.lightsources.org/regions on 04.01.2016
3. Martin, I.P.S., et al., "*Experience with low-alpha lattices at the Diamond Light Source".* Physical Review Special Topics-Accelerators and Beams, 2011. **14**(4).
4. Abo-Bakr, M., et al., "*Brilliant, coherent far-infrared (THz) synchrotron radiation".* Physical Review Letters, 2003. **90**(9).
5. Feikes, J., et al., "*Metrology Light Source: The first electron storage ring optimized for generating coherent THz radiation".* Physical Review Special Topics-Accelerators and Beams, 2011. **14**(3): p. 10.
6. A.S. Müller, et al. *"Far infrared coherent synchrotron edge radiation at ANKA"*. In Particle Accelerator Conference 2005, volume 19, pages 18-24. Taylor & Francis, 2005.
7. A.-S. Müller, private communication.
8. Yunhai Cai, *"Theory of microwave instability and coherent synchrotron radiation in electron storage rings"*, Proceedings of IPAC2011.
9. Hsu, I.C., C.C. Chu, and C.I. Yu, "*Energy measurement of relativistic electron beams by laser Compton scattering".* Physical Review E, 1996. **54**(5): p. 5657-5663.
10. Mackay, W.W., et al.,"*Measurement of the gamma-mass".* Physical Review D, 1984. **29**(11): p. 2483-2490.
11. Barber, D.P., et al., "*A precision measurement of the ϒ′ meson mass".* Physics Letters B, 1984. **135**(5–6): p. 498-504.
12. Arnaudon, L., et al., "*Measurement of LEP beam energy by resonant spin depolarization".* Physics Letters B, 1992. **284**(3–4): p. 431-439.
13. J. Zhang, et al, *"Experiments to measure beam energy using spin depolarization method at Soleil"*, IPAC2011.
14. Z. Martí, et al. *"Beam energy measurements using resonant spin depolarization at ALBA"*, Proceedings of IPAC2014.
15. Yamazaki, T., et al., "*Generation of quasi-monochromatic photon beams from Compton backscattered laser-light at etl electron storage ring".* Ieee Transactions on Nuclear Science, 1985. **32**(5): p. 3406-3409.
16. Abakumova, E.V., et al., "*A system of beam energy measurement based on the Compton backscattered laser photons for the VEPP-2000 electron-positron collider".* Nuclear Instruments & Methods in Physics Research Section a-Accelerators Spectrometers Detectors and Associated Equipment, 2014. **744**: p. 35-40.
17. Abakumova, E.V., et al., "*The beam energy measurement system for the Beijing electron-positron collider".* Nuclear Instruments & Methods in Physics Research Section a-Accelerators Spectrometers Detectors and Associated Equipment, 2011. **659**(1): p. 21-29.
18. Blinov, V.E., et al., "*Review of beam energy measurements at VEPP-4M collider KEDR/VEPP-4M".* Nuclear Instruments & Methods in Physics Research Section a-Accelerators Spectrometers Detectors and Associated Equipment, 2009. **598**(1): p. 23-30.
19. Klein, R., et al., "*Operation of the Metrology Light Source as a primary radiation source standard".* Physical Review Special Topics-Accelerators and Beams, 2008. **11**(11): p. 10.
20. Klein, R., et al., "*Measurement of the BESSY II electron beam energy by Compton-backscattering of laser photons".* Nuclear Instruments & Methods in Physics Research Section a-Accelerators Spectrometers Detectors and Associated Equipment, 2002. **486**(3): p. 545-551.

21. Klein, R., et al., "*Beam diagnostics at the BESSY I electron storage ring with Compton backscattered laser photons: Measurement of the electron energy and related quantities".* Nuclear Instruments & Methods in Physics Research Section a-Accelerators Spectrometers Detectors and Associated Equipment, 1997. **384**(2-3): p. 293-298.
22. Sun, C., et al., "*Energy and energy spread measurements of an electron beam by Compton scattering method".* Physical Review Special Topics-Accelerators and Beams, 2009. **12**(6).
23. A.-S. Müller et al., *"Energy calibration of the ANKA storage ring"*, Proceedings of EPAC 2004.
24. A.-S. Mueller, et al., *"Linear and nonlinear optics studies in the ANKA storage ring"*, Proceedings of the 2003 Particle Accelerator Conference.
25. A.-S. Mueller, et al. *"Momentum compaction factor and nonlinear dispersion at the ANKA storage ring"*, Proceedings of EPAC 2004.
26. A.-S. Müller et al., *"Experimental Aspects of CSR in the ANKA Storage Ring"*, Beam Dynamics Newsletter 57, ICFA, p. 154, 2012.
27. A. H. Compton, *"A quantum theory of the scattering of x-rays by light elements".* Phys. Rev., vol. 21, pp. 483–502, May 1923.
28. Milburn, R.H., "*Electron scattering by an intense polarized photon field".* Physical Review Letters, 1963. **10**(3): p. 75-&.
29. Arutyunian, F.R. and V.A. Tumanian, "*The Compton effect on relativistic electrons and the possibility of obtaining high energy beams".* Physics Letters, 1963. **4**(3): p. 176-178.
30. Kulikov, O.F., et al., "*Compton effect on moving electrons".* Physics Letters, 1964. **13**(4): p. 344-346.
31. Sandorfi, A.M., et al., "*High-energy gamma-ray beams from compton backscattered laser-light".* Ieee Transactions on Nuclear Science, 1983. **30**(4): p. 3083-3087.
32. Schoenlein, R.W., et al., "*Femtosecond x-ray pulses at 0.4 angstrom generated by 90 degrees Thomson scattering: A tool for probing the structural dynamics of materials".* Science, 1996. **274**(5285): p. 236-238.
33. Pogorelsky, I.V., "*Ultra-bright X-ray and gamma sources by Compton backscattering of CO2 laser beams".* Nuclear Instruments & Methods in Physics Research Section a-Accelerators Spectrometers Detectors and Associated Equipment, 1998. **411**(1): p. 172-187.
34. Huang, Z.R. and R.D. Ruth, "*Laser-electron storage ring".* Physical Review Letters, 1998. **80**(5): p. 976-979.
35. Weller, H.R., et al., "*Research opportunities at the upgraded HI gamma S facility*", in *Progress in Particle and Nuclear Physics, Vol 62, No 1*, A. Faesssler, Editor. 2009. p. 257-303.
36. Roderick J. Loewen. *"A Compact Light Source: Design and Technical Feasibility Study of a Laser-Electron Storage Ring X-Ray Source"*. SLAC-R-632.
37. C. Bruni, R. Chiche, R. Cizeron, Y. Fedala, J. Haissinski, et al. ThomX - Conceptual Design Report. 2009, pp.1-136.
38. http://www.lynceantech.com/ on 04.01.2015
39. Sakaue, K., et al., "*Observation of pulsed x-ray trains produced by laser-electron Compton scatterings".* Review of Scientific Instruments, 2009. **80**(12).
40. Shimada, M. and R. Hajima, "*Inverse Compton scattering of coherent synchrotron radiation in an energy recovery linac".* Physical Review Special Topics-Accelerators and Beams, 2010. **13**(10): p. 5.
41. Graves, W.S., et al., "*MIT inverse Compton source concept".* Nuclear Instruments & Methods in Physics Research Section a-Accelerators Spectrometers Detectors and Associated Equipment, 2009. **608**(1): p. S103-S105.
42. Du, Y., et al., "*Generation of first hard X-ray pulse at Tsinghua Thomson Scattering X-ray Source".* Review of Scientific Instruments, 2013. **84**(5).
43. R. Nagai, et al. *"Demonstration of high-flux photon generation from an ERL-based laser Compton photon source"*. Proceeding of IPAC 2015.

44. O. Adriani, et al. Technical Design Report EuroGammaS proposal for the ELI-NP Gamma beam System. arXiv:1407.3669
45. M.N. Achasov et al., *"The beam energy calibration system for the BEPC-II collider"*, arXiv: 0804.0159v1 (2008)
46. T.Suzuki,*"General formulae of luminosity for various types of colliding machines"*, KEK Preprint 76-3,(1976)
47. S. White. *"Determination of the absolute luminosity at the LHC"*. Ph. D. thesis of Universite Paris Sud - Paris XI, 2010.
48. C. Sun. *"Characterizations and Diagnostics of Compton Light Source"*. Ph.D. thesis of Duke University, 2009.
49. K. Yokoya. User's Manual of CAIN, Version 2.42. https://ilc.kek.jp/~yokoya/CAIN/ on 04.01.2015
50. Sebastian Marsching and Nicole Hiller, Private communication.
51. Erhard Huttel, Private communication.
52. Doug Reilly, et al. Passive Nondestructive Assay of Nuclear Materials. 1991.
53. Osae, E.K., et al., "*An empirical expression for the full energy peak efficiency of an N-type high purity germanium detector".* Journal of Radioanalytical and Nuclear Chemistry, 1999. **242**(3): p. 617-622.
54. Kis, Z., et al., "*Comparison of efficiency functions for Ge gamma-ray detectors in a wide energy range".* Nuclear Instruments & Methods in Physics Research Section a-Accelerators Spectrometers Detectors and Associated Equipment, 1998. **418**(2-3): p. 374-386.
55. Raman, S., et al., "*Efficiency calibration of a Ge detector in the 0.1-11.0 MeV region".* Nuclear Instruments & Methods in Physics Research Section a-Accelerators Spectrometers Detectors and Associated Equipment, 2000. **454**(2-3): p. 389-402.
56. Molnar, G.L., Z. Revay, and T. Belgya, "*Wide energy range efficiency calibration method for Ge detectors".* Nuclear Instruments & Methods in Physics Research Section a-Accelerators Spectrometers Detectors and Associated Equipment, 2002. **489**(1-3): p. 140-159.
57. Sakaue, K., A. Endo, and M. Washio, "*Design of high brightness laser-Compton source for extreme ultraviolet and soft x-ray wavelengths".* Journal of Micro-Nanolithography Mems and Moems, 2012. **11**(2).
58. K. Sakaue, et al. *"Demonstration of an optical enhancement cavity with 10 micron wavelength"*, Proceedings of SPIE, 2015
59. A.Terebilo. Accelerator Toolbox for MATLAB. SLAC-PUB-8732. 2001.
60. Lars Præstegaard, Ph.D. thesis, *"Investigations of the ANKA Injector: Lattice, Beam Properties and Performance"*, 2001.
61. http://www.nist.gov/pml/data/xraycoef/index.cfm on 04.01.2014
62. https://www.coherent.com/downloads/sabre_techsheet.pdf on 04.01.2016.
63. Yosuke Honda, *"Development of CW laser wire in storage ring and pulsed laserwire"*, Proceedings of PAC09, 2009.
64. Henrik Jørgensen (customer service at Danfysik), private communication.
65. "Manual: Stabilized CO_2 Laser", DLR.
66. Anthony E. Siegman, *"Defining, measuring, and optimizing laser beam quality"*, Proc. SPIE 1868, Laser Resonators and Coherent Optics: Modeling, Technology, and Applications, 2 (February 5, 1993); oi:10.1117/12.150601; http://dx.doi.org/10.1117/12.150601
67. http://www.lambdares.com/oslo-university-program, on 04.01.2014
68. A. E. Siegman. Lasers. 1986. P666-667.
69. Gillen, G.D., C.M. Seck, and S. Guha, "*Analytical beam propagation model for clipped focused-Gaussian beams using vector diffraction theory".* Optics Express, 2010. **18**(5): p. 4023-4040.

70. Ahmet, K., "*The OPAL detector at LEP".* Nuclear Instruments & Methods in Physics Research Section a-Accelerators Spectrometers Detectors and Associated Equipment, 1991. **305**(2): p. 275-319.
71. G. F. Knoll. *"Radiation Detection and Measurement"*, fourth edtion, 2010.
72. N. Tsoulfanidis, S. Landsberger. *"Measurement and Detection of Radiation"*, third edition. 2010.
73. P. Russo and D. Vo. *"Gamma-Ray Detectors for Nondestructive Analysis".* LA-UR-05-3813, Passive Nondestructive Assay of Nuclear Materials,2007 Addendum.
74. Handout from ORTEC, Inc. *"PROFILE HPGe Photon Detector Product Configuration Guide"*, www.ortec-online.com/download/profile.pdf on 04.01.2014
75. User's Manual of DSPEC-50, AMETEK, Inc.
76. R.D. Bingham, R.M. Keyser, T.R. Twomey, *"An Innovative, Portable MCA Based on Digital Signal Processing".* Conference Proceedings, 23rd ESARDA meeting on Safeguards and Nuclear Materials Management, Brugge, May 2001.
77. Michael Holz. *"Determination of the Transversal Electron Beam Size at the ANKA Storage Ring"*. Master thesis. 2014.
78. Ferrari, A., M. Pelliccioni, and P.R. Sala, "*Estimation of fluence rate and absorbed dose-rate due to gas bremsstrahlung from electron storage-rings".* Nuclear Instruments & Methods in Physics Research Section B-Beam Interactions with Materials and Atoms, 1993. **83**(4): p. 518-524.
79. http://www.nucleide.org/DDEP_WG/DDEPdata.htm, on 04.01.2014.

Acknowledgments

First of all, I want to thank Prof. Anke-Susanne Müller and Prof. Marc Weber for the opportunity of this thesis. Thanks to the EU Marie Curie funding program, LA³NET (LAsers for Applications at Accelerator facilities NETwork). In particular, special thanks to Prof. Anke-Susanne Müller for the supervision and inspired instructions at ANKA.

Thanks to Michael Nasse and Erhard Huttel for the fruitful discussions, comments and supervision. Special thanks to Michael, who helped me to order nearly all the components of the setup as a post-doc, made a handy panel in Igor for the frequent curve fitting/data analysis and contributed lots of great ideas and advise to this work. Michael also spent a lot of time in the ANKA hall helping me as a laser expert, and did various jobs regarding interfaces of organization, translation and preparation. I would like to thank Erik Bründermann for the help and advises based on his broad knowledge and experience, especially the introduction to the crucial CO_2 laser system from DLR. I want to express my sincere thanks to Nicole Hiller and Johannes Steinmann for their valuable and skillful aid on the optics alignment and component setup. Nicole also helped to operate the machine, transport the laser system from Berlin and actively facilitated and helped my integration into the life in Germany. I also would deeply thank Marcel Schuh and Edmund Hertle for their professional and experienced operation of the machine, which provides a crucial basis for the measurement, in particular for the orbit optimization due to machine misalignment.

Special thanks go to the entire THz group and all the colleagues at ANKA for all their support to this work. In particular, thanks to A. Voelker and T. Fischboeck for the valuable discussion and suggestion about the vacuum components and laser tracker measurement. Thanks to R. Lang for all the excellent buildings and constructions for the setup. Thanks to N. J. Smale for instructive discussions and operating the machine. Thanks to S. Marsching and J. Schmid for the controller issues of the translation stages as well as refilling of the LN_2 dewar by J. Schmid. Thanks to M. Süpfle and the IR beamline for testing our components and other equipment support. Thanks to L. Weinhardt, P. Nagel and S. Schuppler for the smooth collaboration on the beamline construction schedule and the components at the front end area of XSPEC and WERA beamlines. Thanks to S. Bauer, et al. for supporting our measurements at the ANKA IMAGE beamline. Thanks to M. Hagelstein and D. Bachelor for the organization and the help on the bremsstrahlung measurement.

Thanks to R. Klein at MLS, Berlin for the inspired discussion. Thanks to C. Wilhelm and S. Kaminski at KSM/KIT for lending us the HPGe detector and a lot of valuable suggestions and instructions. Also particularly thanks to Prof. Hübers and H. Richter from DLR, Berlin, for making the laser available to us and giving us the practical instructions and valuable supports.